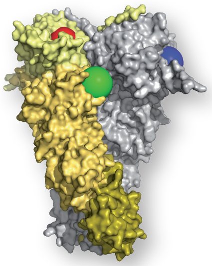

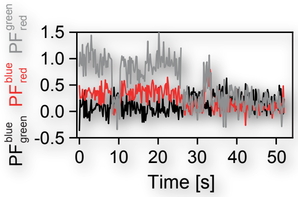

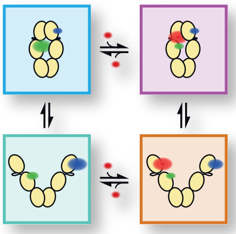

Multi-Color Single-Molecule FRET Experiments and Analysis

The Dynamic Protein System Hsp90

Markus Götz

Technische Universität München
Physik Department
Lehrstuhl für Biophysik, E22

Multi-Color Single-Molecule FRET Experiments and Analysis

The Dynamic Protein System Hsp90

Markus Götz

Vollständiger Abdruck der von der Fakultät für Physik der Technischen Universität München
zur Erlangung des akademischen Grades eines

Doktors der Naturwissenschaften (Dr. rer. nat.)

genehmigten Dissertation.

Vorsitzender:		Prof. Dr. Martin Zacharias
Prüfer der Dissertation:	1.	Prof. Dr. Thorsten Hugel
	2.	Prof. Dr. Friedrich Simmel

Die Dissertation wurde am 27.09.2017 bei der Technischen Universität München

eingereicht und durch die Fakultät für Physik am 16.11.2017 angenommen.

Markus Götz: *Multi-Color Single-Molecule FRET Experiments and Analysis*,

Table of Contents

Appendices

Abstract

Proteins are the “workhorses” of a cell. In order to fulfill their task, they have to dynamically adopt different conformations and interact with other biological molecules. Protein structure determination (e.g. with X-ray crystallography) has been and still is a valuable source of static structural information. However, a complete understanding of the complex processes in a cell can only arise from both, a static and a kinetic description.

Single-molecule Förster resonance energy transfer (smFRET) between a dye-pair attached to specific positions of a protein allows tracking distances and distance changes on a length scale relevant for biomolecules in real time. Using three-color instead of two-color smFRET experiments literally adds another dimension to the analysis of biomolecular machines because it offers the possibility to directly observe the correlation between two molecular interactions or conformational changes. This is essential for truly understanding biological multi-state and multi-component systems. However, reliable tools for the analysis of such data have been lacking because experiments were performed mostly on simple model systems so far.

In the first part of this work, a three-color smFRET analysis is presented that is capable of dealing with the shortcomings of “real world” protein samples. In a two-step approach, first the position of all distinguishable states in the three-dimensional FRET space is determined (one dimension for each distance between the three dyes). In a second step, the optimal parameters of the kinetic model comprising all distinguishable states are found using hidden Markov models (HMM). This maximum likelihood method also permits specifying the uncertainty of all extracted parameters. The reliability and precision of the approach are demonstrated.

In the second part of this work the dynamic multi-domain heat shock protein 90 (Hsp90) in combination with several of its interaction partners is studied with different smFRET approaches. Hsp90 is a chaperone, i.e. it helps other proteins to maturate and reach their functional active state. Eukaryotic Hsp90 acts in a dynamic network with at least 20 transiently associated proteins, so-called co-chaperones, and serves as a hub for activation of numerous signaling pathways, thereby regulating diverse cellular functions.

Two co-chaperones (Aha1 and p23) and a model-substrate (Δ131Δ) are investigated. They induce subtle changes in Hsp90. However, they are not able to fundamentally change the characteristic N-terminal dynamics of the chaperone. This suggests that Hsp90’s structural flexibility actually might be part of its function. Another project focuses on the nucleotide binding of Hsp90 and reveals a previously overlooked cooperativity between the two nucleotide binding pockets of the Hsp90 dimer. The cooperativity is not caused by ATP affecting one single transition, but by the combined effects of the nucleotide on four transitions in the studied system.

In summary, a novel approach in the analysis of dynamic multi-state and multi-protein systems has been developed and applied to Hsp90 in this work. Multi-color smFRET experiments will most likely be an important method to decipher the physics of life in the future.

Publications

Some ideas and figures have appeared previously in the following publications:

[A] Götz, Wortmann, Schmid & Hugel. “A Multicolor Single-Molecule FRET Approach to Study Protein Dynamics and Interactions Simultaneously”.
Methods in Enzymology 581 (2016)

[B] Schmid, Götz & Hugel. “Single-Molecule Analysis beyond Dwell Times: Demonstration and Assessment in and out of Equilibrium”.
Biophysical Journal 111 (2016)

[C] Wortmann, Götz & Hugel. “Cooperative Nucleotide Binding in Hsp90 and Its Regulation by Aha1”.
Biophysical Journal 113 (2017)

[D] Götz, Wortmann, Schmid & Hugel. “Using Three-color Single-molecule FRET to Study the Correlation of Protein Interactions”.
Journal of Visualized Experiments (accepted)

Acknowledgments

This work would not have been possible without the – scientific and non-scientific – help, encouragement and support from many people.

First of all, I want to thank my supervisor, Thorsten Hugel, for giving me the opportunity to work in his group and for maintaining an atmosphere that set only few boundaries. I acknowledge the contributions from my cooperation partners, the Agard lab and the Sönnichsen group.

Doing my PhD took a turn when the Hugel group moved from Munich to Freiburg. I want to thank all the people from the E22/E27 back in Munich and also everybody from the new “Alte PC” in Freiburg – you are just too many to name you all – for help in fighting the bureaucracy, for keeping the lab and all other infrastructure running and for sharing offices, ideas, labs, code, food, beer, thoughts, ...

Thanks to Philipp Wortmann for his impatience that I sometimes lack. And to Sofia Brander not only, but also for trying hard and introduce us to Freiburg. I owe a lot to Sonja Schmid, though we never played real office ping-pong, there has been indeed a ping-pong of ideas that I appreciate. And the possibility to talk about everything and anything.

I want to thank Anna and Clara for sharing a flat that was more than just a place to stay. And I want to thank my friends from Neumarkt, my family and my sister Dani for keeping me in contact with the world outside of the PhD.

Thank you, Asia, for more than words can say.

Ever tried. Ever failed. No matter. Try again. Fail again. Fail better.

— Samuel Beckett

1. Introduction and Motivation

Biological macromolecules (e.g. DNA, RNA or proteins) can fulfill their function only by the constant interaction with other molecules in the cell. Proteins, which are the “workhorses” of the cell, get synthesized by ribosomes, large protein-RNA complexes, and are helped to fold or held in an active form by other proteins called molecular chaperones. Proteins achieve their specific task by interacting with different partners or substrates on a broad range of time-scales [44, 87, 118] and with a broad range of affinities and eventually get degraded by yet another large, highly-regulated multi-component machinery, the proteasome. Besides, the number of genes does not differ substantially between e.g. humans and the nematode *Caenorhabditis elegans*, suggesting that “complexity” may in part rely on the contextual combination of the gene products [29].

Determination of the tertiary and quaternary structure of proteins and multi-component complexes has proven to be a very helpful approach in the course of studying their function. However, no matter how appealing and instructive such a structure might be, only with also taking into account the transient conformations proteins can adopt and the dynamic nature of their arrangement, the full picture of a protein’s function becomes available [2]. The matter gets even more complicated when the *interplay* of different constituents in a multi-component system is to be studied. These complexes are governed by the dynamic association and dissociation of its components.

1.1. Single-Molecule Experiments

With the advent of single-molecule techniques for biological samples in the late 1970’s and optical methods for detection of single molecules in the 1990’s, researchers started to become capable of studying these large and dynamic molecules directly for the first time. Insights into their mechanism at unprecedented resolution and sensitivity are possible by revealing details that are masked by conventional ensemble measurements [8]. In fact, single-molecule methods are now so widespread and accepted in chemistry and biology that it has become natural to use the single-molecule thermal energy ($k_B T$), instead of the ensemble one (RT), as the unit of energy [40].

Single-molecule techniques are able to reveal static and dynamic heterogeneity. Static heterogeneity refers to the fact that a protein generally adopts more than just one conformation. Single-molecule experiments can resolve these different species and their population while ensemble measurements only report on the ensemble-average. Dynamic heterogeneity means that the system under study shows a wide variation in the rates that govern the transitions between the different conformations. There is no need for relaxation methods (e.g. rapid mixing or jump experiments) in order to resolve the kinetics of these transitions because an individual molecule can be observed in real time as it spontaneously alternates between states under steady-state or equilibrium conditions [8]. In both cases, single-molecule methods are able to detect the occurrence of rare events and it is “only” a matter of a sufficient data set size to ensure statistical significance.

One popular method of studying single biomolecules is single-molecule Förster resonance energy transfer (smFRET). It is a versatile tool for studying biomolecules in a quantitative manner. Multiple conformations within and interactions between biomolecules can be detected. As FRET is distance dependent, the structure of the different conformations can be determined [90, 15, 58, 43]. From the sequence of states, the kinetics and thus also the thermodynamics of the system can be extracted.

Common two-color smFRET experiments can provide only limited insight into the function of biological systems, which typically consist of more than two components. A complete understanding of complex multi-component biological systems requires correlated information on conformational rearrangements on the one hand and transient interactions with binding partners on the other. Multi-color smFRET experiments enable the direct observation of such correlated dynamics and interactions.

One of the most common proteins in the cell is heat shock protein 90, which plays a key role in the regulation of many essential cellular functions such as signaling, transcriptional regulation and protein homeostasis [100]. Multi-color smFRET experiments are perfectly suited to study its large conformational flexibility and its multitude of dynamic co-chaperone complexes.

1.2. Heat Shock Protein 90

The heat shock protein 90 (Hsp90) is a molecular chaperone. This means, it assists other proteins to reach their functional form as it is involved in their activation and cellular stabilization [98]. Its name stems from the fact that it was first found to be overexpressed under elevated temperatures and has an approximate molecular weight of 90 kDa. Hsp90 is the key protein of a huge multi-component machinery, which consists of more than 20 so-called co-chaperones that can transiently interact with Hsp90 and regulate its function [134]. It is one of the most abundant proteins, even in unstressed cells, accounting for about 1% of the total soluble cytosolic protein [69]. Thus, it is hardly surprising that Hsp90 is essential for cell viability under all conditions in eukaryotic organisms [12, 79] and has become a prominent anti-cancer drug target [143].

While Hsp90 is absent in archaea, bacteria typically carry one Hsp90 gene, high-temperature protein G (HtpG). In eukaryotes, two cytosolic forms exist, an inducible (Hsp82 in *Saccharomyces cerevisiae*, HSP90α_1 and HSP90α_2 in human) and a constitutive form (Hsc82 and HSP90β in *S. cerevisiae* and human, respectively). In animals, additional endoplasmic reticulum (Grp94 in human) and mitochondrial (TRAP1 in human) homologues exist [17, 117].

Hsp90 is a homo-dimer and can adopt at least two globally distinct conformations – a closed one where the two subunits are arranged in a parallel way with close contacts between the domains and an open, V-shaped one (Fig. 1.1). Each subunit comprises four structural segments [100, 117]:

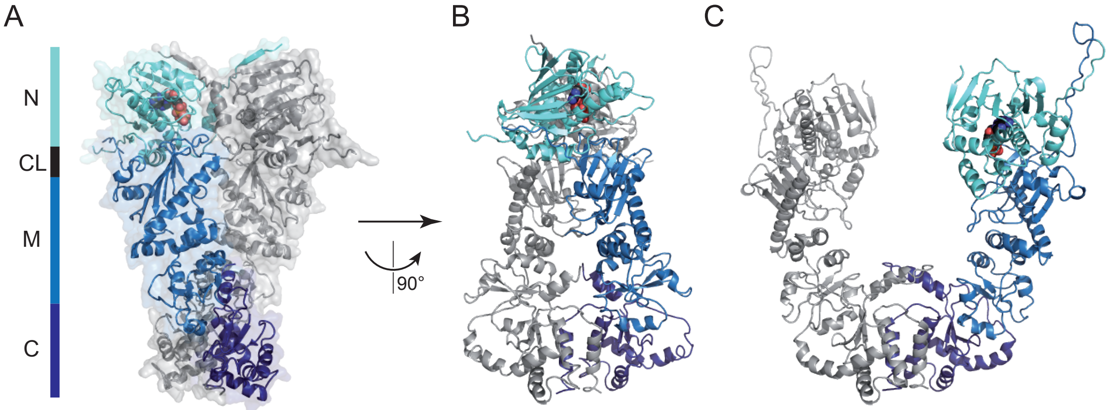

Figure 1.1: The structure of yeast Hsp90. (A) N-terminal closed conformation, PDB 2CG9 [5]. One subunit is shown in color, with the N-terminal (turquoise), middle (blue) and C-terminal (dark blue) domain, the other in gray. The position of the charged linker (CL) is also indicated. The nucleotide in the N-terminal binding pocket is shown as space-filling spheres in CPK coloring or gray. (B) Rotated view of (A). (C) Open conformation of Hsp90 with the CTD aligned to the view in (B) [43].

- The N-terminal domain (NTD) that harbors the nucleotide binding pocket. A motif in this domain, called “ATP lid”, can close over the bound nucleotide.
- The charged linker (CL) which connects the NTD and the middle domain and modulates their domain contacts and Hsp90’s biological function [54].
- The middle domain (MD) which has to interact with the NTD (via the “catalytic loop” that is part of the MD) in order to from the split ATPase domain [117] and allow hydrolysis to occur. It is – like the other domains – involved in client and co-chaperone binding.
- The C-terminal domain (CTD) that provides the dimerization interface. The CTD ends with the conserved MEEVD penta-peptide – the tetratricopeptide repeat (TPR) recognition site.

The Hsp90 dimer has a dissociation constant of about 60 nM [113] and dimerization is essential for the function of Hsp90 *in vivo* [77, 139]. The ATPase rate in the Hsp90 chaperone family is slow, about one ATP min^{-1} for the Hsp90 dimer in the yeast homologue. Nevertheless, the ability to hydrolyze ATP has been reported to be essential *in vivo* [93, 86]. The ATPase requires dimerization and the presence of both NTD [139, 113].

Negative-stain electron microscopy (EM) [126], small-angle X-ray scattering and cryo-EM [13] as well as single-molecule experiments [85, 115, 43] show that eukaryotic Hsp90 is predominately (i.e. at least 85%) in the open conformation under apo (i.e. no nucleotide present) or saturating ADP or ATP conditions. Only in the presence of AMP-PNP, a non-hydrolyzable ATP analog, a stable N-terminally closed state can be reached.

The function of Hsp90 is modulated by co-chaperones. Several of them contain a TPR domain and bind to the CTD of Hsp90. However, binding sites for co-chaperones have been identified in all three domains of Hsp90 [117]. Hsp90 is believed to work in a chaperone cycle, i.e. it progresses through a set of functional and conformational states, with some co-chaperones (e.g. Aha1 and p23) regulating distinct steps in this cycle. Others act as adapter proteins for client recruitment (e.g. Cdc37) or connect Hsp90 to the Hsp70 chaperone system (e.g. Hop). However, a consistent and generally accepted model and the molecular details of the proposed chaperone cycle are still missing.

The class of proteins that rely on the help of Hsp90 to reach their fully functional state contains several hundred members and is highly enriched in signal transducers [134, 117]. These substrates of Hsp90 are often also called “client” proteins. No discrete binding motifs (be it structure or sequence) are known that would designate a protein as a client of Hsp90 [62]. Rather, Hsp90 binding seems to be linked with the overall structural stability of the client [134, 117] and/or by distributing contacts over a large surface area in both Hsp90 and the substrate [62]. However, it is speculated that Hsp90 is not required for the *de novo* folding of most proteins [92].

Three modes of interaction with substrate proteins can be distinguished in the case of Hsp90 [117]:

- It permits a client to reach a distinct, active conformation (e.g. in the case of kinases).
- It helps to assemble multi-protein complexes (e.g. the kinetochore complex).
- It facilitates the binding of a ligand to its receptor by stabilizing the binding-competent, open conformation of the receptor (e.g. binding of steroid hormone to the glucocorticoid receptor).

However, the function of Hsp90 in the activation of its clients and the detailed mechanisms still remains largely elusive.

Multi-color smFRET can help to study these multi-component systems as they allow tracking correlated interactions and conformational changes. The aim of this work has been to develop the necessary analysis tools and to gain insights into the complex Hsp90 chaperone machinery. The influence of two important co-chaperones (Aha1 and p23) and a model-substrate ($\Delta 131\Delta$) on Hsp90 are investigated in order to better comprehend the regulation mechanisms of the chaperone system. An substantial contribution to this understanding is the identification of Hsp90’s flexibility as a major factor to control its interactions.

2. Theory

2.1. Fluorescence

The emission of light by a substance is called luminescence, and can be further divided into two categories – fluorescence and phosphorescence – depending on the nature of the excited state from which the light is emitted after absorption of a photon [53, 70]. In the case of fluorescence, an excited singlet state (S) exists, i.e. the electron in the excited orbital is paired (by opposite spin) to the second electron in the ground-state orbital. Hence, return to the ground state is spin-allowed and happens rapidly (typically within 10^{-8} s), by emission of a photon. Phosphorescence is the emission of light from triplet excited states, where transitions to the ground state are spin-forbidden and the lifetimes are long (typically 10^{-3} to 10^{-2} s or even longer). Transitions between the different electronic states can be illustrated by a Jabłoński diagram (Fig. 2.1) [52]. At room temperature, the thermal energy is not sufficient to significantly populate any excited vibrational states. This is why absorption and emission primarily start from the vibrational ground state.

Upon light absorption, the fluorophore is usually excited to some higher vibrational level of either S_1 or S_2. This is described by the Franck-Condon principle. Electronic transitions are fast compared to the time scale of the nuclear motion (Born-Oppenheimer approximation). Thus, the new vibrational level has to be immediately compatible with the vibrational wavefunction of the initial electronic state. The probability for a transition is proportional to the square of the overlap of the vibrational wavefunctions of the initial and final state. If the electron configuration of the new electronic state is shifted in equilibrium position of the nuclei compared to the initial state, the most likely transition is accompanied with a change in the vibrational level.

Typically, molecules in condensed phases then rapidly relax to the lowest vibrational level of S_1 by processes called vibrational relaxation and internal conversion that occurs within 10^{-12} s or less. Since fluorescence lifetimes are usually around 10^{-9} to 10^{-8} s, these relaxations are generally complete prior to emission of a photon. Thus, fluorescence or phosphorescence occurs with considerably yield only from the lowest excited state. This is known as Kasha's rule [63].

A general property of fluorescence that follows from this mechanism is that the same fluorescence emission spectrum is usually observed irrespective of the excitation wavelength. Also, the emission spectrum is typically a mirror image of the absorption spectrum of the $S_0 \rightarrow S_1$ transition since the vibrational levels in S_0 and S_1 are similar. Finally, vibrational relaxation, internal conversion and further effects like solvent relaxation result in a loss of energy. Hence, fluorescence typically occurs at lower energies (i.e. longer wavelengths) compared to the absorption. This is known as Stokes shift.

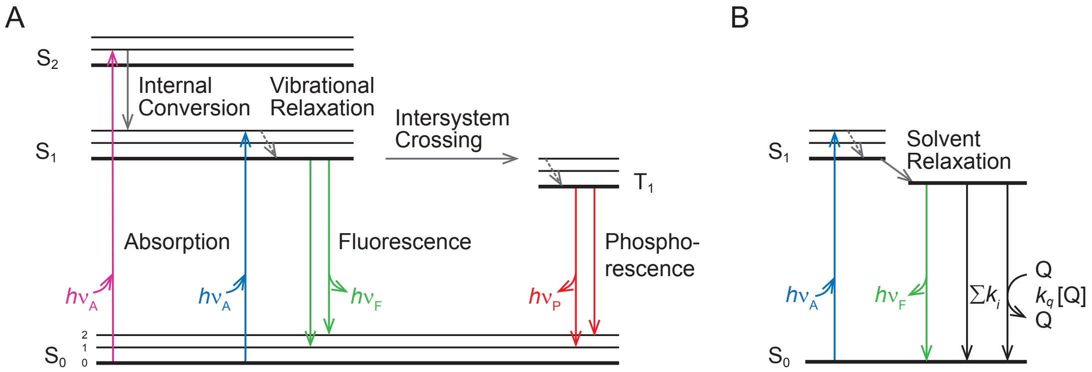

Figure 2.1: Typical Jabłoński diagram depicting fluorescence. (A) The singlet ground, first, and second electronic states (S_0, S_1, and S_2, respectively) are shown. At each of these electronic energy levels the fluorophores can exist in a number of vibrational energy levels, depicted by 0, 1 and 2. The first triplet state (T_1) is also shown. (B) Simplified Jabłoński diagram showing the effect of solvent relaxation and also non-radiative paths to the ground state ($\sum k_i$) and collisional quenching. Figure based on Ref. [70].

2.2. Förster Resonance Energy Transfer

Förster resonance energy transfer (FRET) is a process of non-radiative energy transfer between two fluorophores that is strongly distance-dependent. It has become widely used in the biological sciences due to the favorable distances for energy transfer on the order of a few nanometers. This length scale ideally matches the size of many proteins or the thickness of a lipid bilayer [70].

FRET can be described as an intermolecular long-range dipole-dipole interaction by which energy is transferred from a fluorophore in the excited state (the “donor”) to another fluorophore in the ground state (the “acceptor”) . Hence, the energy transfer occurs without the appearance of a photon (Fig. 2.2A).

Förster showed that – assuming point dipoles in a homogeneous medium – the rate of energy transfer for this process (k_{ET}) is proportional to the inverse of the sixth power of the distance r between the two fluorophores [26]:

$$k_{ET}(r) = \frac{1}{\tau_{DO}} \left(\frac{R_0}{r}\right)^6 \tag{2.1}$$

with the fluorescence lifetime of the donor in absence of the acceptor (τ_{DO}) and the Förster radius R_0 that represents the distance where 50% of the absorbed energy is transferred to the acceptor. The Förster radius of a dye pair depends on the quantum yield of the donor in the absence of the acceptor (Q_D), the relative orientation of the donor and acceptor transition dipoles (κ^2), the refractive index (n), the Avogadro constant (N_A) and the spectral overlap of the emission spectrum of the donor ($F_D(\lambda)$) with the absorption spectrum of the acceptor ($\epsilon_A(\lambda)$):

$$R_0^6 = \frac{Q_D\,\kappa^2}{n^4}\,\frac{9000\,\ln(10)}{128\,\pi^5\,N_A}\,\frac{\int_0^\infty F_D(\lambda)\,\epsilon_A(\lambda)\,\lambda^4\,\mathrm{d}\lambda}{\int_0^\infty F_D(\lambda)\,\mathrm{d}\lambda} \tag{2.2}$$

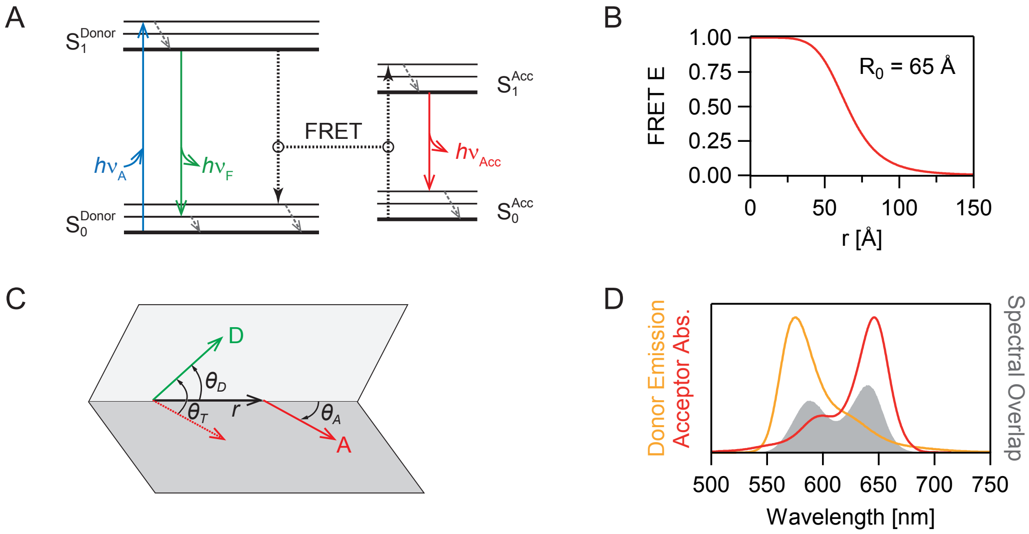

Figure 2.2: Conceptual basis for the energy transfer between a donor-acceptor pair. (A) Jabłoński diagram of Förster resonance energy transfer (FRET). (B) Distance dependence of the FRET efficiency from the dye separation r, shown for an exemplary Förster radius $R_0 = 65\,\text{Å}$. (C) The angles between the transition dipoles of the emission of the donor (green) and the absorption of the acceptor (red) needed for the calculation of κ^2. (D) The spectral overlap of the emission spectrum of the donor with the absorption spectrum of the acceptor. Figure based on Ref. [70].

The efficiency of the energy transfer (E) is the fraction of energy transfer events occurring per donor excitation event. This fraction is given by

$$E = \frac{k_{ET}(r)}{k_f + k_{nr} + k_{ET}(r)} = \frac{k_{ET}(r)}{\tau_{DO}^{-1} + k_{ET}(r)} \tag{2.3}$$

with the fluorescent decay rate k_f and the sum of the rate constants of any other de-excitation pathway k_{nr}. These two can be summed to yield the inverse of the fluorescence lifetime of the donor τ_{DO}. Using Eq. (2.1), this can be rewritten as

$$E = \frac{1}{1 + \left(\frac{r}{R_0}\right)^6} \tag{2.4}$$

In order to relate the distance between the two fluorophores to the FRET efficiency (which is experimentally accessible), the Förster radius has to be known. The overlap integral and the quantum yield of the donor (for the fluorophores attached to the sample molecule) can (in principle) be determined experimentally. The correct choice for the refractive index is not so clear, however [67]. The controversial question is which medium is relevant for the energy transfer: the one directly intervening donor and acceptor, the one of a region much wider than the immediate vicinity of the donor and acceptor or the one directly surrounding the dyes. As a consequence, a refractive index somewhere between that of water ($n = 1.33$) or small organic molecules ($n = 1.4$) is often assumed.

Likewise, the orientation factor κ^2 is a constant source of debate. It is given by

$$\kappa^2 = (\cos\theta_T - 3\cos\theta_D \cos\theta_A)^2 \tag{2.5}$$

where θ_T is the angle between the emission transition dipole of the donor and the absorption transition dipole of the acceptor, and θ_D and θ_A are the angles between these dipoles and the vector joining the donor and the acceptor (Fig. 2.2C). κ^2 can take values from 0 to 4 (0 for perpendicular, 1 for parallel and 4 for head-to-tail oriented transition dipoles). If the fluorophores are sufficiently mobile, rotational diffusion can randomize their orientation prior to energy transfer ($k_{rot} \gg k_{ET}$). Integration over all possible transition dipole orientations yields $\kappa^2 = 2/3$. To check if this assumption holds, separate measurements of the fluorescence anisotropy of the donor only and the acceptor only samples can be performed. The faster the anisotropy decay in time-resolved measurements or the lower the steady state anisotropy, the more orientations the dye samples before energy transfer takes place. However, no clear criterion exists when a dye (or the combination of two dyes) is mobile enough to safely assume $\kappa^2 = 2/3$.

Experimentally, the FRET efficiency can be determined from either the fluorescence lifetime or the fluorescence intensities:

$$E = 1 - \frac{\tau_{DA}}{\tau_{DO}} = 1 - \frac{F_{D|D}^{DA}}{F_{D|D}^{DO}} = \frac{F_{A|D}^{DA}}{F_{A|D}^{DA} + F_{D|D}^{DA}} \tag{2.6}$$

where τ_{DA} and τ_{DO} are the donor fluorescence lifetimes in the presence and absence of an acceptor, respectively, and $F_{D|D}^{DA}$ and $F_{D|D}^{DO}$ are the donor fluorescence intensities after donor excitation in the presence and absence of an acceptor, respectively, and $F_{A|D}^{DA}$ is the acceptor fluorescence intensity after donor excitation.

Despite the mentioned uncertainties in the determination of R_0, FRET can be used to estimate distances or changes in distance for biological samples and is referred to as a "spectroscopic ruler" [130]. A big step forward in the development of methods for understanding biomolecules was the introduction of single-molecule FRET, first with near-field detection [39] and shortly later also with a far-field approach [121].

2.3. Single-Molecule Detection

Even though detectors with single-photon sensitivity and a high quantum yield exist, the detection of single fluorophores with sufficient contrast is still a technological challenge [70, 8]. In order to achieve a single-molecule sensitivity with optical setups, the background signal from the system has to be minimized. It stems from impurities in the measurement chamber, auto-fluorescence of optical components, Raman scattering and dark current from the detector. The Raman cross-section for water is small compared to the cross-section for absorption of a fluorophore. However, the concentration of water is high compared to the fluorophore. Besides, Raman scattering cannot be blocked completely with emission filters because it overlaps with the wavelength range of the desired fluorescence light. This means that it is necessary to restrict the observed volume, typically to volumes below one femtoliter (i.e. $1\,\mu m^3$). This can be achieved either by confocal detection optics or by total internal reflection (TIR) illumination. TIR occurs when a beam of light strikes a medium boundary with a lower refractive index on the other side, at an angle larger than the critical angle. The critical angle θ_c can be found using Snell's law:

$$\theta_c = \arcsin\left(\frac{n_2}{n_1}\right) \tag{2.7}$$

with the refractive indices n_1, n_2 and $n_1 > n_2$.

In the case of TIR, an evanescent wave forms beyond the boundary with an exponential attenuation of the intensity in the direction normal to the interface:

$$I(z) = I_0 \ \exp(-z/d_0) \tag{2.8}$$

where I_0 is the intensity at the interface, z the distance to the interface and d_0 the decay constant (also called the "penetration depth") for the intensity, which is given by

$$d_0 = \frac{\lambda}{4\pi\, n_1}\left(\sin^2\theta_1 - \left(\frac{n_2}{n_1}\right)^2\right)^{-1/2} \tag{2.9}$$

with θ_1 being the incident angle. The penetration depth is typically in the range of 100 to 200 nm, thus effectively reducing the excited volume.

Another, inevitable challenge is the fact that single-molecule fluorescence kinetic measurements are generally "photon-starved" and noisy [8]. Current commercially available fluorophores will only emit on the order of 10^6 photons before they irreversibly photobleach. Even with high-NA objectives, not more than 10% of these photons may reach the detector and generate a signal. If these are distributed over 250 frames, only 400 photons will be collected during each acquisition. This already results in a relative standard deviation ($\sqrt{n}/n$) of 5% under optimal conditions and from photon statistics only.

2.4. Analysis of smFRET Time Trace Data

Single-molecule techniques can overcome the averaging inherent to ensemble measurements. From a "static" point of view, they can resolve different populations and their weights, where bulk experiments can only yield a population-weight average. Besides, single-molecule approaches can also uncover the dynamics of the system directly, without the need of synchronizing all molecules and studying the relaxation to the equilibrium. The relaxation methods with a spectroscopic readout (e.g. jump or stopped-flow techniques) can recover kinetic rates only in a simple two-state systems (e.g. one bound and one unbound state). In cases where more states or intermediates are involved, they yield only a complex mixture of the rate constants. In contrast, single-molecule experiments allow following each molecule separately and in real time, as they transition through their state network. From this sequence, the kinetic model – that fully describes the system – can be extracted. However the sequence of states (i.e. the conformational trajectory) is not directly accessible from a measurement because the signal is obscured by experimental shortcomings and a low signal-to-noise ratio (SNR).

In order to obtain time-resolved data, surface-immobilized molecules labeled with a FRET-pair can be studied with different types of setups, including confocal microscopes and setups with a total internal reflection geometry for excitation and a CCD camera for detection. Independent of the exact nature of the setup, single-molecule fluorescence intensity time traces in different spectral regions are acquired. By carefully choosing the labeling positions, conformational changes of the studied biomolecule result in a change of the distance between the fluorophores. This in turn changes the energy transfer rate and thus the observed FRET efficiency.

Using alternating laser excitation (ALEX) [59, 60], i.e. switching between excitation of the donor and the acceptor, allows one to exclude dye artifacts (e.g. dark states of the acceptor) and also to include regions of low FRET efficiency before bleaching of the donor that would be erroneously removed from the data otherwise. Besides, the additional information allows determining correction factors for setup and dye properties directly from the measured sample, via the stoichiometry versus FRET efficiency histogram – at least if two species with distinct FRET efficiency are present in the sample (see Section B.8.5 in the Appendix) [72]. The apparent stoichiometry (S_{app}) and FRET efficiency (E_{app}) are given by:

$$S_{app} = \frac{I_A^D + I_D^D}{I_A^D + I_D^D + I_A^A} \tag{2.10}$$

$$E_{app} = \frac{I_A^D}{I_A^D + I_D^D} \tag{2.11}$$

with the fluorescence intensity I_{em}^{ex} in detection channel em after excitation of ex.

Different approaches are used to analyze this kind of data. In most cases the smFRET efficiency trajectory is calculated from the fluorescence intensities of donor and acceptor according to Eq. (2.11) and a transformation from the continuous FRET efficiency space to the discrete state space is applied (discretization). This can be achieved for example by a simple threshold (i.e. an interval in the FRET efficiency is linked to a certain state) if states are well-separated, or by more advanced methods such as hidden Markov model analysis (HaMMy [80], QuB [106], vbFRET [14], SMART [37] and others [64]) or other maximum likelihood techniques [34]. Typically, dwell time histograms are then compiled from the resulting state trajectories and kinetic parameters are obtained by a single- or multi-exponential fit to these histograms.

However, the limitations of dwell time based approaches have been noticed already 30 years ago, in the patch-clamp field. For example, problems arise, when multiple states share the same signal level [48]. Besides, ambiguities may arise when trying to assign the rates to a kinetic model because the information on the cross-correlation between two adjacent events is not included in a normal one-dimensional dwell time histogram [9, 105].

2.5. Hidden Markov Models

To overcome the aforementioned shortcomings and to provide an unbiased way of state assignment *and* kinetic rate extraction from the data, a kinetic state model can be inferred directly from the recorded time traces using hidden Markov models (HMMs). The basis for each HMM is a Markov chain.

In a discrete-time Markov chain, the system is considered to be in one of a set of distinct states. At regularly spaced, discrete times, transitions from one to another state can occur according to the transition probability that is time-invariant and only depends on the current state [107]. This also means that the sequence of states in a Markov process is memoryless.

However, a Markov chain is not flexible enough to be applicable to the problem of interest. Additionally, the true state of the system is hidden and the actual observation (also called the “output”) is a probabilistic function of this hidden state. Hence, the resulting model – called HMM – consists of a doubly embedded stochastic process and fits a combined kinetic and noise model to the data [37]. Because the hidden states are linked to the output generated by an HMM by a probability distribution, the sequence of observations gives some information about the underlying sequence of states.

An HMM (Fig. 2.3) is characterized by the following elements: The initial state distribution $\boldsymbol{\pi}$, that gives the probabilities π_i for the system being in state i at the first time point of a time trace. The transition matrix $\boldsymbol{A}$, which contains the transition probabilities a_{ij} between all hidden states. And a set $\boldsymbol{B}$ of so-called emission probabilities, b_i, that link the hidden states to the observables.

The observation space can either be discrete (the HMM emits symbols or categories) or continuous. In the case of total internal reflection fluorescence (TIRF) microscopy smFRET data, the emission probabilities can be typically modeled sufficiently well by continuous Gaussian probability density functions, $\mathcal{N}(\boldsymbol{\mu}, \boldsymbol{K})$, with mean vector $\boldsymbol{\mu}$ and

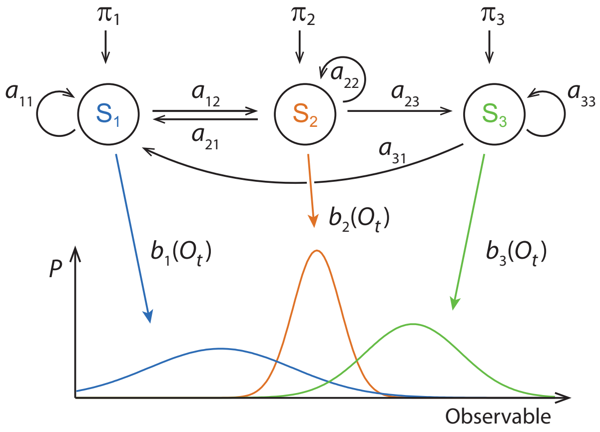

Figure 2.3: Probabilistic parameters of an exemplary hidden Markov model with continuous emission probabilities. States (S_i), initial probabilities π_i, transition probabilities (a_{ij}) and continuous emission probabilities ($b_i(O_t)$) are depicted. Transitions $\mathrm{S}_1 \rightarrow \mathrm{S}_3$ and $\mathrm{S}_3 \rightarrow \mathrm{S}_2$ are not possible in this exemplary HMM.

covariance matrix $\boldsymbol{K}$ [80, 115, 10] (see also Section 3.4.1 for the shape of experimental emission probabilities). Vector notation is used in this work. Thus, the formula are independent of the actual dimensionality of the observation.

HMMs are used in a number of applications including temporal (e.g. speech, handwriting, gestures) or sequential (e.g. gene prediction) pattern recognition. In time series analysis, they can be used for signal smoothing/filtering, decoding (i.e. finding the most probable trajectory of states that resulted in a signal) and prediction.

Three basic problems have to be addressed to make HMMs useful in real-world applications [107].

1. An efficient way of calculating the "goodness of fit" of a model, given a sequence of observations $\boldsymbol{O}$, is needed.
   The production probability $P(\boldsymbol{O}|\lambda)$ gives the probability that the observed sequence was produced by the model $\lambda = (\boldsymbol{\pi}, \boldsymbol{A}, \boldsymbol{B})$ and can be calculated by the forward-backward algorithm.

2. A way to select the most probable state trajectory that resulted in a given observation sequence is required.
   The Viterbi algorithm finds this sequence.

3. A method of optimizing the model parameters λ in order to maximize $P(\boldsymbol{O}|\lambda)$ is needed.
   The Baum-Welch algorithm offers a way to iteratively update the parameters until the maximum-likelihood solution is found.

Finally, in order to give error estimates for the parameters after the optimal values have been computed, their confidence intervals can be determined. These serve as a measure of the uncertainty of the extracted parameter.

2.5.1. Production Probability and Likelihood

Given an observation trajectory $\boldsymbol{O} = \{O_1, O_2, ..., O_T\}$ of length T, the “brute-force” approach to calculate the probability of the observation trajectory given the model, $P(\boldsymbol{O}|\lambda)$, is to enumerate all possible state trajectories $\boldsymbol{S} = \{s_1, s_2, ...s_T\}$ (where s_t indicates the state at time t) of the same length and to sum over their respective probabilities to occur and to produce the observation trajectory.

The probability for the emission of a specific observation trajectory given a state sequence and a model is:

$$P(\boldsymbol{O}|\boldsymbol{S}, \lambda) = \prod_{t=1}^{T} b_{s_t}(O_t) \tag{2.12}$$

with the probability $b_{s_t}(O_t)$ to emit the observation O_t from state s_t at time point t. The probability to generate a specific state trajectory given a model is:

$$P(\boldsymbol{S}|\lambda) = \pi_{s_1} \cdot \prod_{t=2}^{T} a_{s_{t\text{-}1}s_t} \tag{2.13}$$

with the transition probability $a_{s_{t\text{-}1}s_t}$ for the transition from state s_{t-1} at time point $(t-1)$ to state s_t at time point t. Then, the probability for a specific observation trajectory from a specific state trajectory is simply the product of the above two terms:

$$P(\boldsymbol{O}, \boldsymbol{S}|\lambda) = P(\boldsymbol{O}|\boldsymbol{S}, \lambda) \cdot P(\boldsymbol{S}|\lambda) = \pi_{s_1} \cdot \prod_{t=2}^{T} \left(a_{s_{t\text{-}1}s_t}\, b_{s_t}(O_t)\right) \tag{2.14}$$

Finally, the production probability is obtained by summing over all possible state sequences (since each of these can produce the observation trajectory $\boldsymbol{O}$):

$$P(\boldsymbol{O}|\lambda) = \sum_{\text{all } \boldsymbol{S}} P(\boldsymbol{O}, \boldsymbol{S}|\lambda) = \sum_{\text{all } \boldsymbol{S}} \left(\pi_{s_1} \cdot \prod_{t=2}^{T} \left(a_{s_{t\text{-}1}s_t}\, b_{s_t}(O_t)\right)\right) \tag{2.15}$$

However, this calculation is computationally unfeasible. A more efficient way is the forward-backward algorithm. Here, one uses the fact that for a state s_{t+1} only the states at the preceding time point t are relevant (Markov property). This means that all calculations can be done along the time axis and in parallel for all states, which cuts computational complexity considerably. The forward and backward variables $\alpha_t(i)$ and $\beta_t(i)$ give the probability of the partial observation sequence from the beginning until time t or from time $t+1$ until the end, respectively. They are calculated inductively as follows (i, j denote states):

1. Initialization

$$\alpha_1(i) = \pi_i\, b_i(O_1) \tag{2.16}$$

$$\beta_T(i) = 1 \tag{2.17}$$

2. Induction
   for $1 \leq t \leq T-1$

$$\alpha_{t+1}(i) = \left(\sum_j \left(\alpha_t(j) \; a_{ji} \right) \right) b_i(O_{t+1}) \tag{2.18}$$

$$\beta_t(i) = \sum_j \left(\, a_{ij} \; b_j(O_{t+1}) \; \beta_{t+1}(j) \, \right) \tag{2.19}$$

3. Termination

$$P(\boldsymbol{O}|\lambda) = \sum_i \alpha_T(i) \tag{2.20}$$

$$P(\boldsymbol{O}|\lambda) = \sum_i \left(\, \pi_i \; b_i(O_1) \; \beta_1(i) \, \right) \tag{2.21}$$

Finally, the production probability is identical to the likelihood of the model, given the data: $P(\boldsymbol{O}|\lambda) = \mathcal{L}(\lambda|\boldsymbol{O})$.

2.5.2. Viterbi Algorithm

The single best state trajectory $\boldsymbol{S}^*$ for a given observation and a given model can be found using the Viterbi algorithm. It maximizes $P(\boldsymbol{S}|\boldsymbol{O}, \lambda)$ over the entire observation trajectory and not for each time point individually. $\boldsymbol{S}^*$ is also called the Viterbi path. The procedure is similar to the forward algorithm, with the major difference being the maximization over previous states instead of a summation. From a signal processing point of view, this step "decodes" the noisy input signal (i.e. the observation) and yields a noise-free state trajectory.

The variable $\delta_t(i)$ stores the probability of the most likely (partial) path that ends in state i at time point t and the variable $\psi_t(i)$ stores the associated optimal predecessor state for each state i at time t.

1. Initialization

$$\delta_1(i) = \pi_i \; b_i(O_1) \tag{2.22}$$

$$\psi_1(i) = 0 \tag{2.23}$$

2. Induction
   for $1 \leq t \leq T-1$

$$\delta_{t+1}(j) = \max_i [\delta_t(i) \; a_{ij}] \cdot b_j(O_{t+1}) \tag{2.24}$$

$$\psi_{t+1}(j) = \operatorname*{argmax}_i [\delta_t(i) \; a_{ij}] \tag{2.25}$$

3. Termination

$$P^*(\boldsymbol{O}|\lambda) = P(\boldsymbol{O}, \boldsymbol{S}^*|\lambda) = \max_i[\delta_T(i)] \tag{2.26}$$

$$s_T^* = \operatorname*{argmax}_j[\delta_T(j)] \tag{2.27}$$

4. Path backtracking
   for $1 \leq t \leq T-1$

$$s_t^* = \psi_{t+1}(s_{t+1}^*) \tag{2.28}$$

2.5.3. Baum-Welch Algorithm

The last problem is to adjust the model parameters $\lambda = (\boldsymbol{\pi}, \boldsymbol{A}, \boldsymbol{B})$ in order to maximize the production probability. This is also known as "training" the HMM. There is no known way to analytically solve for the model which maximizes the probability of the observation sequence [107]. However, an iterative procedure – called Baum-Welch algorithm – exists that locally maximizes $P(\boldsymbol{O}|\lambda)$. The basis for calculating the updated parameters are the quantities $\gamma_t(i)$ and $\gamma_t(i,j)$, the probabilities for a given state or transition at a given time point, respectively. Summation over time then yields the expected number of transitions starting in state i and transitions from state i to state j.

$$\gamma_t(i) = P(s_t = i|\boldsymbol{O}, \lambda) \qquad = \frac{\alpha_t(i)\ \beta_t(i)}{P(\boldsymbol{O}|\lambda)} \tag{2.29}$$

$$\gamma_t(i,j) = P(s_t = i, s_{t+1} = j|\boldsymbol{O}, \lambda) = \frac{\alpha_t(i)\ a_{ij}\ b_j(O_{t+1})\ \beta_{t+1}(j)}{P(\boldsymbol{O}|\lambda)} \tag{2.30}$$

The emission probability b_i of state i is given by the continuous Gaussian probability density function $\mathcal{N}(\boldsymbol{\mu}_i, \boldsymbol{K}_i)$, with mean vector $\boldsymbol{\mu}_i$ and covariance matrix $\boldsymbol{K}_i$. The re-estimation formulas for the updated model parameters $\hat{\lambda} = (\hat{\boldsymbol{\pi}}, \hat{\boldsymbol{A}}, \hat{\boldsymbol{B}})$ are:

$$\hat{\pi}_i = \gamma_1(i) \tag{2.31}$$

$$\hat{a}_{ij} = \frac{\sum_{t=1}^{T-1} \gamma_t(i,j)}{\sum_{t=1}^{T-1} \gamma_t(i)} \tag{2.32}$$

$$\hat{\boldsymbol{\mu}}_i = \frac{\sum_{t=1}^{T} \gamma_t(i)\ O_t}{\sum_{t=1}^{T} \gamma_t(i)} \tag{2.33}$$

$$\hat{\boldsymbol{K}}_i = \frac{\sum_{t=1}^{T} \left(\gamma_t(i)\ O_t O_t^{\mathsf{T}}\right)}{\sum_{t=1}^{T} \gamma_t(i)} - \boldsymbol{\mu}_i \boldsymbol{\mu}_i^{\mathsf{T}} \tag{2.34}$$

In order to combine the information from more than one observation trajectory, the ensemble parameters $\pi_i^{\varnothing}$, $a_{ij}^{\varnothing}$ are updated based on all N molecules, assuming that there is no significant heterogeneity in the single-molecule behavior between the molecules in the data set. Since the re-estimation formulas are based on frequencies of occurrence, this is done by summation over all molecules:

$$\hat{\pi}_i^{\varnothing} = \frac{1}{N}\sum_{n=1}^{N} {}^n\hat{\pi}_i \tag{2.35}$$

$$\hat{a}_{ij}^{\varnothing} = \frac{\sum_{n=1}^{N}\left(\sum_{t=1}^{T-1} {}^n\gamma_t(i,j)\right)}{\sum_{n=1}^{N}\left(\sum_{t=1}^{T-1} {}^n\gamma_t(i)\right)} \tag{2.36}$$

The left superscript denotes the n-th molecule in the data set.

By iterating the Baum-Welch algorithm until $\mathcal{L}(\lambda'|\boldsymbol{O})$ converges, the maximum likelihood estimator (MLE) of the parameters are found.

2.5.4. Confidence Intervals

After having obtained the MLE of the parameters, one is also interested in their uncertainty. In the framework of HMMs this means: how much variation is allowed in a parameter without significant changes in the likelihood of the model? A typical approach is to calculate the confidence interval (CI). The CI is the range that encloses the true parameter with a certain frequency, namely the confidence level (e.g. 95%). In other words, if a parameter is obtained from each of an infinite number of independent repetitions of an experiment and the CI is constructed for each of these parameters, then the fraction of these CI that contain the true value of the parameter will equal the confidence level [38].

The CI of a parameter can be estimated by examining the likelihood profiles around the MLE of this parameter. The method of likelihood profiling relies on finding a value of the parameter of interest that results in a significant change in the log-likelihood [83, 137, 37]. To obtain this profile, the parameter under consideration is fixed at some value around the MLE, the other parameters are re-estimated and the new likelihood $\mathcal{L}(\lambda'|\boldsymbol{O})$ with the modified model λ' is calculated. This can be compared to the MLE model with a likelihood ratio (LR) test.

$$LR = 2\left(\ln\mathcal{L}(\lambda_{\mathrm{MLE}}|\boldsymbol{O}) - \ln\mathcal{L}(\lambda'|\boldsymbol{O})\right) \tag{2.37}$$

LR is approximately χ^2-distributed with df degrees of freedom, where df is the difference between the degrees of freedom of λ_{MLE} and λ'. Here, $df = 1$ because only one parameter is fixed [31, 137]. The confidence bound for the parameter is reached when LR exceeds the quantile given by the desired confidence level of a χ^2-distribution with one degree of freedom. E.g., for a 95% (99%) CI, this value is 3.841 (6.635). Finding such values on both sides of the MLE of a parameter then results in the CI.

2.6. Quantitative Kinetic Analysis of Two-Color smFRET Data

Main parts of this section are published in Schmid, Götz & Hugel (2016) [115].

In this section, the thorough implementation of a maximum-likelihood approach using

HMM to analyze two-color smFRET time traces of a protein system is summarized. The single-molecule analysis of complex kinetic sequences (SMACKS) is a simple and robust technique for extracting kinetic state models and thermodynamic quantities.

As stated above, the typical approach to analyze time traces obtained from measurements with surface-tethered molecules and a TIRF microscope to date is to deduce state trajectories from the smFRET trajectories and to obtain kinetic information from exponential fits to the respective dwell time histogram of every observed state [80, 14, 37]. However, this analysis only gives unbiased results when every state has a characteristic emission which is distinct from the other states and all transition rates are on the same time scale. In this case, there is a sampling rate at which every state is reached many times before irreversible photobleaching of one of the fluorophores. Both requirements may be broken by proteins, which typically show dynamics on diverse time scales and conformations that are experimentally indistinguishable but differ kinetically [27, 132, 44]. This leads to multi-exponential dwell time distributions. The interpretation of such distributions may result in erroneous conclusions because the way the states are connected in the state model is completely ignored by a dwell time analysis.

Besides, enzymatic antibleaching agents (such as oxygen scavenger systems consisting of glucose oxidase, catalase and Trolox [11, 1]), which largely increase the observation time of DNA-based samples, are much less effective for protein systems. What is more, their use with protein systems – and especially a molecular chaperone like Hsp90 – is problematic, as they may contain proteins up to a micromolar concentration [133] and might interact non-specifically with the protein under study. As a consequence, the detection bandwidth for protein samples spans less than a factor of 200 at a reasonable signal/noise ratio – independent of the sampling rate applied. In this situation, the classical dwell time analysis overestimates transition rates systematically, because predominantly long dwell times are missed.

In contrast, SMACKS implements a two-step protocol to extract the kinetic information. In the first step, the emission probability density functions (PDFs) for all experimentally distinguishable states are determined individually for each molecule. This takes into account the experimental heterogeneity in the signal levels that exists in single-molecule data. Also, the HMM is trained with the original two-dimensional signal (fluorescence intensity of donor and acceptor after donor excitation) instead of the FRET efficiency. This significantly increases the robustness with respect to uncorrelated noise.

Molecules that do not show any detectable state transition during the observation time ("static traces") can be included in the analysis, too. In a system with fast and slow processes, a fast sampling is needed to resolve all transitions. However, this also means that the slow processes may not be sampled long enough (e.g. up to five times the lifetime of the slowest transition) due to photobleaching and the accompanying finite observation time of the experiment. Nevertheless, these static traces contain kinetic information. Because a model with more than one state would not converge to a meaningful solution for these molecules, the mean emission PDF of the remaining data set is used.

In the second step, an ensemble HMM run is performed to optimize the initial state distribution $\boldsymbol{\pi}^{\varnothing}$ and the transition matrix $\boldsymbol{A}^{\varnothing}$ based on the *entire* data set while holding the predetermined, individual emission PDFs fixed (see Fig. 2.4A). The kinetic parameters are then directly obtained from the transition matrix, without the detour via dwell time histograms.

The dwell time histograms might not be mono-exponentially distributed (such as in the case of Hsp90). This suggests the presence of more states than are experimentally distinguishable from the observation signal. In this situation, states with "degenerate" FRET efficiency can be included in the HMM.

Differently sized models can be compared (see Fig. 2.4B), relative to each other, using the Bayesian information criterion (BIC) [122]:

$$\mathrm{BIC} = -2\ \ln \mathcal{L}(\lambda|\boldsymbol{O}) + k \cdot \ln n \tag{2.38}$$

Here, k is the number of free parameters and n is the number of data points. Increasing the number of parameters of a model can also increases the goodness of fit (i.e. the likelihood of the model). However, this may result in overfitting. By balancing the likelihood against the number of free parameters, the information criterion selects for a model that describes the data well, while at the same time is not unnecessarily complex. The BIC is commonly used in model selection problems, also with single-molecule time trace data [6, 80, 74, 37].

The model with the optimal number of states can be further refined (see Fig. 2.4C), e.g. by omitting transitions that do not occur in the data. To this end, the transition histogram is compiled from the Viterbi paths.

Finally, several means of model evaluation including error quantification are possible within this framework (see Fig. 2.4D). First, an illustrative test for the consistency of the trained model with the original experimental data is "re-simulation" using the optimized transition matrix, the bleach rate and the emission probabilities of the states. State trajectories are obtained by a Monte Carlo simulation and then "translated" to synthetic time traces. Thus, simulated dwell time or FRET efficiency histograms can be compared with the measurement. Second, the convergence of the HMM to the global maximum is tested by using random start parameters for the transition matrix [91]. Additionally, sampling random subsets of the data (e.g. 66% of the molecules) reveals the heterogeneity of the data set. Third, the confidence interval is calculated for every transition probability. It reports on precision of the HMM considering the data set size and heterogeneity and the experimental noise.

Being able to resolve the kinetic state model in turn allows one to address the question of (energy) flow and directionality in any network with more than two states. Note that any time-homogeneous Markovian analysis requires stationarity – but not thermodynamic equilibrium. The free energy difference over a closed cycle is given by

$$\Delta G_{\mathrm{cyc}} = -k_B T\ \ln\left(\frac{a_{c_1c_2} \cdot a_{c_2c_3} \cdots a_{c_kc_1}}{a_{c_2c_1} \cdot a_{c_3c_2} \cdots a_{c_1c_k}}\right) \tag{2.39}$$

for the cycle of states $(c_1, c_2, ..., c_k)$ and the transition probabilities $a_{c_ic_j}$ from state c_i to c_j [50, 46].

If no external energy source (i.e. ATP) is present in the experiment, the system has to be in thermal equilibrium. The HMM then satisfies detailed balance, i.e. does not

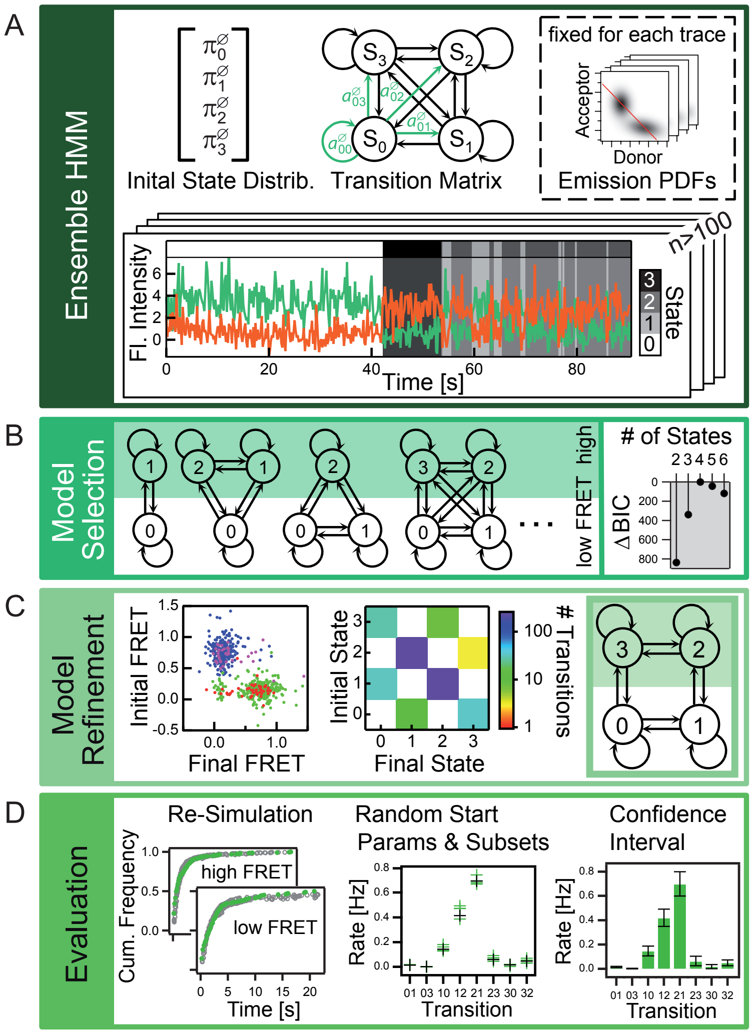

Figure 2.4: SMACKS workflow. (A) Components of the ensemble HMM run: initial probability $\boldsymbol{\pi}^{\varnothing}$, transition matrix $\boldsymbol{A}^{\varnothing}$ and individual emission PDFs for each molecule. Fluorescence intensity time traces of donor (green) and acceptor (red) are used as input. (B) Degenerate states are included by duplicating the emission PDFs of the experimentally discernible states (here, low FRET and high FRET). The relative difference in the BIC identifies the optimal number of states (here, four). (C) The transition map (left) relates the mean FRET efficiency before and after each transition found by the Viterbi algorithm. The transition histogram (middle) reveals the frequency of each transition in the data set. Excluding transitions that do not occur leads to a refined, cyclic model (right). (D) Model evaluation. First, dwell time distributions can be reproduced by re-simulation (left). Simulated data (gray) fits the experimental data (green) well. Second, random start parameters uncover potential local likelihood maxima and random subsets reveal data set heterogeneity (middle, subsets (green), complete set (black)). Third, confidence intervals measure the uncertainty of the obtained rates (right). Figure based on Ref. [115].

change under time reversal. This implies that, around any closed cycle of states i and j, there is no net flow:

$$\pi_i \, a_{ij} = \pi_j \, a_{ji} \tag{2.40}$$

where $\boldsymbol{\pi}$ is the stationary distribution of the Markov chain.

Even if the data arises from a system in thermal equilibrium, the MLE most likely yields transition probabilities that almost – but not exactly – satisfy detailed balance. Following the approach in Ref. [37], detailed balance can be imposed by averaging the transition matrix with its time-reversed version $\boldsymbol{A}_{\text{rev}}$:

$$\boldsymbol{A}_{\text{rev}} = \left\{ a_{ij} \frac{\pi_i}{\pi_j} \right\} \tag{2.41}$$

A transition matrix that satisfies detailed balance ($\boldsymbol{A}_{\text{db}}$) is then calculated by

$$\boldsymbol{A}_{\text{db}} = \frac{\boldsymbol{A} + \boldsymbol{A}_{\text{rev}}}{2} \tag{2.42}$$

In summary, SMACKS incorporates all features that are necessary for a detailed kinetic description of a protein system from smFRET time traces. Including states that share the same signal but differ kinetically and extracting the kinetic information directly from the HMM helps to analyze real-world protein systems which commonly adopt more than two states. By taking into account every experimental data point – not only dwell times – SMACKS prevents the systematic overestimation of transition rates, especially in the case of processes that are slow compared to the sampling rate.

3. Quantitative Kinetic Analysis of Multi-Color smFRET Experiments

Using conventional two-color smFRET experiments with a TIRF microscope imposes a strong limitation on the questions one can address. By observing the energy transfer between one dye pair (and thus tracking only one distance) it is impossible to observe the correlation of different conformational changes. What is more, most proteins do not work by themselves, but they rely on the interplay with other components of the cell [2]. Therefore, it is of interest to observe more than one process at a time, e.g. the binding of an interaction partner and a (potentially correlated) conformational change. Hence, naturally, the need to extend smFRET experiments and analysis by at least one more color arises. This multi-color approach literally adds a new dimension to the technique of smFRET and helps to tackle the complexity of multi-component protein systems [47, 71, 35].

Conceptually new effects or properties of the system under study can be observed with multi-color smFRET experiments: First, it becomes possible to test for synergistic or cooperative effects of binding events and/or conformational changes. Second, a higher-dimensional state space may lead to more states being distinguishable with separating states that were “degenerated” in a common two-color experiment. Also the sequence of distinct events can be assayed. This results in, third, the increased possibility to observe systems that work out of equilibrium (i.e. are coupled to an energy source) and thus show a net flow through a network of states.

The aim of this part of the work was to extend the existing two-color smFRET TIRF experiment analysis methods and software tools to multi-color experiments that are suited for the Hsp90 system.

3.1. Redesign of a Four-Color smFRET TIR Setup

The work described in this section was conducted in collaboration with Philipp Wortmann and main parts are published in Götz, Wortmann, Schmid & Hugel (2016) [35].

An existing four-color smFRET TIRF setup (originally designed and built by Christoph Ratzke [110]) was redesigned and built after relocating from Munich to Freiburg (see Fig. 3.1A and [35]). Several improvements were implemented and key components were replaced by new parts. This includes the objective, the tube lens, dichroic mirrors and filters in the detection paths and the EMCCD cameras.

The beams of four lasers at the wavelengths 473 nm (Cobolt Blues 50 mW, Cobolt), 532 nm (Compass 215M 75 mW, Coherent), 594 nm (Cobolt Mambo 100 mW, Cobolt) and 637 nm (LPM635-25C 25 mW, Newport) are expanded and collimated individually by Keplerian telescopes and subsequently overlaid using dichroic mirrors. Fine adjustments of the laser path can be done with Picomotor piezo mirror mounts (New Focus, Newport).

An iris selects the central part of the beam to obtain homogeneous illumination. An acousto-optical tunable filter (AOTFnC-Vis, AAOptics) is used to control the excitation power and allows fast switching of the different excitation colors. Additional mechanical shutters (SH1, Thorlabs) in each beam ensure that the excitation is blocked completely for measurements on a slower time scale ($> 20\,\mathrm{ms}$). The combined excitation beam is circularly polarized by a $\lambda/4$ plate (AQWP05M-600, Thorlabs) and focused on the quartz-buffer interface of the measurement chamber by an achromatic lens via a quartz prism. This results in an excitation with total internal reflection (TIR) geometry. An asymmetric, elongated prism is used in order to prevent the back reflection of the excitation beam from the rear side of the prism to enter the objective. The total excitation power before entering the prism is typically in the range of 1–3 mW.

The emitted fluorescence is collected by a high-NA oil immersion objective with 100× magnification (CFI Apo TIRF 100×, Nikon) and the image is not further magnified in the detection path. The objective is mounted on a micrometer stage and a Piezo Focus Positioner (MIPOS 250 CAP, piezosystem jena) for precise focusing. The tube lens is positioned as close as possible to the objective (which is also in accordance with the tube lens focal length of Nikon objectives, 200 mm) to prevent loss of off-center fluorescence light. The final pixel size of the setup is close to the theoretical value with 162, 162, 158, and 159 nm per pixel for the detection channels in the order of increasing wavelength (corresponding to a magnification of 99×, 99×, 101× and 101×, respectively; determined with a calibration target and a torch; R1L3S2P, Thorlabs).

In the detection paths, achromatic aspheric lenses with 50 mm diameter and a focal length of 200 mm (G322-304-000, Qioptiq) are used in order to collect as much light as possible and to prevent aberrations, e.g., distortions in off-center regions of the image.

An adjustable optical slit (Owis GmbH) is placed in the intermediate image plane to adjust the field of view and to remove off-axis beams. The light is collimated again and spectral regions are separated into the different detection channels with dichroic mirrors. Each channel is focused with a separate lens onto the chip of the respective EMCCD camera (iXon Ultra 897, Andor). Bandpass filters decrease the leakage of fluorescence from other dyes (see Fig. 3.1B). Spectral regions of the filters were also selected in a way that the main Raman peak of water is excluded from any channel as far as possible. Mechanical shutters in the blue and orange detection channels (Uniblitz VS35, Vincent Associates) can block excitation light from the corresponding excitation laser. One camera is used per two detection channels that are imaged side by side. The orientation of the camera was chosen in a way that channels do not overlap during readout.

Shutters, AOTF, and cameras are synchronized by TTL signals from a digital I/O card (PCIe-6535, National Instruments) that is controlled by PC software developed with Labview (National Instruments).

For simplification the corresponding excitation and emission channels are refereed to with the same identifier (i.e. “blue”, “green”, “orange” or “red”) in this work.

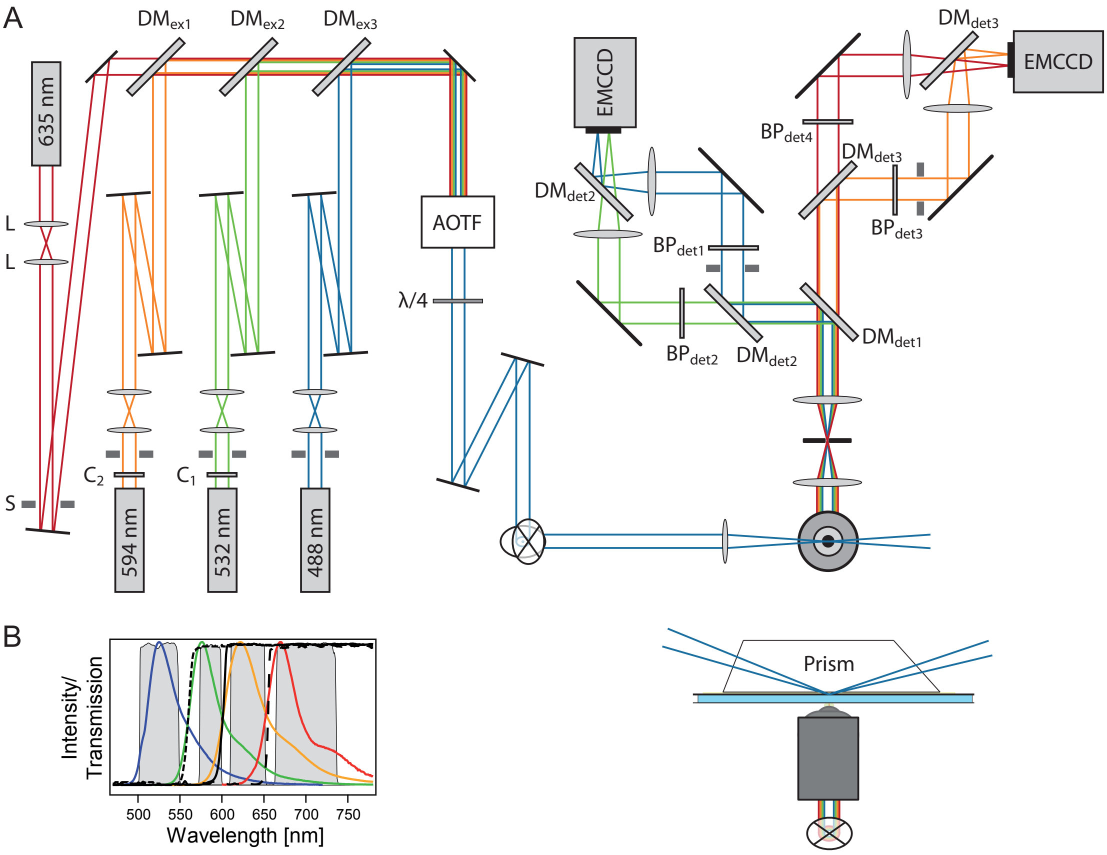

Figure 3.1: Scheme of the multi-color smFRET setup. (A) The position of the elements roughly corresponds to the real layout. S: mechanical shutter, C: clean-up filter (C_1: ZET532/10, C_2: ZET 594/10), DM: dichroic mirrors (DM_{ex1}: ZQ594RDC, DM_{ex2}: 570DCXR, DM_{ex3}: ZT491RDC, DM_{det1}: T 600 LPXR, DM_{det2}: H 560 LPXR superflat, DM_{det3}: HC BS R635), BP: bandpass filter (BP_{det1}: 525/40 BrightLine HC, BP_{det2}: 586/20 BrightLine HC, BP_{det3}: 631/36 BrightLine HC, BP_{det4}: 700/75 ET Bandpass). All filters and dichroic mirrors were purchased from AHF analysentechnik. (B) The emission spectra of the utilized fluorescent dyes (left to right) Atto488 (blue), Atto550 (green), Atto594 (orange), Atto647N (red), and the transmission spectra of the bandpass filter (gray) and the transmission spectra of the dichroic mirrors (bold black lines). Spectral information provided by Atto-Tec and AHF analysentechnik. Figure based on Ref. [35].

3.2. Measurement and Calculation of the Partial Fluorescence Traces

Main parts of this section are published in Götz, Wortmann, Schmid & Hugel (2016) [35].

Expression, purification and fluorescence labeling of the sample protein is described in Sections B.2 and B.4 in the Appendix.

3.2.1. Monomer Exchange

In order to form heterodimers of Hsp90 labeled with Atto488 at amino acid position D61 and Atto550 at amino acid position Q385, a 10:1 mixture of the variants with a total protein concentration below 10 µM is incubated at 47°C for 30 min. This allows exchanging of the Hsp90 subunits by destabilizing the C-terminal coiled-coil motif ("Czip") that extends the C-terminus in order to prevent dimer dissociation at picomolar concentrations used in single molecule experiments [85]. Potential aggregates are removed by centrifugation at $14'000 \times g$ at 4°C for at least 30 min. Exchanging with a 10× excess of D61C-Atto488 will result in mainly heterodimers observed in the measurement chamber, as immobilization on the surface is achieved by biotin-Neutravidin interaction and only Q385C-Atto550 is biotinylated.

3.2.2. Data Acquisition

The sample is studied in a custom-built flow-chamber, which is a sandwich of a quartz slide (Finkenbeiner), a sealing film (Tegaderm, 3M) sprayed with Photomount (3M) on the non-adhesive side and a high precision cover slip (LH26.1, Carl Roth). The quartz slide is passivated with a layer of methoxy-/biotin-PEG. Thick (3 mm) quartz slides are employed in order to prevent the scattering at the quartz-glycerol-quartz boundary between the prism and the functionalized quartz slide to be near the imaged area. The Tegaderm film is used because it is thinner than e.g. Nesco film. The TIR illumination necessitates to have the attachment of the molecule of interest on the opposite site of the flow-chamber as the objective. Thus, a thin chamber is of advantage for collecting a maximal amount of fluorescence light. A syringe pump (PHD22/2000, Harvard Apparatus) allows exchanging of buffer and flushing in interaction partners.

The measurement chamber is "pre-bleached" to remove any fluorescent contaminants on the surface by slowly moving along the complete detection range of the slide with a laser power of about 10 mW for all lasers.

The single-molecule FRET experiments are conducted under ALEX and the resulting fluorescence in the respective emission channels is detected with EMCCD cameras. The CCD sensor is cooled down as far as possible (-95°C with external water cooling) to decrease the dark current noise. Camera settings are optimized for single-molecule recording: 3.3 µs vertical shift speed, normal vertical clock voltage, 17 MHz 16-bit horizontal read out, pre-amplification gain 3 and electron multiplier gain 1000. The overall time resolution of the presented three-color experiments is 200 ms per excitation cycle, with each excitation lasting 70 ms plus 30 ms read-out time.

3.2.3. Selection of Single-Molecule Traces

The recorded movies are split into the respective detection channels and individual molecules are identified by searching for the brightest spots in a channel. The corresponding position for all other detection channels is calculated using a channel mapping created from images of fluorescent beads. Fluorescence intensity time traces are then extracted by binning of 5×5 pixels around the central coordinates in each channel and frame. The binning corresponds to an area of approximately 800×800 nm for the magnification of the setup and was determined empirically to give the best SNR.

Intensity traces are corrected for an offset originating from the dark current of the EMCCD and background fluorescence. This is done by automatically subtracting a background time trace that is the mean intensity of the 200 darkest pixels in each channel. This global background correction is refined by subtracting the average intensity of a manually selected interval, where all fluorophores are bleached already. The advantage of this approach is that it permits subtracting a time-dependent background originating from residual fluorescent contamination that bleaches during acquisition and at the same time correcting for a local offset in the fluorescence intensity.

For each molecule, a joint raw intensity trace is calculated as the sum of all traces with the same excitation color. Traces are selected according to the following criteria: The joint raw intensity trace should have a roughly flat plateau, a single bleaching step, and the appropriate channel intensities have to show anti-correlated behavior.

As the aim of this work is to characterize nucleotide binding to Hsp90, only traces exhibiting intermittent red fluorescence after blue or green excitation, indicating the presence of Atto647N-labeled AMP-PNP (AMP-PNP*), are selected. About 200 spots in each detection channel of a movie are tested for single-molecule behavior.

Additionally, molecules that show two intensity levels in the detection channel for the labeled nucleotide are excluded, indicating that two AMP-PNP* might be bound to the Hsp90 dimer at the same time.

In the analysis, it is assumed that the nucleotide-coupled Atto647N does not bleach within the duration of a binding event since it is the most photo-stable of the three dyes. Moreover, AMP-PNP is not hydrolyzable by Hsp90. Thus, a loss of Atto647N fluorescence is treated as unbinding of the labeled nucleotide.

3.2.4. Calculation of the Partial Fluorescence Traces

Due to experimental shortcomings the measured fluorescence intensities depend not only on the energy transfer but also on fluorophore and setup properties. In order to obtain the true energy transfer efficiency between two fluorophores, the measured intensities have to be corrected for the following systematic deviations:

1. Upon donor excitation a small fraction of photons excite the acceptor dye directly. This is referred to as direct excitation.

2. A fraction of the photons emitted by the donor are detected in the channel for acceptor fluorescence. This is commonly referred to as leakage.
3. The fluorophores have different quantum yields and the detection of photons from different dyes depends on the detection efficiency of the setup in each detection channel.

For a two-color experiment the corresponding correction factors can be obtained from stoichiometry vs FRET efficiency (SE) plots based on experiments with ALEX [59, 60].

However, this correction method is not generally suited for multi-color FRET experiments, because the full ALEX information, i.e. subsequent excitation with all colors, might not be accessible anymore. This may be the case when the experimental conditions require a labeled species that is free in solution at concentrations above 10 nM. Then, the high background signal from molecules that are not immobilized to the surface prevents acquisition in this channel. Nevertheless, correcting the recorded intensities is advantageous for the discrimination between different populations and the comparison of multi-color FRET experiments with two-color experiments.

Correction factors for apparent leakage (lk) and apparent gamma (ag) can be calculated from single-molecule traces that show an acceptor bleaching event (see Fig. 3.2A). The correction factors are determined independently with a high-FRET dsDNA sample for each dye in combination with the acceptor having the longest excitation wavelength (Atto488-Atto647N, Atto550-Atto647N, Atto594-Atto647N).

The leakage of the donor dye into every possible acceptor channel is calculated from all data points in the recorded FRET traces where the acceptor dye is bleached but the donor is still fluorescent (${}^{\dagger}I$):

$$lk_b^a = \frac{{}^{\dagger}I_b^a}{{}^{\dagger}I_a^a} \tag{3.1}$$

with I_{em}^{ex} being the intensity in the detection channel em after excitation with color ex. The median of the leakage factor histogram is used as the apparent leakage factor (Fig. 3.2B).

After correction for leakage, the apparent gamma factor is determined from the same set of traces. It is calculated by dividing the change of fluorescence in the acceptor channel by the change of fluorescence in the donor channel upon bleaching of the acceptor dye:

$$ag_a = \frac{\Delta I_c^a}{\Delta I_a^a} = \frac{I_c^a - {}^{\dagger}I_c^a}{I_a^a - {}^{\dagger}I_a^a} \tag{3.2}$$

Here, c denotes the detection channel of the acceptor with the longest wavelength (i.e. Atto647N). The median of the apparent gamma factor distribution is used as an apparent correction factor (Fig. 3.2B). The apparent gamma factor for an arbitrary FRET pair combination is then approximated by the ratio between the two apparent gamma factors of the dyes measured in combination with Atto647N. The determined apparent correction factors lk and ag include a small contribution from the direct excitation and are therefore not completely independent of the FRET efficiency.

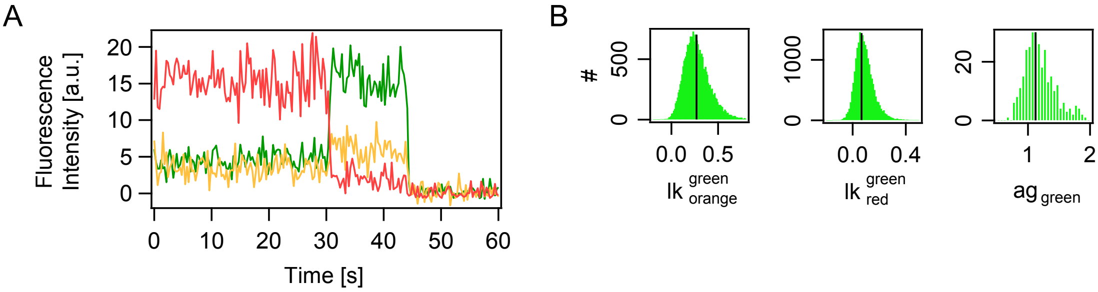

Figure 3.2: Determination of correction factors from a calibration sample with acceptor dye bleaching. (A) Representative fluorescence intensity trace of a dsDNA high-FRET sample labeled with Atto550 and Atto647N. Consecutive acceptor ($t \approx 30\,\mathrm{s}$) and donor bleaching ($t \approx 45\,\mathrm{s}$) is observed. Intensities for the green, orange, and red detection channel are shown. (B) Histograms for the correction factors from about 1000 molecules. The median (black bar) of the distribution for the apparent leakage and gamma factors is used. Figure adapted from Ref. [35].

Finally, the corrected intensity in each channel is obtained by:

$$ {}^{\mathrm{corr}}I_b^a = \left(I_b^a - \sum_{i=a}^{b-1} I_i^a \cdot lk_b^i \right) \cdot ag_b \tag{3.3}$$

with the sum over all detection channels with shorter wavelength than the channel that is corrected and the apparent gamma factor for the Atto647N detection channel $ag_c := 1$.

In multi-color FRET measurements, the energy from one donor fluorophore is transferred to different acceptor fluorophores. The rates for the transfer to all other fluorophores are independent and the signal in each detection channel results from the sum of all energy transfers to the respective acceptor fluorophore. Therefore, the partial fluorescence PF_{em}^{ex} is used as a proxy for the energy transfer between two fluorophores, where ex is the excitation channel and em is the emission channel. It is defined as:

$$ PF_b^a = \frac{{}^{\mathrm{corr}}I_b^a}{\sum_{i=a}^{c} {}^{\mathrm{corr}}I_i^a} \tag{3.4}$$

Since the donor may transfer energy to different acceptor dyes in multi-color FRET experiments, the relative position of all dyes is not accessible from excitation of the donor alone. ALEX overcomes this limitation.

3.3. General Approach of the Kinetic Analysis

One decisive difference of SMACKS (Section 2.6) compared to many other two-color smFRET implementations is the fact that it exploits the fluorescence intensities (two observables, namely donor and acceptor fluorescence) instead of the FRET efficiency (one observable). This renders the signal more robust with respect to uncorrelated noise that otherwise results in spikes in the FRET efficiency [115].

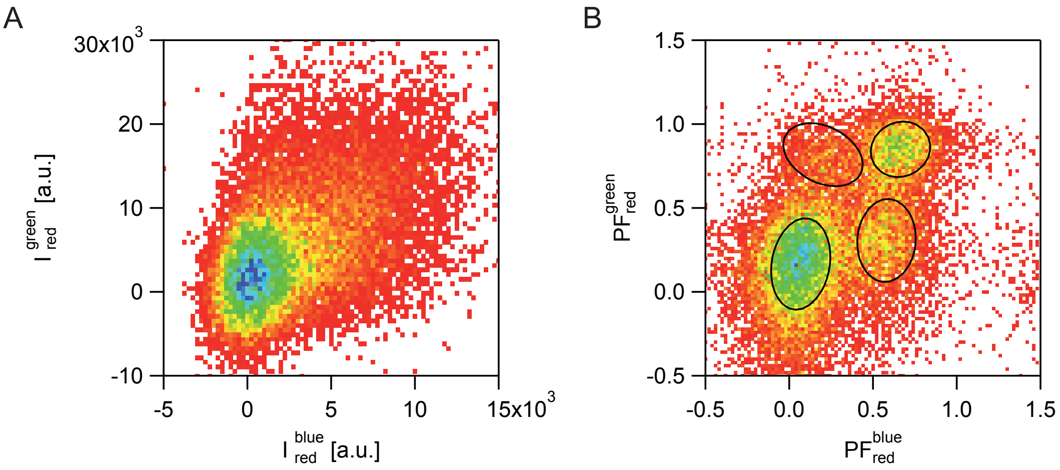

Figure 3.3: Fluorescence intensities are too diverse in a three-color experiment to give a reliable basis for state assignment. (A) Fluorescence intensities in the red channel after blue or green excitation, I_{red}^{blue} and I_{red}^{green} respectively, for a typical three-color experiment. (B) The PFs of the same data scatter less drastically and allow identifying four separate states (indicated by black ovals) in this projection of the actual three-dimensional PF space.

Unfortunately, this approach does not work "out of the box" for multi-color experiments. First, the number of intensity traces that have to be taken into account increases to five (three from the excitation of the dye with the smallest absorption wavelength and two from the dye with mid-wavelength absorption) for a three-color experiment and to nine for a four-color experiment. Working with a signal of such high dimensionality is not feasible since straightforward ways of simultaneous display are limited to three dimensions. Second, an even broader variation for fluorescence intensity levels is observed in three-color experiments, leading to two-dimensional histograms that do not allow to discern states from the fluorescence intensity, while different states can be distinguished in the PF histogram (see Fig. 3.3).

The general approach to analyze three-color smFRET data applied in this work is depicted in Figure 3.4. In short, from 2D projections of the 3D PF histogram, the relative population for all distinguishable states (five in this case) is determined. The relative population weights serve as constraints for a fit to the 3D histogram with the sum of five Gaussian functions. These are used as emission PDFs of the states. The rationale and implications of this procedure are presented in more detail in Section 3.4.

In a second step, an HMM is optimized over the complete data set (Section 3.5). This allows one to extract the kinetic state model and to determine the state trajectory for each individual molecule. These can then be further analyzed to gain deeper insights of the system under study (Section 3.6).

Finally, different ways of determining the uncertainty of the values extracted from the data are presented in Section 3.7.

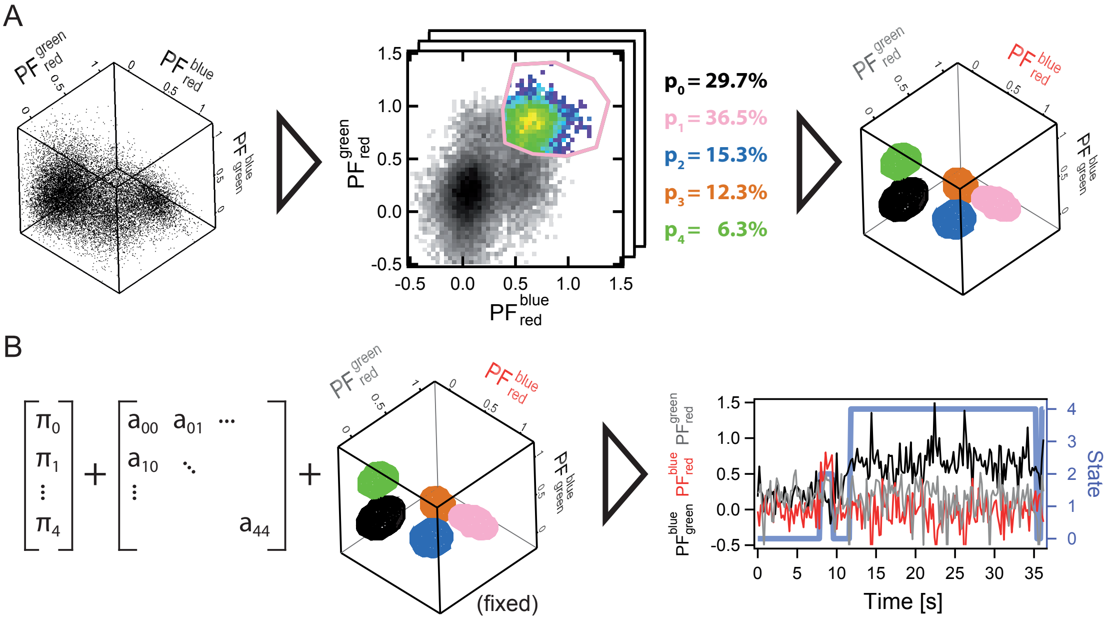

Figure 3.4: Workflow for state assignment and extraction of kinetic information in a three-color smFRET experiment. (A) Determination of the state-specific 3D Gaussian emission PDFs in the PF space (left). Population weights are obtained from free-hand polygons in 2D projections (middle). The weights serve as constraints in the subsequent fit with the sum of five Gaussians to the 3D PF histogram (right). (B) HMM optimization and extraction of kinetic information. One ensemble HMM is trained on the complete data set (left). The emission PDFs are fixed to the ones obtained from the procedure shown in (A). From the optimized kinetic state model, the Viterbi path (blue) can be calculated for each molecule (right). Figure based on Ref. [35].

3.4. Identifying 3D Gaussian PDFs for Multiple States

How to obtain good estimates for the state-wise 3D emission PDFs? This is achieved by fitting the sum of five Gaussian functions to the 3D histogram of the PFs. The means and covariance matrices of the fit are then used in the subsequent HMM optimization.

The PF distributions of each state can be approximated with Gaussian functions (refer to Subsection 3.4.1). However, a fit without any constraints results in vanishing of Gaussians (since the population weighing factors get very small) or very broad Gaussians, spreading over more than one visually distinguishable state (Fig. 3.5).

To prevent unreasonable fitting results, constraints have to be applied. Ideally, the constraints do not affect the position or width of the Gaussian functions directly since these are the variables that are supposed to be obtained. For the data sets used in this work it is already sufficient to keep the population weights fixed during the fit. These can be determined independent of the fit by mere “counting” the events that comprise one state in the PF histogram.

To do so, it is necessary to combine the information from at least two 2D projections of the 3D PF histogram since there are overlapping states in any projection. E.g. Figure 3.5A shows that states S_0 and S_4 are overlapping in the PF_{red}^{green} over PF_{red}^{blue} projection while state S_4 can be discerned from all the other states in the PF_{green}^{blue} over PF_{red}^{blue} projection.

Events in one state are counted by manually drawing a polygon around the corresponding area in the PF plot (Fig. 3.6). The number of events selected by such a “localization” is then divided by the total number of events selected, in order to normalize the sum of the relative populations to unity. In total, polygons are typically drawn nine times for each state and the results are averaged to reduce the influence of the exact shape and position of the hand-drawn polygon.

The fit’s starting values for the position and width of the Gaussians are estimated from the 2D projections of the 3D PF histogram “by eye”. Also, fit results from other experimental conditions can be used. The better the initial guess, the fewer iterations are necessary for the fit to converge. Fitting five Gaussian functions in 3D is a computationally expensive task and is performed on a work-station with 20 CPUs for maximal parallelization.

Even though the manual localization may seem coarse, the reproducibility in determining the population size is sufficiently high. Figure 3.7A shows that the maximal relative error is below 10% for all states and around 5% for states that are substantially populated. Thus, the variability in the data set (as judged from ten 75% subsets) is larger than the uncertainty from the localization process. Also, the influence of the person that analyzes the data is small (Fig. 3.7B).

In summary, the approach to determine the population weights from free-hand polygons and to use them as constraint for the three-dimensional fit works reasonably well and constitutes only a small perturbation of the Gaussian fit considering the number of free fit parameters.

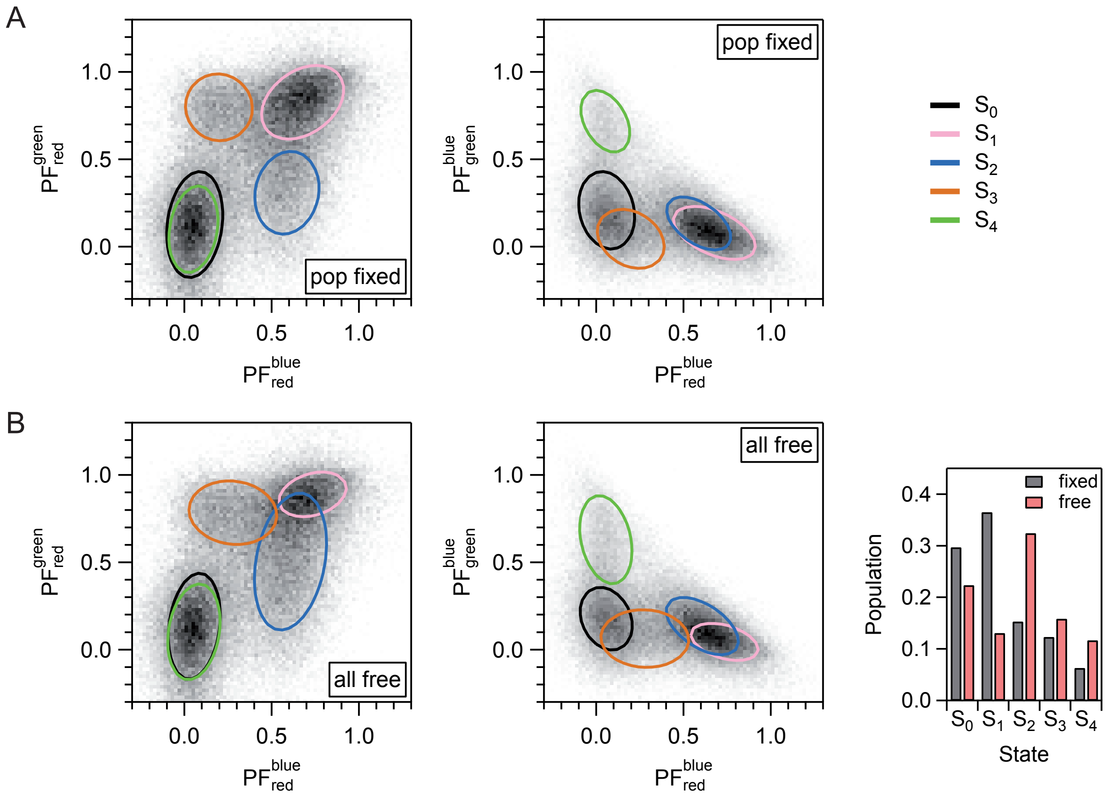

Figure 3.5: Constraining the population weight in the 3D fit is sufficient to yield reasonable results. (A) Fit result in two 2D projections with the population weights constraint. The color code of the states is given to the right. (B) Same as (A) with the population weights not constraint. The panel to the right gives the populations for both the constraint and the free fit, showing drastic differences. The PDFs of the states are depicted as contour of the full width at half maximum.

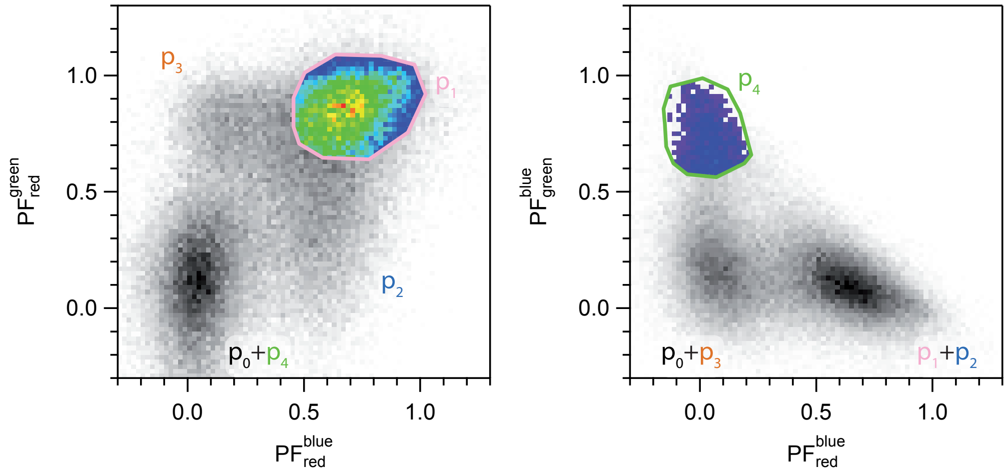

Figure 3.6: Manual localization of the five states and determination of their relative populations. Events that comprise a states are selected by manually drawing a polygon. By combining two projections the relative populations of all five states can be determined.

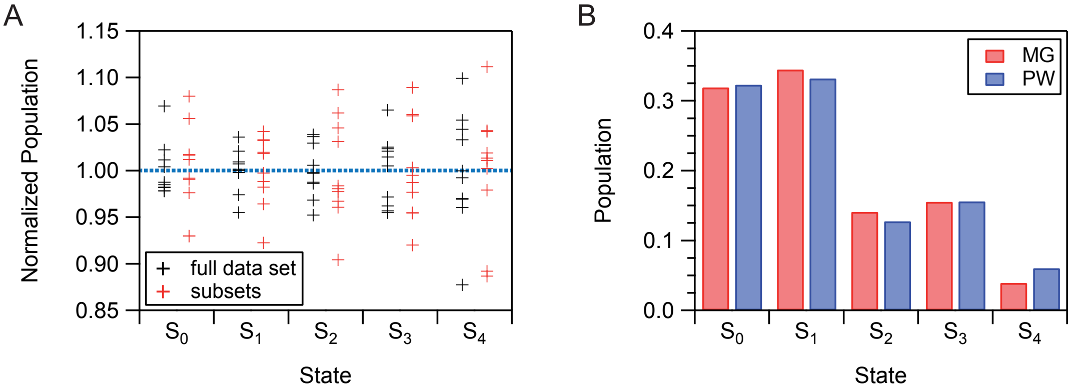

Figure 3.7: Reproducibility of the manual population localization process. (A) Population sizes were determined for a typical data set (ten repetitions) or ten random 75% subsets thereof. Population sizes where normalized to the mean of all ten repetitions of the full data set. Each marker is the average of three localizations. The relative error is typically below 5% for the manual localization process. (B) Comparison of the subjective bias introduced by the person (indicated by initials MG or PW) that selects the states.

3.4.1. Shape of the Fluorescence Intensity and PF Histograms

Different conformational states of Hsp90 interacting with Atto647N-labeled AMP-PNP (AMP-PNP*) result in distinct populations in the 3D histogram of the PFs. In two-color TIRF experiments, the one-dimensional FRET efficiency histogram can be fitted sufficiently accurate by the sum of one-dimensional Gaussian functions. When the two fluorescence intensities of the donor and acceptor dye are considered instead, assuming Gaussian distributions is also appropriate [115].

In order to check if this assumption still holds also in the three-color experiments the intensity and PF histograms are compiled for each state independently in Figure 3.8. In general, the fluorescence intensity distributions are roughly Gaussian with a slight tail towards higher intensities (see Fig. 3.8A and 3.8B). The PF_{green}^{blue} and PF_{red}^{blue} distributions are nicely described by Gaussian functions for all states. The PF_{red}^{green} distribution is slightly skewed to the left (i.e. with a longer tail to smaller PF) for all states (see Fig. 3.8C). The PF distributions are narrower compared to the intensities. This is in line with the 2D histogram in Figure 3.3.

The exact shape of the histograms could be derived from a detailed theoretical description of the underlying photon statistics [32, 33, 10] and a model accounting for experimental shortcomings (e.g. non-uniform excitation intensities). However, one finds that empirically, the distributions are well approximated by Gaussian functions. Such a simple function also brings the benefit of increased computational speed for further calculations, especially in the optimization of an HMM.

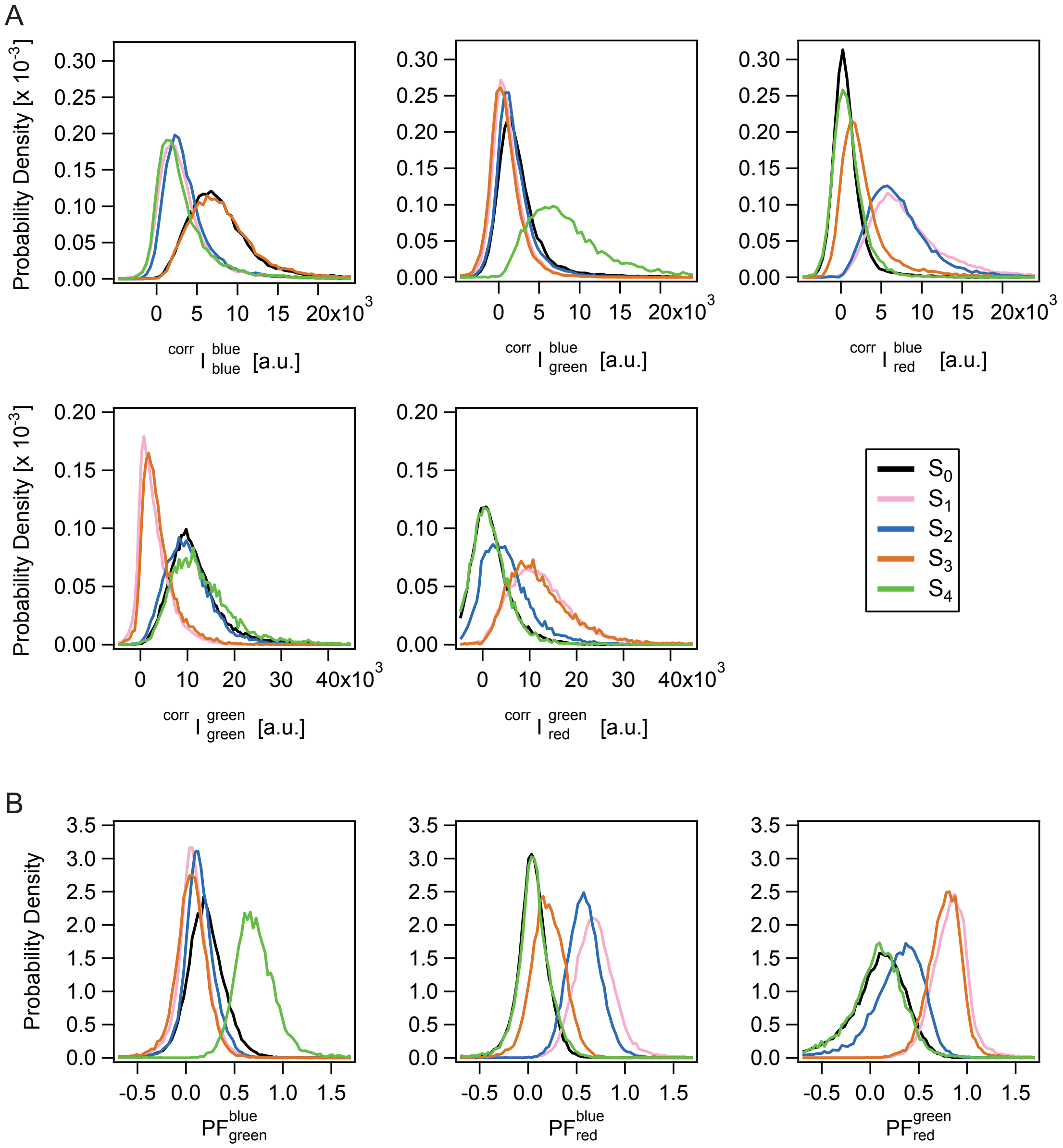

Figure 3.8: Probability density functions of fluorescence intensity and PF for all five states of a representative three-color smFRET experiment. (A) Probability density function of the fluorescence intensity, separated according to excitation and emission channel. Intensities were corrected for leakage and different gamma factors. (B) Same data as in (A), shown for the PF. Both intensities and especially the PFs can be reasonably well described with Gaussian functions.

3.5. HMM Parameter Optimization for 3D PF Data

The implementation of the HMM algorithms in IgorPro code followed Ref. [25]. In order to prevent an arithmetic underflow or overflow, scaling coefficients that keep the probability values in the dynamic range of the Igor interpreter are used in the forward-backward and the Viterbi algorithm. This approach has to handle multiples of the scaling factor (10^{50}) per time step because probabilities well below this limit occur with a three-dimensional PDF.

After having established a method for the determination of parameters for the emission PDFs in the previous section, an HMM is used to extract the kinetic information and the state trajectories from the data. All three components of the HMM (initial and transition probabilities, emission PDFs) are used in a “global” manner, meaning that they are not determined per molecule but are shared by the whole ensemble of molecules in the data set.

Individual (i.e. per molecule) emission probabilities are not used for two reasons: First, due to the width of the PDFs in the PF space, the overlap between different states is not negligible. Only by averaging over all molecules, states that can be reliably distinguished emerge. Thus, it may be difficult to assign states reasonably from just one molecule. Second, when five states are distinguishable according to their PFs, the likelihood that one molecule visits all states during the observation window for a sufficient amount of time gets small. Thus, individual emission PDFs would not be possible for the most molecules or the “partial” PDFs would have to be linked via the global PDF anyway.

Start values for the initial probabilities are set to the relative population of each state. The transition matrix for a five-state model is initialized with $a_{ii} = 0.8$ for each state and the remaining probability split equally for all other transitions.

The parameter optimization using forward-backward and Baum-Welch algorithms does not result in the convergence to reasonable emission PDFs for all of the five states (Fig. 3.9). Thus, the emission PDFs that where determined from the 3D Gaussian fit are kept fixed during the optimization of the other HMM parameters. After the starting and transition probabilities are optimized, the Viterbi path, i.e. the most likely state trajectory, is calculated for every molecule.

In order to prevent the HMM (and in turn also the Viterbi algorithm) to erroneously assign a transitions at a time point t where one of the PF traces contains an outlier (i.e. the PF exceeds the interval $[-1; 2]$), the emission O_t is set to “Not a Number” (NaN). At these time points, our implementation of the forward-backward algorithm uses the minimal emission probability (10^{-200}) for all states. This prevents a numerical underflow in the calculation of the probabilities and artificial transitions because in this case remaining in the previous state is the most likely process according to the transition probabilities (assuming $a_{ii} > a_{ij}\ \forall\, i,\ j,\ i \neq j$). Molecules with an overall poor trace quality (i.e. with more than 10% of the frames being set to NaN) are removed from the data set.

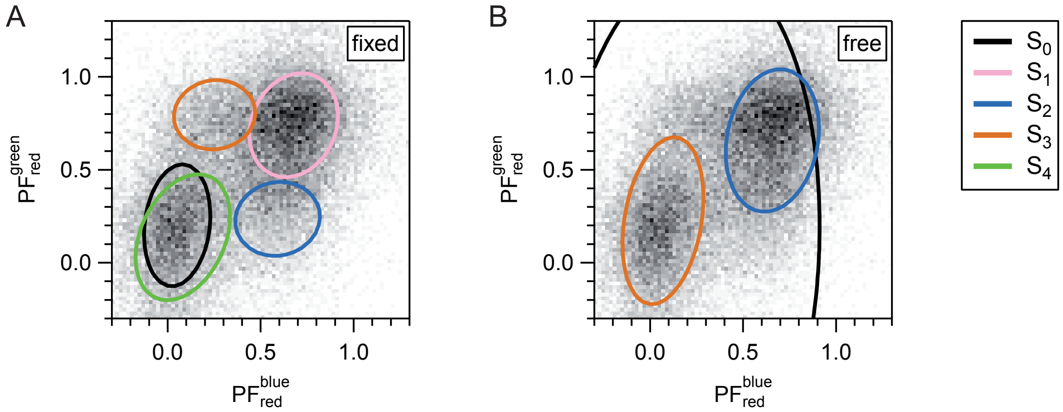

Figure 3.9: Convergence of the emission probabilities of the HMM. (A) Emission PDFs are constrained to the values obtained from the 3D Gaussian fit and (B) allowed to be optimized (“free”) with the same starting values as in (A). When the emission PDFs are optimized by the Baum-Welch algorithm, position and width are not stable and the population of two states even drops to zero. The PDFs of the states are shown as contour of the full width at half maximum.

3.6. Evaluation of Viterbi Paths and Transition Matrix

In a Markov chain, the transition probabilities are time-invariant, that is, constant over time. If the Markov chain is ergodic, i.e. any state can be reached from any other state in a finite number of steps, a unique, stable “stationary distribution” exists [38]. All information about the kinetics and the stationary distribution (i.e. the steady state population) of the states is given by the transition matrix:

- The column vector describing the stationary state population ($\boldsymbol{\pi}$) has entries that are non-negative and sum to unity. It is unchanged by the operation of the transition matrix $\boldsymbol{A}$ and thus satisfies the following equation:

  $$\boldsymbol{\pi}^\mathsf{T}\boldsymbol{A} = \boldsymbol{\pi}^\mathsf{T} \tag{3.5}$$

  This means that the state population is the left eigenvector of the transition matrix with eigenvalue 1.

- The relative occurrence of a certain transition, say from state i to state j, is given by $f(s_{t+1} = j|s_t = i) = \pi_i \cdot a_{ij}$. The number of transitions is illustrative when it comes to finding the transitions that are taken frequently in the protein’s path through the network of states.

However, the transition matrix may not be very intuitive when it comes to understanding the overall effects that are caused by changes in one or more rates in a complex kinetic model. To this aim, dwell time histograms of the relevant process (which may comprise more than one specific transition from a state to another) can be compiled.

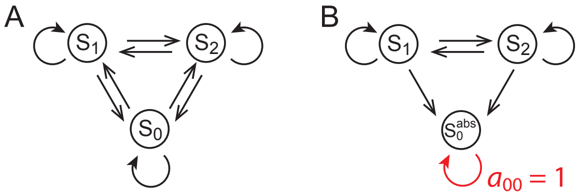

Figure 3.10: Converting a Markov chain in an absorbing Markov chain. (A) Exemplary three-state Markov chain. (B) Corresponding absorbing Markov chain with state S_0^{abs} as the absorbing state. Transition probabilities leaving S_0^{abs} are set to zero and the transition probability to stay in state S_0^{abs} (i.e. a_{00}) is set to 1.

To further reduce the complexity and increase the comparability between different experimental conditions, the mean dwell time for a process can be determined.

In case of a first order elementary process with a rate constant k, the mean dwell time is equal to the time constant of the reaction $\tau = 1/k$. If the process under consideration is more complex and comprises more than one steps in the state network, the mean dwell time may not have a strict physical equivalent anymore. It is nevertheless useful to give an impression of the time scale of the process.

Different approaches for compiling the dwell time histogram are possible. Either, only dwells with an observed start and end point can be taken into account, i.e. the dwell is “bounded”. If this requirement is dropped, the dwells are called “unbounded” in this work. Using dwell times as the basis for kinetic conclusions might be problematic because an observation bias leads to a systematic overestimation of the rate. This is due to missing long events that occur on a time scale similar to or larger than the average trace length. Including unbounded dwells in the dwell time histogram mitigates this systematic error to a certain degree because the histogram is based on more data and longer dwells also appear in the histogram, even if their endpoint was not observed. However, the result still is only an estimate for the lower limit of the dwell time.

Another approach independent of the actual dwells in the Viterbi path is to directly calculate the expected average time it takes to get from one state to another. The presented method only relies on the optimized HMM, which in turn is based on the data that contains the observation bias. However, applying this observation bias twice (for optimization of the HMM *and* for analysis of the dwells) is circumvented. This can be done by modifying the state model such that it corresponds to an “absorbing Markov chain” [38]. An absorbing state S_i^{abs} is impossible to leave (i.e. $a_{ii} = 1$). An absorbing Markov chain has at least one absorbing state, which can be reached from every state (in a finite number of steps).

Thus, if one is interested in the average time it takes to reach certain states (starting in an arbitrary state) these end states are considered the absorbing states and the corresponding transitions probabilities leaving these states are set to zero. For example, to get the average time it takes to reach S_0 from either S_1 or S_2 for the three-state system shown in Figure 3.10A, the Markov chain is modified as indicated in Figure 3.10B.

Let there be an absorbing Markov chain with a total of S states and r absorbing states. Setting the transition probabilities leaving absorbing states to zero and reordering the transition matrix $\boldsymbol{A}$ so that absorbing states come last gives the matrix $\boldsymbol{A}'$

$$\boldsymbol{A}' = \begin{pmatrix} \boldsymbol{Q} & \boldsymbol{R} \\ \boldsymbol{0} & \boldsymbol{I}_r \end{pmatrix} \tag{3.6}$$

where $\boldsymbol{Q}$ is a $(S-r)\times(S-r)$ matrix, $\boldsymbol{R}$ is a nonzero $(S-r)\times r$ matrix, $\boldsymbol{0}$ is a $r\times(S-r)$ zero matrix, and $\boldsymbol{I}_r$ is the $r \times r$ identity matrix (with ones on the main diagonal and zeros elsewhere). For the example given in Figure 3.10, this results in a matrix $\boldsymbol{A}'$

$$\boldsymbol{A}' = \begin{array}{c} \\ \mathrm{S}_1 \\ \mathrm{S}_2 \\ \mathrm{S}_0^{\mathrm{abs}} \end{array} \begin{array}{c} \begin{array}{ccc} \mathrm{S}_1 & \mathrm{S}_2 & \mathrm{S}_0^{\mathrm{abs}} \end{array} \\ \begin{pmatrix} a_{11} & a_{12} & a_{10} \\ a_{21} & a_{22} & a_{20} \\ 0 & 0 & 1 \end{pmatrix} \end{array}, \quad \text{with } \boldsymbol{Q} = \begin{pmatrix} a_{11} & a_{12} \\ a_{21} & a_{22} \end{pmatrix} \tag{3.7}$$

The probability of being in a non-absorbing state s_j after k steps, if the chain started in state s_i is given by $\boldsymbol{Q}^k$. Then, summing over all possible numbers of steps yields the matrix $\boldsymbol{N}$, whose entries n_{ij} give the expected number of times that the process is in state s_j, if it started in state s_i.

$$\boldsymbol{N} = \sum_{k=0}^{\infty} \boldsymbol{Q}^k \tag{3.8}$$

This is a Neumann series (analogous to a geometric series in $\mathbb{R}$) and can be re-written as

$$\boldsymbol{N} = \sum_{k=0}^{\infty} \boldsymbol{Q}^k = (\boldsymbol{I}_{S-r} - \boldsymbol{Q})^{-1} \tag{3.9}$$

where $\boldsymbol{I}_{S-r}$ is the identity matrix of the same dimension as $\boldsymbol{Q}$. The expected number of steps before an absorbing state is reached, when starting in state i, is the i-th entry of the column vector

$$\boldsymbol{t} = \boldsymbol{N}\boldsymbol{1} \tag{3.10}$$

where $\boldsymbol{1}$ is a column vector of length $(S-r)$ whose entries are all 1. The expected number of steps averaged over all possible starting states, i.e. the time to adsorption (in number of frames), is then given by the dot product of the normalized population of the starting states with $\boldsymbol{t}$.

$$\tau_{TTA} = \frac{1}{\|\boldsymbol{\pi}'\|}\,\boldsymbol{\pi}' \cdot \boldsymbol{t} \tag{3.11}$$

with $\boldsymbol{\pi}' = \begin{pmatrix} \pi_1 \\ \pi_2 \end{pmatrix}$ for the example given in Fig. 3.10. An exemplary calculation of the time to absorption for experimental data (nucleotide dissociation from Hsp90) is given in the Appendix, Section A.2.

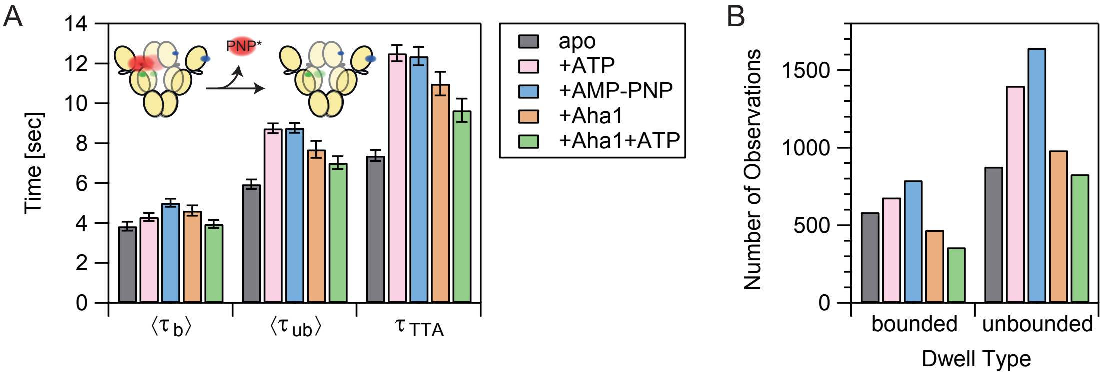

Figure 3.11: Different ways for representation of kinetic information. (A) Different ways of illustrating the time, a labeled nucleotide stays bound to Hsp90. From the Viterbi path dwells in the respective state can be extracted. If observation of both start and end of the dwell is required ("bounded" dwell, $\langle\tau_b\rangle$) a lot of dwells are ignored compared to the case without this limitation ("unbounded", $\langle\tau_{ub}\rangle$) . From the HMM the "time to absorption" (τ_{TTA}) can be calculated which is less biased by limited observation time. Error bars indicate the standard deviation from ten random 75% subsets. (B) Number of dwells found for the transition in (A). Up to about 50% of the dwells may be ignored when bounded dwells are used.

3.7. Estimates of Uncertainty

Different sources contribute to the overall uncertainty of the measures extracted from the data: (i) Variations in experimental conditions that are not controlled – or are not controllable with reasonable experimental effort – result in deviations between single experiments. (ii) Experimental limitations such as photobleaching lead to a limited observation window and in turn to a limit of the temporal resolution. (iii) Various noise sources (blinking of the fluorophores, dynamics of the sample faster than the time resolution, etc.) result in a decrease in the SNR. (iv) Data analysis introduces another layer of uncertainty by selecting and filtering the data. (v) Only a limited number of observations can be accumulated in finite time, limiting the statistics of the results.

To indicate the degree of precision that is achieved for a result obtained from the data analysis, it is necessary to give meaningful uncertainty bounds. Several procedures are used and compared here since they report on different aspects contributing to the uncertainty.

3.7.1. Population Size

For determining the population of the five states, reproducibility of the manual localization and the variability in the data set are expected to be the main sources of uncertainty. The influence of the manual localization process can be reduced by averaging over a sufficient number of repetitions. Slight outliers are already marginalized by averaging over three localizations (see Fig. A.2 in the Appendix) and typically nine localizations were averaged to determine the population of a state in this work. The overall precision of the approach leads to a relative uncertainty of about ±5% for states with a relative population larger than 5% and about ±10% for states with a relative population smaller than 5%. The same is true for the accuracy of the population. Figure 3.12 shows that the true population size is recovered from simulated data with a deviation below 5 percent points.

What is more, the variability in the data set can be assessed with subsets of the original data. With decreasing subset size the variation of the localizations increases slightly (see Fig. 3.13). However, with decreasing subset size also an increase in the mis-assignment between states S_1 and S_2/S_3 can occur. Thus, subsets of 75% are good compromise and report on both, the variability within the data set and on the uncertainty of the manual localization procedure.

3.7.2. Transition Probabilities

Uncertainties for the MLEs of the transition probabilities (and thus for the rates) are taken from their confidence intervals (CIs). These CIs report on both, the variability in the data set and the goodness of fit of the HMM for the specific rate.

The SMACKS implementation calculates a likelihood profile of the parameter of interest by varying the transition probability in a fixed interval around the MLE and keeping all other rates equal to their MLE (see Fig. 3.14A). To ensure that the total probability of leaving a state always sums to one, the probability to stay in the respective state is adjusted accordingly. With this new set of rates, the production probability and the likelihood ratio (LR) are calculated (see Section 2.5.4). The sampling points are equally distributed in log space to account for the asymmetric shape of the likelihood profile. The endpoint of the CI is found by linear interpolation between the two sampling points closest to the LR corresponding to the desired significant level.

This approach can be further improved by stepwise approximating the endpoint of the CI with the secant method [137]. From two estimates for the limit of the CI a new estimate is calculated by linear extrapolation. Since this method omits calculating the likelihood profile in regions far away from the limit of the CI, the endpoint can be sampled with higher resolution.

However, this approach neglects the fact that all the other rates would slightly change with one rate forced away from its MLE if the HMM is re-optimized. The small changes in the other rates partially compensate for the variation of the rate under consideration. As a consequence, the CI is slightly larger if the HMM is re-optimized. This improvement comes at the cost of significant higher computational effort since for each sampling of the likelihood profile the HMM has to be re-optimized.

As expected, stepwise approximating the endpoint of the CI with the secant method gives a slightly larger CI (as would be the case if the likelihood profile would be sampled with higher resolution). Stepwise approximation in combination with re-optimization of the HMM increases the CI to an even larger extend. However, as can be seen in Figure 3.14B, all three approaches do not differ drastically in the estimated CI. Consequently, the HMM re-optimization was omitted for calculating the uncertainty of the transition probabilities. This speeds up the calculation while still yielding CIs that are

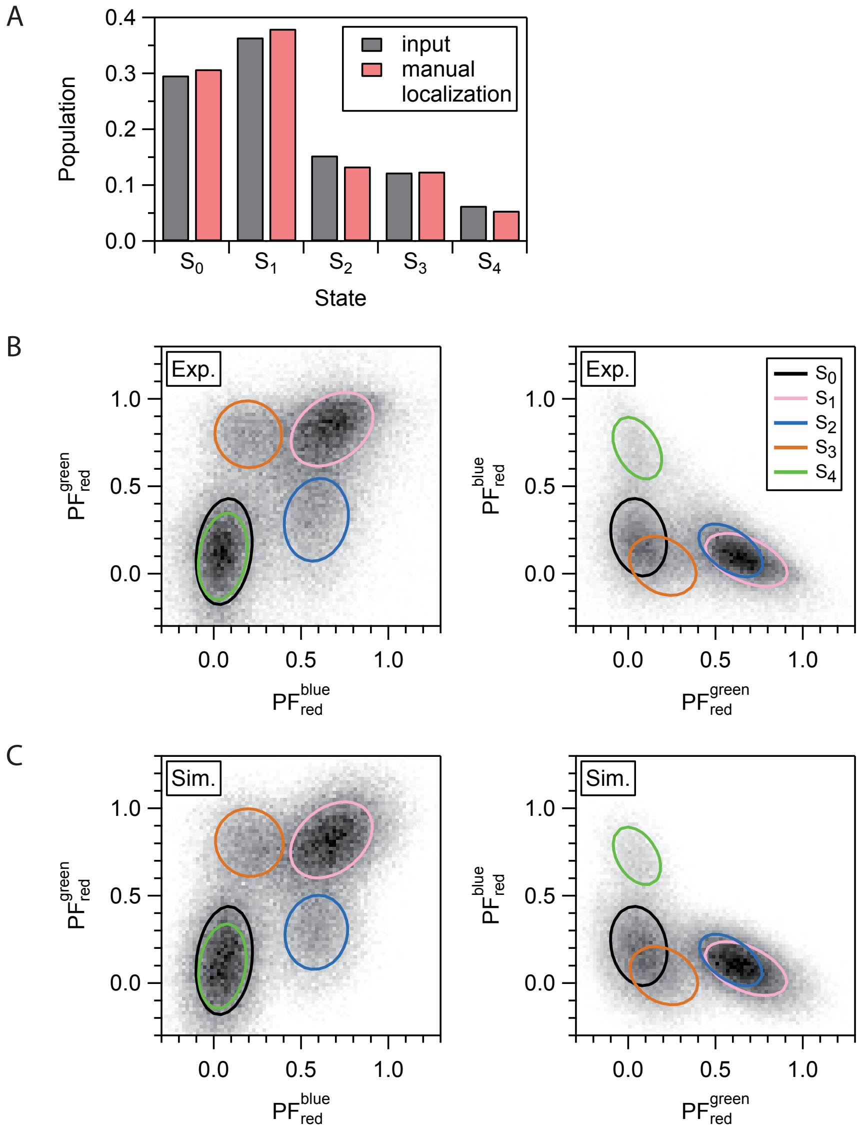

Figure 3.12: Accuracy of population selection and 3D Gaussian fitting procedure. (A) Accuracy of the manual population localization. A 3D PF histogram was simulated with the indicated population distribution (black) and subjected to manual selection (red). (B) Experimental data and respective positions of the states that served as the simulation input. (C) Simulated PF histogram and respective state positions found after manual localization and fitting. Position and width are recovered with high accuracy.

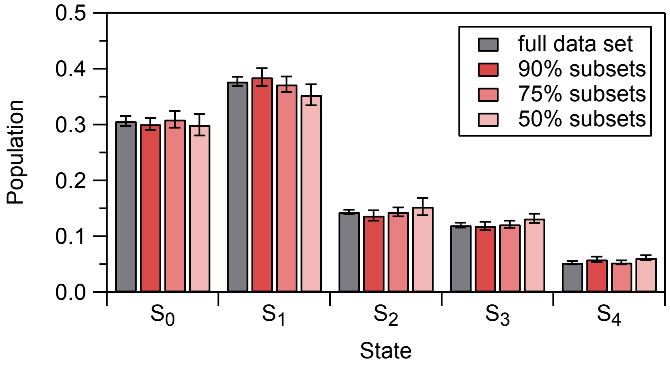

Figure 3.13: Dependence of population size from subset size. For 50% subsets, populations start to get less well defined as is evident from a shift of the population of S_1 to S_2/S_3. A slight trend of increasing uncertainty with smaller subset size is observed, however, the influence of the subset size is not very strong. Thus, the uncertainty mostly arises from the manual localization process. Three localizations where averaged and mean and standard deviation from ten such values are depicted.

closer to the exact solution than using equally spaced sampling points.

3.7.3. Single Data Sets

For each tested experimental condition, three data sets were recorded. A possibility to asses the variability between the three data sets recorded under the same experimental conditions is to analyze them separately and to compare with the results obtained from the merged data set. Population sizes were determined for each data set and the HMM was optimized with the emission parameters set to the ones determined for the merged experiment.

As can be seen in Figure 3.15, the weight averages agree well with the values obtained from the merged data set. As expected, the standard deviation of the three single data sets is larger as the uncertainties obtained from the merged data set. First, the merged data set comprises more data points and consequently the extracted values can be determined with higher confidence. Second, this indicates that the experiments are not exact replicates of the same experimental conditions.

Nevertheless, effects observed in the merged data set are also present in each individual data set.

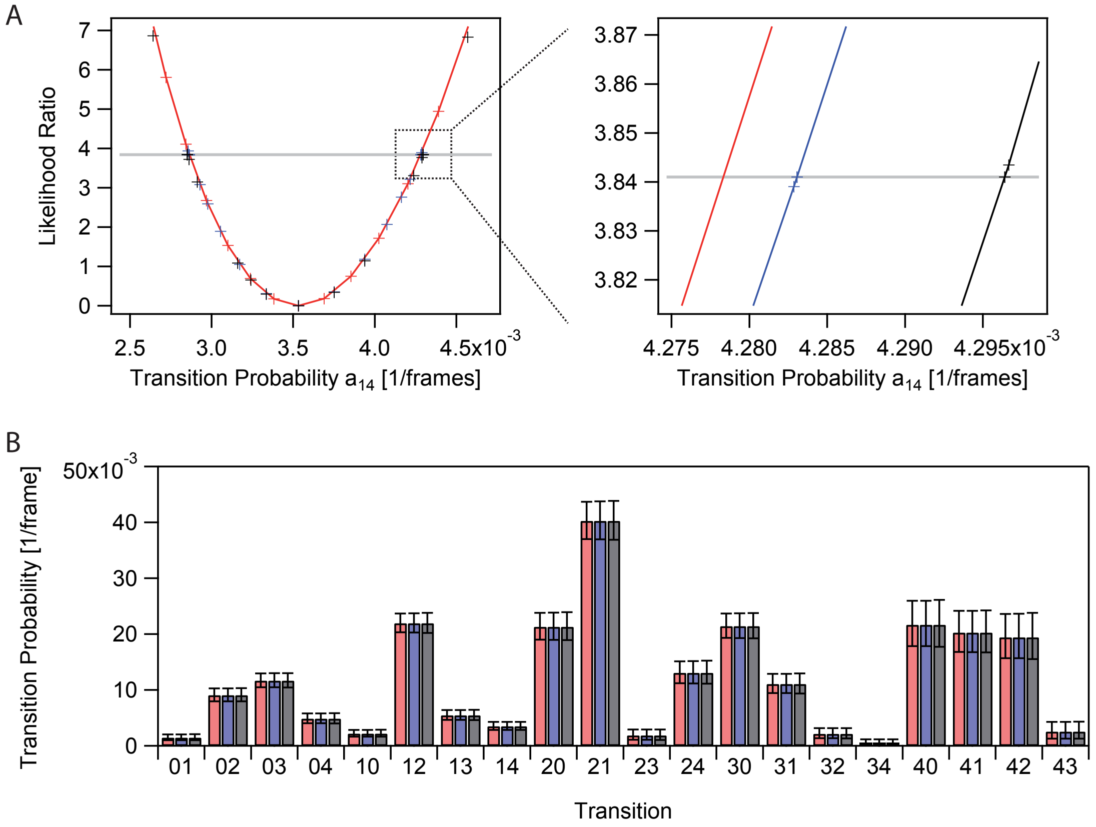

Figure 3.14: Different approaches to determine the confidence intervals for transition probabilities. (A) Likelihood profile using the approach followed in SMACKS [115] (red, lines connecting markers are a linear interpolation), stepwise approximation of the endpoint using the secant method (blue) and stepwise approximation in combination with HMM re-optimization (black). The gray line indicates the LR that corresponds to a significance level of 5% (i.e. results in the 95% CIs). The panel on the right shows a zoom in for the upper boundary of the CI. The crossing of the significance level defines the endpoint of the CI. The different approaches result in a CI of $\pm 0.707 \times 10^{-3}$, $\pm 0.710 \times 10^{-3}$ and $\pm 0.723 \times 10^{-3}$, respectively. (B) The 95% CI for all transitions. The different approaches yield almost identical results for all transition probabilities.

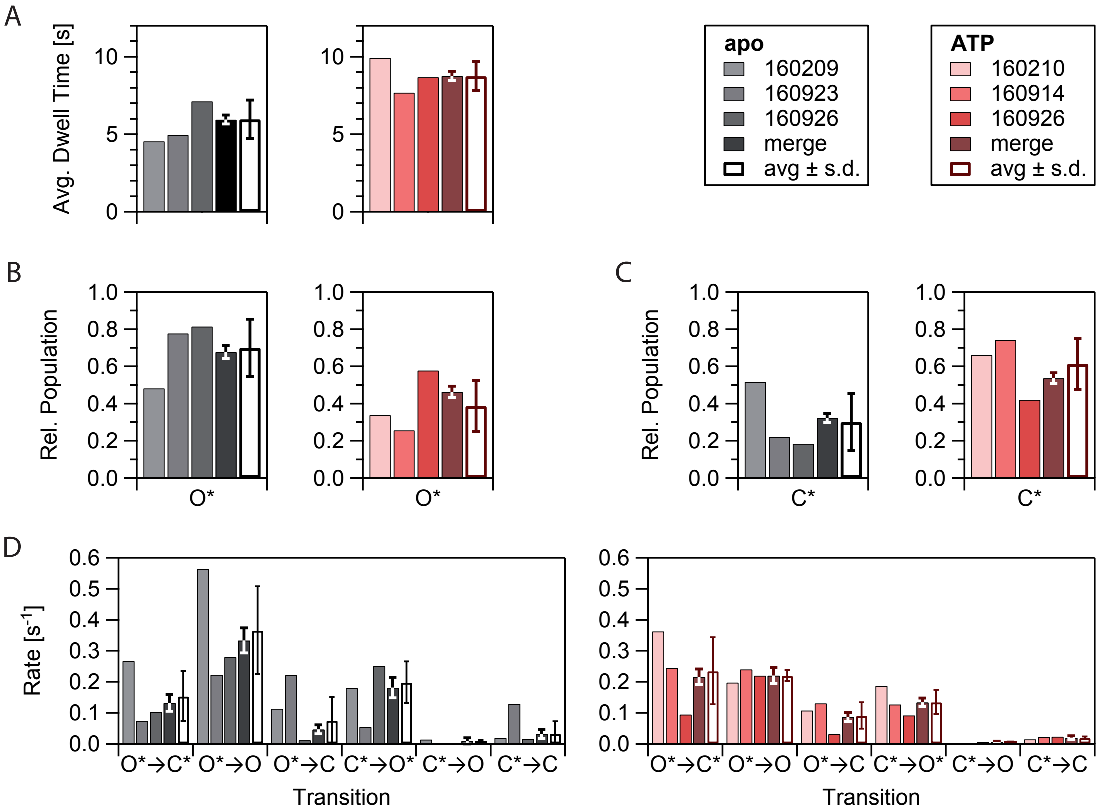

Figure 3.15: Comparison of results from the single data sets. Shown are single experiments (gray or light red), the merged experiment (black or dark red) and the average and standard deviation (s.d.) of the three single experiments (empty bars). For averaging, experiments are weight according to the number of frames in each single data set. The identifiers represent the functional states of the system (O $\equiv$ S_0, C $\equiv$ S_4, O* $\equiv$ S_2/S_3 and C* $\equiv$ S_1). (A) Average dwell time of Atto647N-labeled AMP-PNP (AMP-PNP*) bound to Hsp90. Error bars of the merged experiment are the estimated s.d. from a jackknife resampling. (B) Relative population of the open AMP-PNP* bound state, O*. Error bars of the merged experiment represent one s.d. from ten 75% subsets. (C) Relative population of the closed AMP-PNP* bound state, C*. Error bars as in (C). (D) Transition rates. Error bars of the merged experiment represent the 99% confidence interval. Figure based on Ref. [144].

3.8. Outlook

In order to make multi-color smFRET measurements a robust, easy-to-use technique, different improvements both in experiment and analysis are conceivable. From the data analysis point of view, it would be advantageous to be able to use the fluorescence intensity instead of the PF because it is less susceptible to uncorrelated noise and increases the robustness (much like as in the case of SMACKS).

For this, a more homogenous excitation is needed. Expanding the excitation beams more and cutting out only the central part could help to achieve this. Also, using a correction for the excitation intensity similar to the one applied in a two-color experiment could improve the situation. A so-called "intensity map" can be recorded after the actual measurement with a more densely covered sample chamber. The chamber is moved during acquisition and the average of the image stack is used to correct for the position-specific excitation profile.

Another possibility that makes use of the fluorescence intensity traces is to normalize them to the time-average of the total intensity after the respective excitation, i.e. $\langle I^a \rangle = \frac{1}{T}\sum_{t=1}^{T}\left(\sum_{i=a}^{c} I_i^a(t)\right)$. This normalization yields a value similar to the PF, however the additional averaging over time results in significantly less extreme outliers (see Fig. 3.16).

Furthermore, other approaches to determine the relative populations from the PF histogram can be conceived. These include the application of clustering algorithms. However, a preliminary test with k-means clustering did not result in a satisfactory assignment of the states.

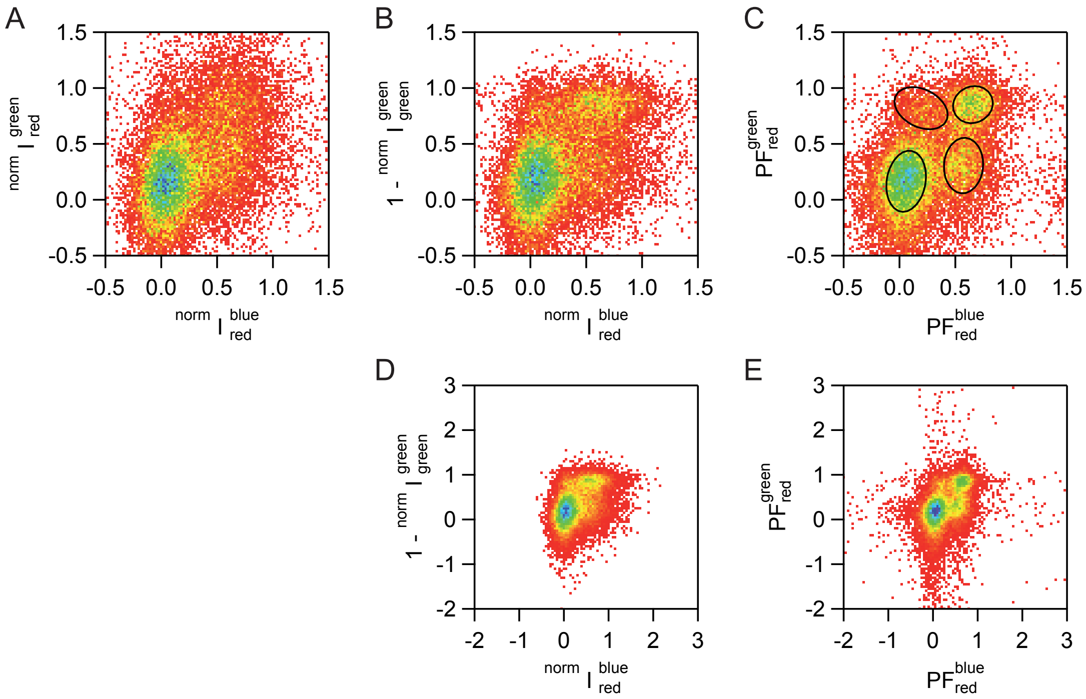

Figure 3.16: Using the fluorescence intensity instead of the PF in multi-color smFRET experiments. Different visualizations of the same data set: (A) Normalizing the fluorescence intensity I^{green}_{red} with the time-averaged total intensity after green excitation still results in broad distributions for ${}^{norm}I^{green}_{red}$ because the background fluorescence from AMP-PNP* is very high in the I^{green}_{red} channel. (B) Instead, using $1 - {}^{norm}I^{green}_{green}$, which reports on the same process, allows to distinguish again the four clusters that can also be seen in the PF plot (C). (D, E) Zoom-out of (B, C). Using an intensity based measure results in significantly less extreme outliers.

4. Application of smFRET to Biological Systems

For living organisms, the dynamic nature and flexibility of many of its key building blocks is essential. For example, interaction partners have to temporarily bind to each other to transmit signals in the cell and proteins have to adopt different conformations to fulfill their function. This part of the work features different approaches how to determine the influence of single parts in a multi-component systems, namely the Hsp90 system with co-chaperones and substrates.

4.1. The Hsp90 Co-Chaperones p23 and Aha1

Hsp90 is know to interact with a network of at least 20 co-chaperones that guide its recognition of client proteins and modulate its biochemical activity [134]. Of these, the two co-chaperones p23 and Aha1 are of special interest. They are prominent examples of non-TPR proteins, bind to Hsp90 with a relative high affinity and significantly influence its ATPase activity.

p23 (Sba1 in yeast), named after its approximate molecular weight, is conserved from yeast to man [57, 111]. The protein binds to the junction of the two N-domains of Hsp90, thereby interacting with both monomers [5, 61] (see also Fig. 4.1). An additional interaction site is found in the M-domain of Hsp90 [78, 110]. A stoichiometry of 1:1 or 2:1 (p23 per Hsp90 dimer) have been suggested [131, 114, 125, 61].

The N-terminal part of p23 is stably folded while the C-terminal tail (roughly the last 80 residues in Sba1) is flexible and unstructured [141], which has prevented crystallization of this part for the human or yeast protein [140, 5].

p23 decreases the ATPase activity of Hsp90 to about 50% [95, 114] and is supposed to specifically target the closed state of Hsp90 [131, 45]. Under AMP-PNP conditions, the apparent dissociation constant for p23 and Hsp90 is found to be 0.5 µM while it is about 15 µM for Hsp90 with ATP (where no significant population of the closed state occurs) [114].

The Activator of the Hsp90 ATPase (Aha1) was first described in 2002 and – like in the case of p23 – its homologues are conserved within the eukaryotes [95]. Aha1 interacts in an anti-parallel fashion with Hsp90 as the N-terminal domain of Aha1 interacts with the middle domain of Hsp90, while the C-terminal domain of Aha1 contacts the N-domains of Hsp90 [84, 112, 68]. Again, the stoichiometry remains elusive, with reports of one or two Aha1 per Hsp90 dimer [95, 125, 112, 73].

No structure of the full-length Aha1 is available to date. However, its N-terminal domain (residues 1–153) was crystallized [84] and a NMR structure of the C-terminal domain exists [112]. Binding of Aha1 is reported to require [114] but also to favor

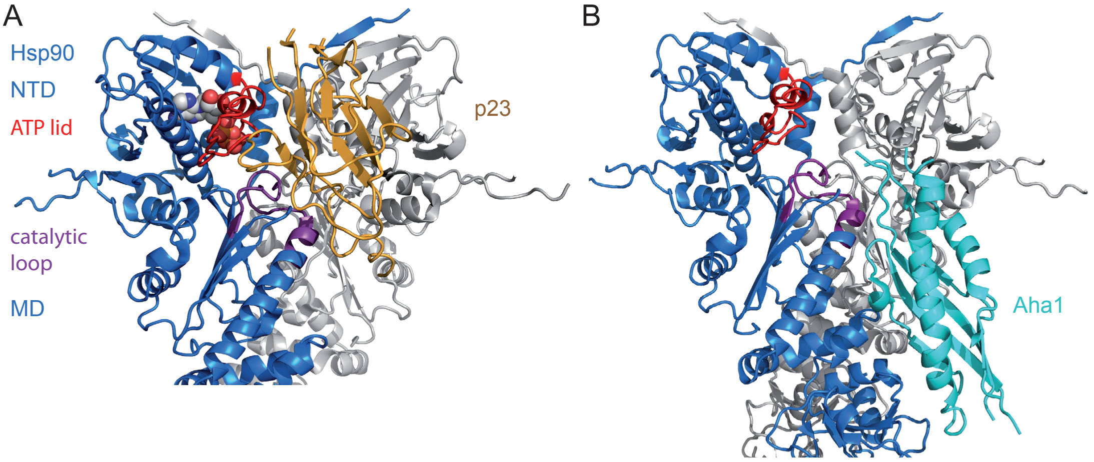

Figure 4.1: Interaction sites of p23 and Aha1 on the Hsp90 dimer. The N-terminal (NTD) and middle domain (MD) of the Hsp90 homodimer (blue and grey) are depicted. (A) The NTD of p23 (orange). The second p23 molecule that is part of the crystal structure is omitted for clarity. The bound nucleotide in one subunit is shown as space-filling spheres (CPK coloring), the second is omitted. The ATP lid (residues 94–125) is highlighted in red and the catalytic loop (residues 370–390) in purple. PDB 2CG9 [5]. (B) The NTD of Aha1 (cyan). PDB 1USU [84].

the N-terminal dimerization of Hsp90 [45, 112]. Furthermore, the more than tenfold acceleration of the ATPase rate in the presence of Aha1 [95] is thought to be caused by a change of the conformation of the catalytic loop in the M-domain of Hsp90 [84, 49]. This loop harbors residue Arg380, which contacts the γ-phosphate of ATP bound to the N-terminal nucleotide binding pocket. This interaction is thought to polarize the terminal phosphodiester bond of ATP, thereby contributing to hydrolysis [5, 19].

4.1.1. Effects of p23 on Hsp90

In order to test the effect of p23 on the large-scale dynamics of Hsp90, smFRET experiments with a heterodimer of Hsp90 (D61C-Atto550/Q385C-Atto647N-biotin) and in the presence of 2 mM ATP were performed. Molecules from three experiments under apo or ATP conditions where combined to yield statistically significant results and analyzed with SMACKS [115]. Overall, a similar kinetic model is obtained, independent of the presence of p23. For both conditions, a cyclic four-state model describes the data best (see Fig. 4.2).

Interestingly, exclusively transitions starting from a closed state are affected by the addition of p23. The transition rates between the two closed states of Hsp90 (states 2 and 3 in Fig. 4.2) are slowed down in the presence of p23. Also, the rate for re-opening of the closed Hsp90 (transition 2→1) is decreased. As a consequence, this leads to a slight increase of the state population of state 2 by a factor of about 1.5 (from 2.7% to 4.0%).

Unfortunately, it is not a straightforward task to directly assign the states from the

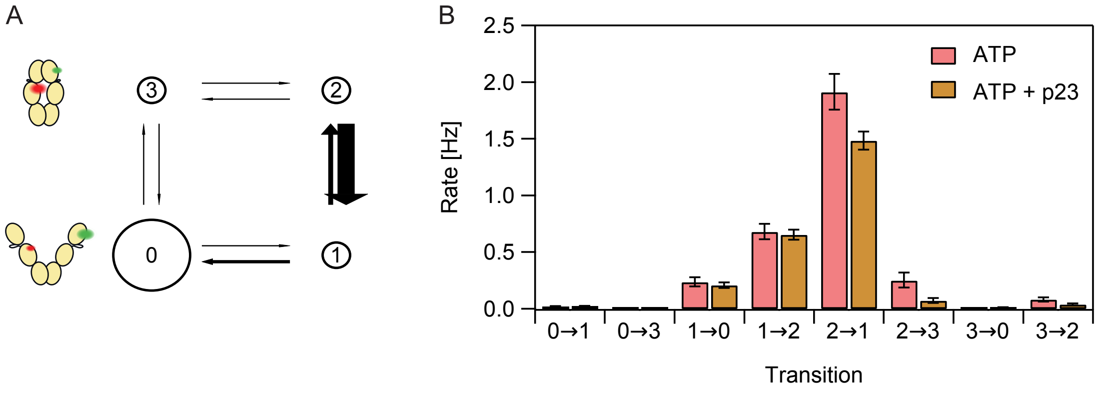

Figure 4.2: Effects of p23 on the global conformational dynamics of Hsp90. (A) States 0 and 1 correspond to N-terminal open Hsp90, states 2 and 3 to the N-terminal closed conformation. (B) Measurements were conducted with Hsp90 D61C-Atto550/Q385C-Atto647N-biotin in the absence or presence of 20 µM p23 in H buffer with 2 mM ATP and at RT. Rates re-opening the short-lived closed state (state 2 in the model, transitions 2→1) and rates between the two closed states (2→3 and 3→2) are decreased in the presence of p23. Error bars represent the 99% confidence intervals.

HMM to functional states of the Hsp90 complex (potentially in combination with p23). Also, an ambiguity exists where the actual hydrolysis occurs in the shown network of states [116]. Several secondary structure elements can regulate the available conformational flexibility of Hsp90, including the catalytic loop, the ATP lid, the N-terminal β-strand and the charged linker. Their interplay is only poorly understood so far. In principal, adding measurements with co-chaperones would open up a “new dimension” and could help in assigning functional states to the (conformational) states obtained from the HMM. However, the mechanism of p23 function itself is not yet understood in great detail.

As p23 is reported to interact with the nucleotide-bound, closed state of Hsp90 and to decrease ATPase activity, two possible inhibition mechanisms are possible: Either p23 inhibits the hydrolysis process (or a step leading to it) directly or it impedes the subsequent release of the products ADP and $\mathrm{P_i}$ [111]. There is experimental evidence for both mechanisms. NMR data shows that p23 binding affects the ATP lid in solution and changes the environment of the nucleotide in its binding pocket [61]. This finding was suggested to favor a model of the ATPase cycle slowdown by preventing a step necessary for hydrolysis [111]. In contrast, the crystal structure of yeast Hsp90 shows the catalytic loop in a hydrolysis-active position in the presence of p23 [5] and the ATPase activity of Hsp90 under single turnover conditions with p23 is not inhibited significantly [36], indicating that p23 slows down a step after the actual hydrolysis.

The most likely scenario under this circumstances is that the closed, hydrolysis competent state of Hsp90 is reached from an open conformation directly and is thus not influenced by p23. After hydrolysis, re-opening of Hsp90 is slowed down by p23 as it inhibits necessary conformational re-orientations in the closed state. This model also im-

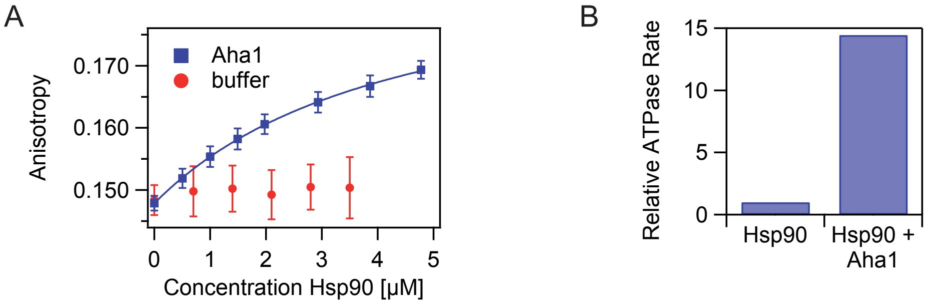

Figure 4.3: Binding of Aha1 to Hsp90. (A) Fluorescence anisotropy assay to monitor the binding of 500 nM Aha1 S85SCO-Atto550 to Hsp90. Fitting with the quadratic equation for equilibrium binding yields a K_d of 4.0 ± 2.1 µM, with respect to the Hsp90 monomer. Addition of buffer (40 mM HEPES pH 7.0, 20 mM KCl, 10 mM $MgCl_2$) alone does not change the anisotropy signal. (B) The ATPase rate of wt Hsp90 is increased by a factor of about 15 by addition of 20 µM wt Aha1. ATPase rates are normalized to the rate of Hsp90 alone.

plies that the crystal structure of closed Hsp90 in combination with p23 (PDB 2CG9) does not correspond to the transition state of the hydrolysis, but to a closed conformation trapped by p23. This is in line with conclusions drawn from mutational studies [18] and the fact that AMP-PNP is commonly used to trap the active sites of another family of ATPases (AAA+) in their ground states, but not in their transition state [16].

4.1.2. Effects of Aha1 on Hsp90

Wild-type Aha1 from yeast contains three cysteines which impede the introduction of a single cysteine point mutant for site-specific labeling. Instead, a construct with an unnatural amino acid (cyclooctyne-lysine, SCO) at position Ser85 is used. This allows labeling with azid-derivatives of the Atto dyes in a copper-free click chemistry reaction. The binding of the S85SCO Aha1 variant was characterized with a fluorescence anisotropy assay (Fig. 4.3A). The dissociation constant under low salt and apo conditions (i.e. without nucleotide) is 3.9 ± 0.3 µM with respect to the Hsp90 monomer. This is higher than reported values (0.33 µM [95] or 1.2 µM [73]), however these publications do not report the used buffer conditions even though binding of Aha1 is known to be salt-dependent [95].

Next, smFRET measurements were performed to study the interaction between Aha1 and Hsp90 in more detail. It was already shown that wt Aha1 has no strong influence on the N-terminal conformational changes of Hsp90 [115]. Interestingly, this is a behavior that is shared between Aha1 and p23 and is in stark contrast to the influence of these co-chaperones on the ATPase activity of Hsp90. However, this does not exclude more subtle effects of Aha1 on Hsp90. In a first step, the binding and dissociation of Aha1 and Hsp90 was followed with a smFRET experiment in the presence of a saturating ATP concentration. Hsp90 labeled with the donor dye in the CTD is attached to the surface and Aha1 labeled with the FRET acceptor is in solution. The resulting FRET efficiency

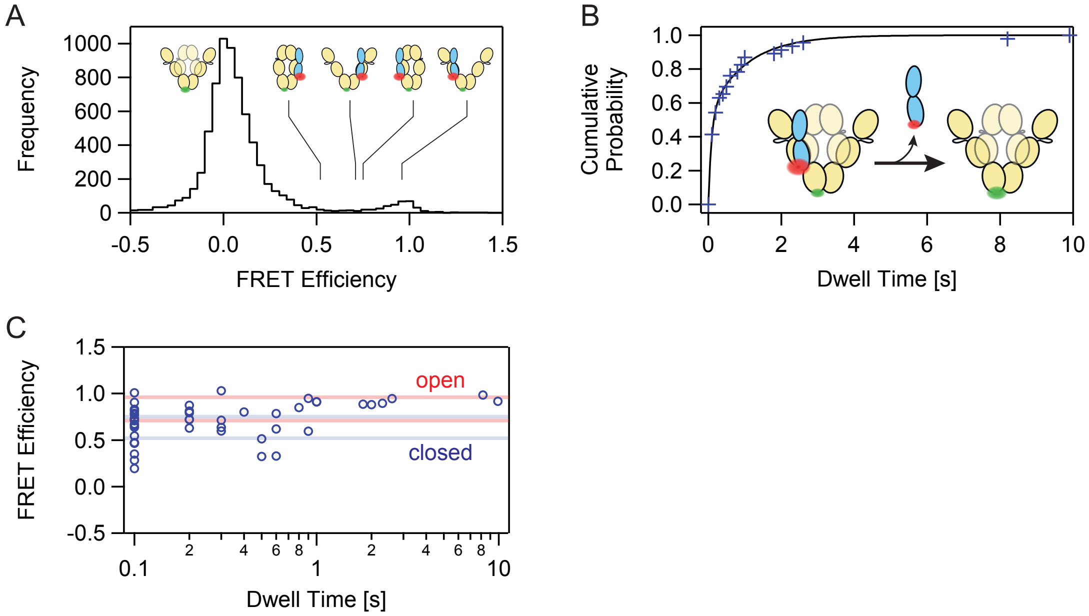

Figure 4.4: A smFRET assay monitoring the binding of 50 nM Aha1 S85SCO-Atto647N to a heterodimer of Hsp90 K637C-Atto550-biotin/wt in presence of 2 mM ATP. (A) FRET efficiency histogram for molecules that show at least one Aha1 binding event. Expected values are zero for unbound Aha1 as well as medium and high FRET efficiency for Aha1 bound to the closed and open conformation of Hsp90, respectively. (B) Dwell time histogram for the dissociation of the Hsp90-Aha1 complex. The cartoon indicates the reaction and the approximate label positions. The black line is a fit with the sum of two exponential functions ($A_1 = 0.53, \tau_1 = 0.09\,\mathrm{s}, A_2 = 0.47, \tau_2 = 1\,\mathrm{s}$). (C) The mean FRET efficiency during the dwell versus the dwell time for the same data as shown in (B). Longer dwells have a slightly higher FRET efficiency. The expected FRET efficiencies for the two Hsp90 conformations (open, closed) are indicated with red and blue lines.

histogram is shown in Figure 4.4A. The interaction of Aha1 and Hsp90 is quite dynamic compared to the slow ATPase rate of Hsp90, with a lifetime of the Aha1-bound state on the order of magnitude of one second under the tested conditions (Figure 4.4B). As Hsp90 is a dimer and Aha1 can bind to either of the monomers (with only one being labeled) two distances between the dyes and thus two FRET efficiencies are expected for each conformation of Hsp90: 0.96 and 0.71 for open Hsp90 and 0.75 and 0.52 for closed Hsp90 (roughly indicated by red and blue horizontal lines in Fig. 4.4C, respectively). Longer dwells at the same time also have a higher FRET efficiency, implying that Aha1 is bound longer to open Hsp90 in the presence of ATP.

To probe another dimension of possible manipulation of the Hsp90-Aha1 system, different available Hsp90 inhibitors where tested for their efficacy to affect the binding of Aha1 to Hsp90 (Fig. 4.5). Several classes of small molecule inhibitors of Hsp90 have been identified by natural product-based drug discovery and rational drug design [65].

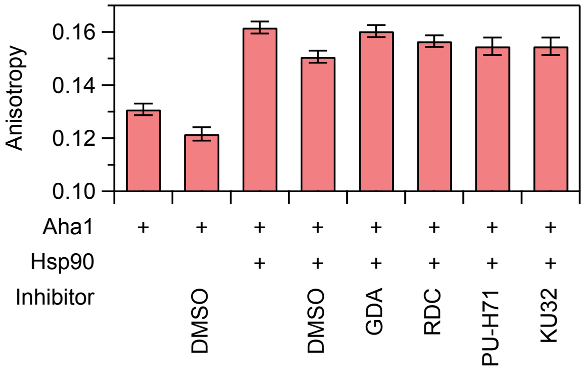

Figure 4.5: Fluorescence anisotropy of Aha1 binding to Hsp90 tested with different small molecule Hsp90 inhibitors. Drugs that target the N-terminal ATP binding site of Hsp90: Geldanamycin (GDA) [20, 142], Radicicol (RDC) [21, 119, 123] and the purine-derived compound PU-H71 [51]. The novobiocin-derivative KU-32 [7] binds to Hsp90's C-terminal domain. 200 nM Aha1 S85SCO-Atto647N was incubated at 25°C in the absence or presence of 10 µM Hsp90 Czip wt and 50 µM inhibitor. Thus, inhibitor concentrations were at least 50-fold higher than the reported dissociation constants, or the half maximal inhibitory concentration (IC_{50}) if the former was not available. Inhibitors were added from stock solutions in DMSO.

They can be grouped into N-terminal and C-terminal inhibitors with the first ones interacting with the nucleotide binding pocket and also inhibiting the ATPase function of Hsp90 [65] while the latter ones bind to a weak C-terminal nucleotide-binding site [23]. Mechanisms for the mode of action of any of these inhibitors *in vivo* still remain elusive.

However, neither the global N-terminal kinetics (data by Sonja Schmid [116], not shown) nor the Aha1 binding are affected significantly by the four tested inhibitors.

4.1.3. Discussion and Outlook

In summary, several subtle effects on Hsp90 could be observed for the co-chaperones p23 and Aha1 with the used approaches and under the tested conditions.

In the case of Aha1, a prolonged binding to the open conformation of Hsp90 in the ATP state was observed. Since AMP-PNP bound, closed Hsp90 is reported to bind Aha1 with higher affinity [95, 73], two mechanisms are conceivable. Either, Hsp90 with ATP does not reach the specific closed state that permits a more stable binding of Aha1 as with AMP-PNP. Or, the thermodynamically more stable bound state (with closed Hsp90) also exists with ATP, but is kinetically more dynamic. This would be possible if both on- and off-rate of Aha1 are increased compared to open Hsp90, with the on-rate being accelerated to a higher degree. Additional experiments in the presence of AMP-PNP could distinguish between these two alternatives.

The global N-terminal kinetics of Hsp90 are not strongly affected by either of the two co-chaperones. As a consequence, p23 does not induce directionality in the four-state

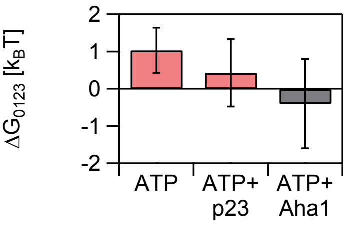

Figure 4.6: Neither p23 nor Aha1 introduce significant directionality to the succession of states for Hsp90 in presence of ATP. Errors for ΔG are propagated from the 95% CIs of the rates along the cycle. The value for Aha1 is taken from Ref. [115].

conformational cycle of Hsp90 in the presence of ATP (Fig. 4.6) – the same outcome that was reported for Aha1 [115]. This is not in opposition to a previously proposed directionality found for the binding of labeled ATP and p23 to the closed conformation of Hsp90 [110], because a different cycle was probed in these experiments.

Bacterial, yeast and mammalian Hsp90's show ATPase activity and mutations preventing the hydrolysis ATP are mostly lethal *in vivo*. An evolutionary tendency to decrease the ATPase rate of Hsp90 seems obvious, however it is not abolished even in high eukaryotes. Thus, the ATPase must be part of Hsp90's function. This naturally raises the question of how the energy from ATP hydrolysis is used in yeast in Hsp90. Closely related is the question of the functional states of Hsp90. Clearly, even the more elaborate distinction between two open and two closed (kinetic) states of Hsp90 is not enough. An even higher "resolution" by probing different local motifs of Hsp90 with single-molecule methods is needed for a full understanding.

4.2. The Hsp90 Model-Substrate Δ131Δ

A fragment of the Staphylococcal nuclease (SN) that comprises residues 1–3 and 13–140 of the 149-residue wild-type protein is referred to as Δ131Δ [4, 3]. It lacks six structural residues (i.e. residues that are resolved in the crystal structure of full length SN, PDB 1SNC [75]) from the N-terminus and one structural residue from the C-terminus [138]. Δ131Δ was first introduced in the field of protein folding, along with other fragments of SN, as a destabilized version of the native state [124, 4]. It was used to study the structure and dynamics in the unfolded state of SN and the sequence of the folding pathway.

In solution, Δ131Δ adopts a conformational ensemble that is globally unfolded but remains compact, with partial formation of secondary structure that is very similar to elements found in the native state [4, 3, 138]. In the presence of high concentrations of SN substrate, Δ131Δ can fold to a structure highly similar to that of the native state according to enzymatic activity, NMR and CD data [4]. This suggests that Δ131Δ is close in free energy to the native state of SN [128].

Apart from that, Δ131Δ is highly soluble, monomeric even at high concentrations and stable under a wide variety of conditions [4, 128]. This makes it an excellent model-substrate for Hsp90, since – unlike most other proteins – the unfolded state is not difficult to populate and not prone to misfolding or aggregation [128]. Also, even if Hsp90 could refold Δ131Δ, this would not lead to an accumulation of the native state as this state is energetically less favorable.

4.2.1. Bulk Interaction Assays

A protocol for the purification of wild-type Δ131Δ from inclusion bodies was obtained from the Agard lab (Daniel Elnatan). This protocol was modified in order to also work with single- and double-cysteine mutants. A protocol for labeling with maleimide-functionalized Atto dyes was established (see Section B.4.3 in the Appendix).

In a first step, the specific binding of Δ131Δ to Hsp90 was characterized with a fluorescence anisotropy assay (see Fig. 4.7). Addition of 5 µM BSA or PEG 10 kDa do not result in a change in the fluorescence anisotropy. In contrast, addition of 5 µM Hsp90 leads to a clear increase of the anisotropy. Interestingly, wt Hsp90 (“noZip” in Fig. 4.7) seems to bind Δ131Δ with higher affinity than the construct used for single-molecule measurements (including a C-terminal coiled-coil motif for stable dimerization).

The dependence of the fluorescence anisotropy on the rotational diffusion of a molecule is given by the Perrin equation [99, 70]. Rotational diffusion of the fluorophores leads to fluorescence depolarization. The rotational correlation times for two processes are of importance here: the restricted motion of the fluorophore (attached to the protein with a linker) near the protein surface and the slower overall motion of the macromolecule. The protein rotation is governed by it’s molecular weight and shape, which also explains the increase in fluorescence anisotropy upon complex formation, assuming no significant influence on the rotational flexibility of the dye itself. The steady-state anisotropy is a result of both of these depolarizations, in relation to the excited state lifetime of the fluorophore, τ_{fl}. A significant increase in the steady state anisotropy signal upon complex formation can only be expected if τ_{fl} is not much smaller than the rotational correlation time of the macromolecule [94]. Assuming a hydrodynamic radius of 20 Å for Δ131Δ [145] and a spherical shape, the rotational correlation time can be estimated to be 8 ns. The fluorescence lifetimes of Atto550 and Atto647N are 3.6 ns and 3.5 ns, respectively, according to the manufacturer. Thus, a fluorophore with longer fluorescence lifetime would be more sensitive on the overall rotation of Δ131Δ. A possible candidate is IAEDANS (with $\tau_{fl} = 10 - 15$ ns). However, preliminary tests with this dye and Δ131Δ resulted in a low labeling efficiency.

Next, the dissociation constant was determined with an equilibrium binding assay and increasing Hsp90 concentrations (Fig. 4.8A). The K_d is found to be 14 ± 2 µM with respect to the Hsp90 monomer. Assuming a stoichiometry of one Δ131Δ per Hsp90 dimer this is in excellent agreement with the reported K_d of 6 µM (if this value refers to the dimer concentration of Hsp90) [128].

Furthermore, the ATPase activity of Hsp90 is increased by addition of wt Δ131Δ (Fig. 4.8B). This is in line with the reported acceleration of the ATPase of HtpG by Δ131Δ [128]. However, client activation of the ATPase activity may not be a general concept in the class of Hsp90 chaperones. Varying or contradicting results have been obtained for different clients and one and the same client results in different stimulation

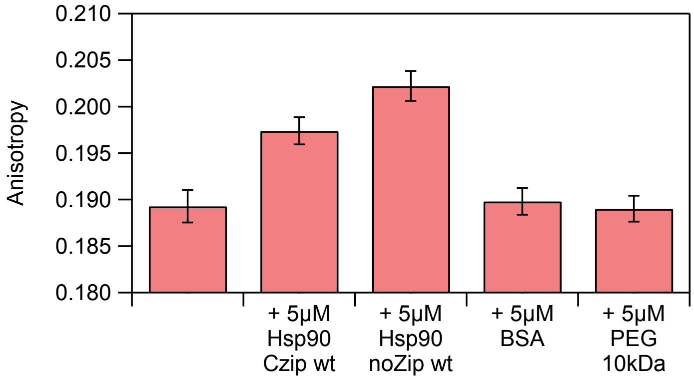

Figure 4.7: The model-substrate Δ131Δ specifically binds to Hsp90. Fluorescence anisotropy assay to monitor the binding of different compounds to 0.5 µM Δ131Δ K16C-Atto647N in H buffer at 25°C. Error bars represent the standard deviation of the recorded anisotropy data points (10 min measurement with a data point taken every 5 sec). No unspecific binding of Δ131Δ to BSA or PEG is detectable.

depending on the origin (i.e. the species) of the Hsp90. In most cases, a stimulatory effect on the Hsp90 ATPase activity is found: α-Synuclein [24], the ligand binding domain of the glucocorticoid receptor (GR-LBD) [81], Δ131Δ [128] and the ribosomal protein L2 [89]. However, α-Synuclein's influence on Hsp90 is debated [116] and L2 stimulates the ATPase of HtpG but not of yeast Hsp90. The GR-LBD stimulates the ATPase of both human and yeast Hsp90 [81], while a stabilized mutant of GR-LBD inhibits the ATPase activity of yeast Hsp90 in a concentration-dependent manner [76].

The diffusion times of Δ131Δ under different nucleotide conditions was determined with fluorescence correlation spectroscopy (FCS) (Table 4.1). Addition of 10 µM Hsp90 under all tested nucleotide conditions results in a marked increase of the diffusion time of fluorescently labeled Δ131Δ. The effect is strongest for ADP. This may indicated that Δ131Δ preferentially binds to the open state of Hsp90. For the *E. coli* homologue HtpG a more compact configuration upon addition of AMP-PNP even in the presence of the model-substrate was reported [128], which could also explain the less pronounced increase of the diffusion time under AMP-PNP conditions. Nonetheless, both open and closed conformation of Hsp90 are able to interact with Δ131Δ. This renders models which suggest an “ejection” of client protein upon closing of Hsp90 during its functional cycle less likely.

In preparation of smFRET experiments, different positions in Hsp90 where tested for their potential to monitor the binding of Δ131Δ to the chaperone. These positions where chosen due to their proximity to the putative interaction of Δ131Δ on Hsp90 interface in the dimer cleft of Hsp90 [128] (see also Fig. 4.9A). Labeling position E431 in Hsp90 gives a FRET signal upon Δ131Δ binding (Fig. 4.9B).

To check if Hsp90 has an influence on the conformational ensemble of Δ131Δ, a double-cysteine mutant of the model-substrate with the labeled positions near the N- and the C-terminus was used (Fig. 4.10). Binding to Hsp90 does not drastically influence the structure of Δ131Δ. However a slight increase in the FRET signal can be observed

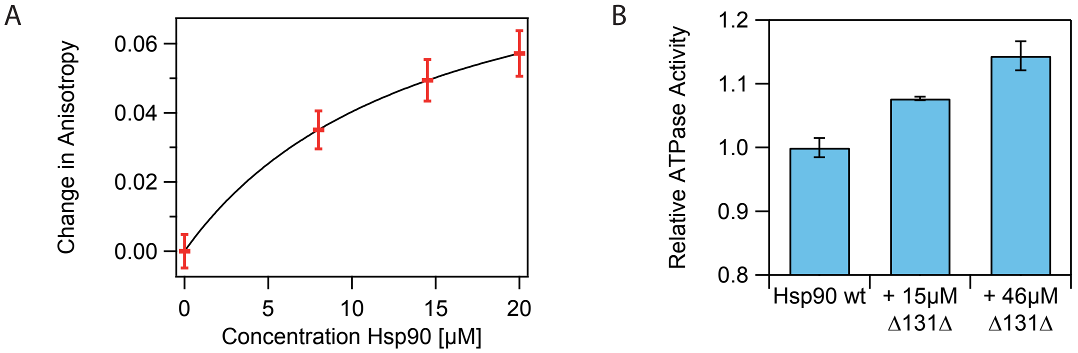

Figure 4.8: Bulk measurements of the interaction of Δ131Δ with Hsp90. (A) Change of fluorescence anisotropy as a function of Hsp90 concentration in H buffer at RT. The black line is a fit to the data with the quadratic equation for equilibrium binding, yielding a K_d of 14 ± 2 µM with respect to the Hsp90 monomer. Error bars represent the standard deviation of the anisotropy signal. (B) Relative ATPase activity of Hsp90 in dependence of Δ131Δ at 37°C. Mean and standard deviation of duplicates.

Sample	Average diffusion time [ms]
Δ131Δ	1.0
+ 10 µM Hsp90 + 2 mM AMP-PNP	1.8
+ 10 µM Hsp90 + 4 mM ATP	2.2
+ 10 µM Hsp90 + 4 mM ADP	2.5

Table 4.1: Diffusion times of Δ131Δ K16C-Atto647N. Measurements by Björn Hellenkamp.

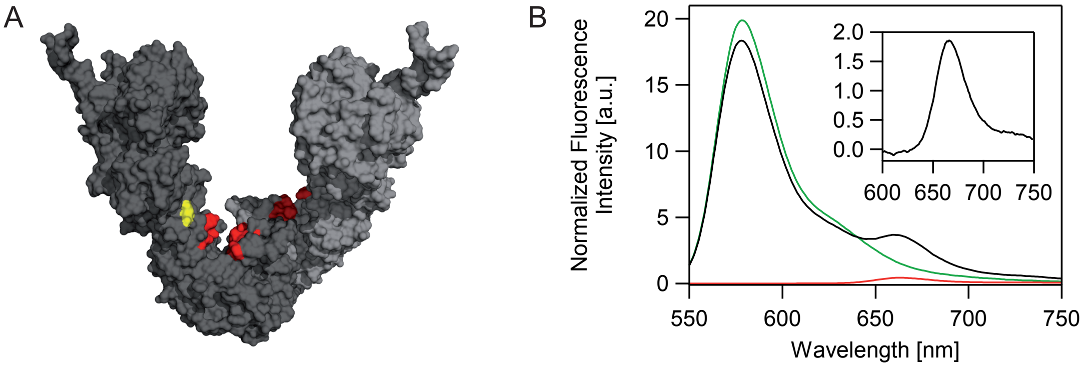

Figure 4.9: FRET assay for the interaction of Hsp90 and Δ131Δ. (A) Open conformation of Hsp90 [43]. Highlighted in yellow is position E431 in Hsp90 and shown in red are homolog residues reported to impair the interaction with client proteins in HtpG [30]. (B) Fluorescence spectra of donor only (1 µM Hsp90 E431C-Atto550, green), acceptor only (1 µM Δ131Δ K16C-Atto647N, red) and donor plus acceptor (black) in H buffer at 22°C. The inset shows the change in acceptor fluorescence intensity upon addition of acceptor.

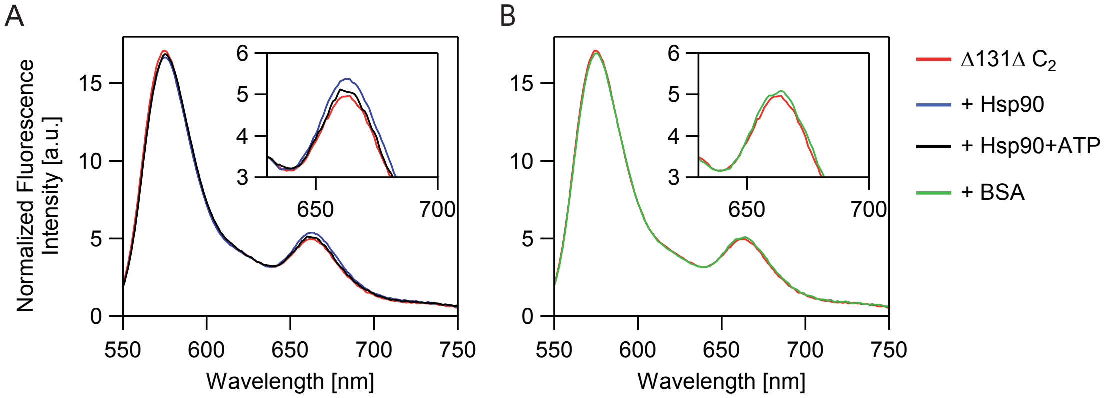

Figure 4.10: FRET assay for the effect of Hsp90 on the conformation of Δ131Δ. (A) The conformation of the double-cysteine variant Δ131Δ C_2 (K16C, L137C; "statistically" labeled with a mix of Atto550 and Atto647N) is only slightly affected by addition of 10 µM Hsp90 or 10 µM Hsp90 + 5 mM ATP. The inset shows a zoom-in of the FRET peak. (B) Control experiment. 10 µM BSA does not influence the conformation of Δ131Δ.

upon addition of Hsp90, indicating a decreased distance between the termini or an overall compaction of the model-substrate. This disfavors a model where Hsp90 acts as a clamp that closes around Δ131Δ in a way comparable to Hsp90 wedging itself between the two lobes of the kinase Cdk4 [136].

4.2.2. Single-Molecule FRET Experiments

In order to characterize the influence of the model-substrate Δ131Δ on Hsp90 and to gain direct conformation specific information, a single-molecule FRET experiment was performed. The Hsp90 heterodimer D61C-Atto550/Q385C-Atto647N-NHS-biotin in the absence or presence of unlabeled Δ131Δ was studied. This Hsp90 variant was chosen because it is well-characterized on the single-molecule level [85, 109, 115] and because it reports on the global N-terminal conformation of the chaperone. For the *E. coli* homologue of Hsp90, HtpG, a partial closing of the open conformation around Δ131Δ under conditions without nucleotide was reported [128]. This study used small-angle X-ray scattering (SAXS) measurements to infer the global structure of Hsp90.

Using smFRET, the N-terminal conformation of Hsp90 can be probed directly. As the affinity of Hsp90 for the model-substrate Δ131Δ is rather low, high concentrations are needed to cause saturated binding. Approximately 100 µM Δ131Δ where used, i.e. about seven times the K_d. The model-substrate induces a shift of the open conformation to smaller efficiencies (Fig. 4.11A). Assuming that the dye mobility is not severely influenced by Δ131Δ binding (the AVs of the dyes for the used variant do not point towards the interaction site, see Fig. 4.11B), this can be explained either by an unlikely rotation of the MD of Hsp90 or by a further expansion of the open state. FCS measurements under different nucleotide conditions by Björn Hellenkamp indicate that Δ131Δ may preferentially bind to Hsp90's open state [42].

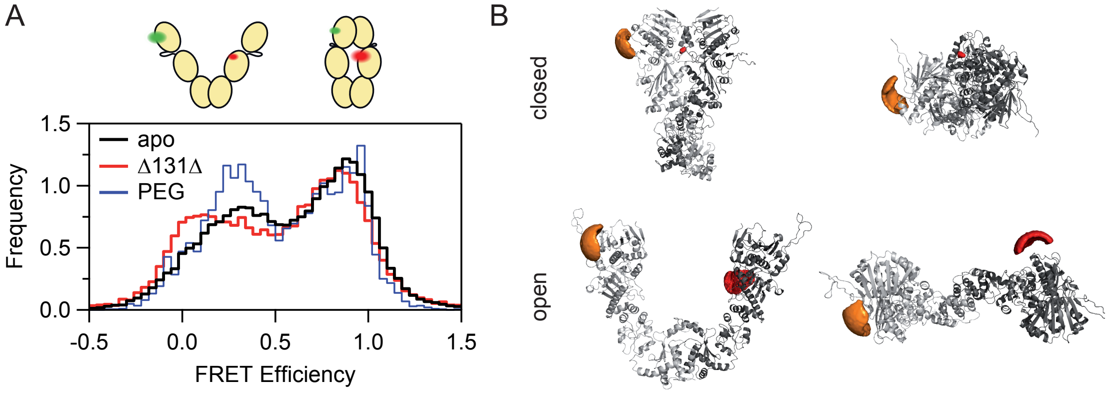

Figure 4.11: Influence of Δ131Δ binding on Hsp90 in a smFRET experiment. (A) FRET efficiency histogram for the Hsp90 heterodimer D61C-Atto550/Q385C-Atto647N-NHS-biotin in H buffer at RT in the absence of further compounds (apo, black) or in the presence of either approx. 100 µM Δ131Δ (red) or 100 µM PEG (10 kDa, blue). Addition of PEG does not drastically change the position of the peaks, while Δ131Δ induces a shift of the open conformation to smaller efficiencies. (B) Accessible volumes for Atto550 (orange) and Atto647N (red) for the closed (top row) and open conformation (bottom row). A front and a top view of Hsp90 are shown. Structures are taken from Refs. [5] and [43].

In order to exclude any unspecific effects due to the Δ131Δ concentration, also a control measurement with a comparable concentration of polyethylene glycol (PEG) was performed. The molecular weight of the PEG was chosen to roughly match the dimensions of Δ131Δ, as estimated from the end-to-end distances of PEG and a fully unfolded protein the size of Δ131Δ. 100 µM PEG 10 kDa corresponds to 0.1% weight/volume, which is well below concentrations typically used for crowding agents and thus no effect of the addition of PEG is expected. Differences in the population of the open/closed conformation can be attributed to different measurement techniques (no ALEX for the apo and Δ131Δ data; this also explains the significant over-population of the closed state under apo conditions).

Unfortunately, further single-molecule experiments that also directly probe the presence of Δ131Δ are not feasible with a TIRF setup as the on- and off-rates for the binding to Hsp90 are too fast. The change of chemical shifts in NMR experiments indicates that the interaction is in “intermediate exchange” [129], which means in the millisecond range [66]. This agrees well with data obtained by Björn Hellenkamp from fast mixing experiments on a confocal setup.

4.2.3. Discussion and Outlook

The special nature of Δ131Δ makes it a convenient model-substrate for Hsp90. Most clients of the Hsp90 system are thought to be late folding intermediates that have already formed a significant amount of secondary and even tertiary structure [55, 56, 146, 97, 22, 62, 117].

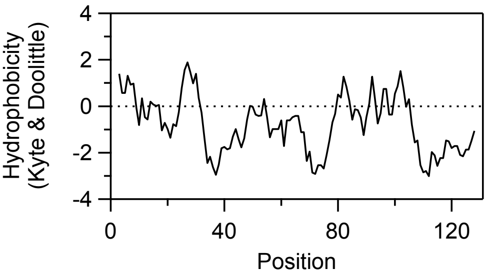

Figure 4.12: Hydrophobicity of Δ131Δ along its amino acid sequence. The plot was created using the ExPASy ProtScale tool [28].

The results obtained for Δ131Δ suggest that primarily the open state of Hsp90 is affected by binding of the model-client. Interestingly, wild-type Hsp90 seems to bind Δ131Δ stronger than the construct with a C-terminal zipper motif used in single-molecule experiments. The zipper might restrict C-terminal fluctuations and thereby prevent Hsp90 from sampling all possible conformations. The putative interaction site of Δ131Δ is in the cleft between the two MDs and CTDs of Hsp90 [128] and might be sensitive to small changes in this region of Hsp90. This allows one to speculate that the highly flexible open conformation of Hsp90 is a prerequisite for its interaction with a broad range of diverse clients.

This also fits well with a previously proposed model for Hsp90's client interaction pattern [62]. An extended substrate binding interface is suggested to distribute moderate hydrophobic interaction over a large surface area. The hydrophobicity of Δ131Δ along its sequence is shown in Figure 4.12. The region of increased hydrophobicity between amino acids 80 and 110 matches nicely to the reported interaction area (residues 85 to 110) found by NMR experiments [128]. Relying on distributed, weak interactions allows Hsp90 to flexibly adapt to the needs of a distinct client.

4.3. The Nucleotide Binding Pockets of Hsp90 Act Cooperatively

Main parts of the work presented in this section are published in Wortmann, Götz & Hugel (2017) [144].

The interplay between Hsp90's conformational changes, nucleotide binding and nucleotide hydrolysis is still enigmatic [98] and several experiments have provided controversial results:

On the one hand, ATP binding and hydrolysis weakly affect the conformational equilibrium between the globally open and closed conformations of Hsp90 [126, 115, 147]. In addition, experimental studies could not reveal any cooperativity in nucleotide binding or hydrolysis [82, 18]. These findings hint towards a weak intramolecular communication between the two subunits of the dimer, or even its absence.

On the other hand, a stable N-terminal closed structure of the otherwise predominately open Hsp90 dimer is observed upon the incubation with the non-hydrolyzable ATP analogue AMP-PNP [5, 43]. A recent study suggests a coordination of local conformational changes in structural elements linked to nucleotide binding within one subunit [120]. Moreover, mutational studies have demonstrated that the hydrolysis activity is affected differently in dimers lacking the ability to either bind or hydrolyze ATP in one NTD [93, 113, 86]. These results imply a communication within each Hsp90 subunit, as well as between the two nucleotide binding pockets in the dimer, despite the lack of direct evidence.

The standard procedure to assess the coordination between two binding sites of a ligand (i.e. cooperativity) in a protein is the evaluation of Hill plots from bulk experiments, where the binding site occupation is measured as a function of ligand concentration. Cooperativity leads to a deviation from a linear scaling, i.e. a slope of one in a log-log plot. However, this analysis is limited by the simplifications of the underlying models [127] and weak cooperativity is hardly detectable. In the case of Hsp90 no strong cooperativity can be expected, because most interactions with clients, co-chaperones and nucleotides do not exhibit strong effects neither on the conformation nor on the kinetics of the conformational changes. Possible cooperative effects are therefore unlikely to be detected by the application of standard approaches.

Multi-color smFRET experiments are advantageous in this situations for two reasons: First, they can be more sensitive because they allow detecting even rare events that would be lost in bulk averaging. Second, multi-color smFRET experiments can directly measure the correlation between two interactions as not only one distance is probed. This abrogates the need for indirect deductions from titration measurements as in the case of a Hill plot.

4.3.1. A Single-Molecule FRET Approach

Studying the interaction of Hsp90 and a labeled reporter nucleotide directly and in real time by the application of three-color smFRET allows resolving the states of the interaction between Hsp90 and nucleotides. Hsp90's global conformation is tracked by measuring FRET between two fluorophores attached to the opposing subunits in the Hsp90 dimer (D61C-Atto488/Q385C-Atto550-biotin). At the same time, the presence of a reporter nucleotide (γ-[(6-Aminohexyl)-imido]-AMP-PNP-Atto647N, abbreviated AMP-PNP*) in one of the two nucleotide binding pockets is probed by FRET. For a detailed description of the three-color smFRET measurement and the extraction of kinetic information using a 3D HMM approach, refer to Chapter 3. The used setup is depicted in Figure 4.13.

The reporter nucleotide AMP-PNP* binds to Hsp90 with approximately 100 times higher affinity than unlabeled AMP-PNP. Using fluorescence anisotropy, the K_d for AMP-PNP* is estimated to be $480 \pm 95\,\mathrm{nM}$ (see Fig. 4.14) while the reported K_d for AMP-PNP and yeast Hsp90 is $33\,\mu\mathrm{M}$ [102]. However, AMP-PNP* binds to the nucleotide binding pocket of Hsp90 similar to the unlabeled nucleotide (see Fig. A.3 in the Appendix) because it can be displaced with AMP-PNP or ATP (at medium to high micromolar concentrations) and it does not bind an Hsp90 mutant that is deficient in

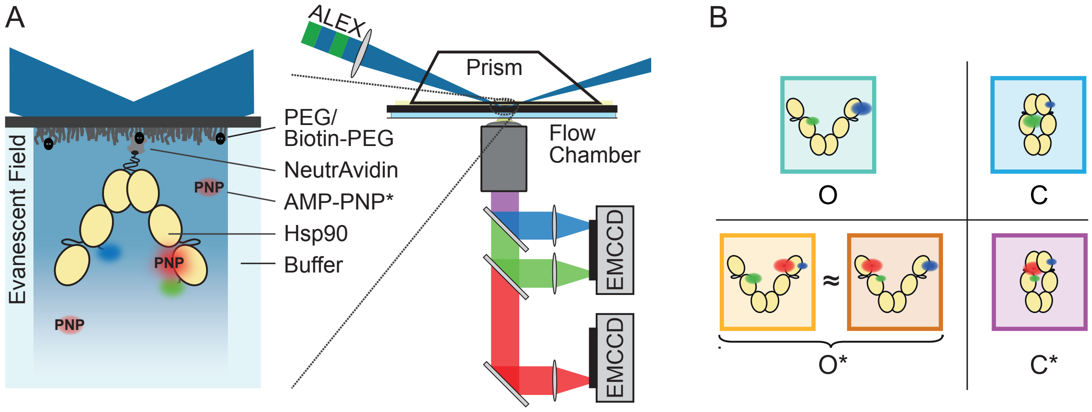

Figure 4.13: Three-color smFRET setup for measurement of nucleotide effects. (A) The studied system consists of an Hsp90 dimer with the dyes Atto488 (blue) and Atto550 (green) attached and the reporter nucleotide AMP-PNP* in solution (labeled with Atto647N; red). The protein is immobilized by NeutrAvidin/biotin interaction on the top of the flow chamber and excited by an evanescent field using alternating laser excitation (ALEX) with a blue and a green laser. The fluorescence light is collected by an objective, separated by dichroic mirrors and detected with EMCCD cameras. The setup is detailed in Section 3.1. (B) Pictograms of the distinguishable states and their respective identifier used in this work. Two populations represent the same functional state, namely open Hsp90 with AMP-PNP* bound. Figure adapted from Ref. [144].

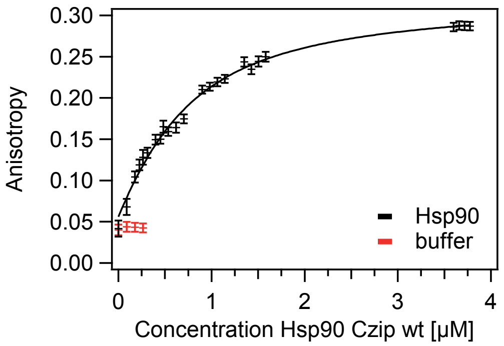

Figure 4.14: Binding of 500 nM AMP-PNP* to Hsp90 Czip wild-type in H buffer, measured by fluorescence anisotropy at 25°C (black). Error bars represent the standard deviation of the signal recorded for about 2 min. The fit with the quadratic equation for equilibrium binding (black line) results in an apparent K_d of 480 ± 95 nM, with respect to the Hsp90 monomer (assuming independent binding of the labeled nucleotide to Hsp90). A buffer control is shown in red.

nucleotide binding (D79N). It is possible to ensure that only one AMP-PNP* is bound at a time and that the second nucleotide binding site is accessible to unlabeled nucleotide for all molecules subjected to further analysis in two ways: First, the used concentration of AMP-PNP* (25 nM) is well below the K_d and second, molecules that may show binding of two AMP-PNP* are excluded in the trace selection process. The fact that AMP-PNP* is non-hydrolyzable and binds to the nucleotide binding pocket of Hsp90 with higher affinity than the unlabeled nucleotide makes it a highly useful reporter for the influence of additional, native nucleotide or the global conformation of Hsp90 on the nucleotide binding properties.

4.3.2. Average Dwell Time of the Reporter Nucleotide

With the three-color smFRET approach, the period of time an AMP-PNP* molecule stays bound to Hsp90, can be measured (Fig. 4.15A). Analyzing more than 800 such dwells, the average dwell time of AMP-PNP* bound to Hsp90 is found to be 5.9 ± 0.3 s (Fig. 4.15B). If the two nucleotide binding pockets of Hsp90 were independent, i.e. no cooperativity between them existed, the addition of unlabeled nucleotide would not affect the average dwell time of the reporter nucleotide already bound to Hsp90. Surprisingly, under conditions with additional, unlabeled ATP or AMP-PNP, the average dwell time is increased significantly by almost 50% to 8.8±0.3 s. The same effect is found when comparing the “time to absorption” (TTA), which does not average the observed dwell times of the Viterbi path but gives the average time it takes a molecule to diffuse through the state network to reach a state without bound AMP-PNP* – starting in an AMP-PNP* bound state and with transition probabilities optimized to the data. Thus, the binding of a second nucleotide to the Hsp90 dimer decreases the apparent overall dissociation probability of the reporter nucleotide AMP-PNP* (averaged over all conformations of Hsp90), i.e. the two nucleotide binding pockets are not independent of

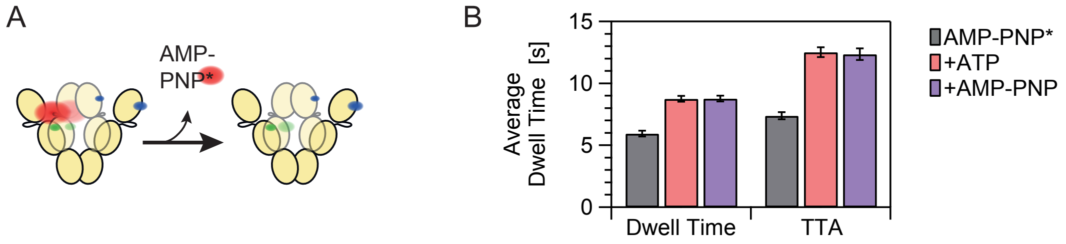

Figure 4.15: The average dwell time of the reporter nucleotide AMP-PNP* bound to Hsp90 is prolonged by additional nucleotide. (A) Pictogram of the observed dissociation of labeled AMP-PNP* from the Hsp90 dimer. (B) Average dwell time (“unbounded”) of AMP-PNP* bound to Hsp90 in absence of additional nucleotide (black) and in presence of 250 µM unlabeled ATP (red) or unlabeled AMP-PNP (purple). The average dwell time is calculated either as average of the observed dwells in the Viterbi paths or as the “time to absorption” (TTA) (see Section A.2 in the Appendix). Error bars represent the standard deviation calculated from ten 75% subsets. Figure adapted from Ref. [144].

each other. In other words, there exists cooperativity between the two binding pockets of Hsp90.

4.3.3. Nucleotide and Aha1 Binding Affect Distinct but Interfering Steps

The ATPase activity of Hsp90 is known to be affected by regulatory co-chaperones. The strongest stimulating effect so far has been found for Aha1, with a more than tenfold acceleration of the ATPase activity [95]. Thus, the effect of Aha1 on the complex interplay of nucleotide binding and N-terminal dimerization (both prerequisite for hydrolysis) deserves further studying. Aha1’s influence on the cooperativity in nucleotide binding was tested by the addition of 10 µM of wild-type Aha1 to the assay. In the absence of additional ATP, Aha1 alone already increases the mean dwell time of the reporter nucleotide bound to Hsp90 from 5.9 ± 0.3 s to 7.7 ± 0.4 s (Fig. 4.16A). Surprisingly, the combination of Aha1 and ATP increases the dwell time of AMP-PNP* (7.0 ± 0.4 s) to a lesser degree than either Aha1 or ATP do. Thus, the effects of ATP and Aha1 are not simply additive.

Figure 4.16B shows, how the conformation of Hsp90 is changed by the addition of Aha1. The O*/C* ratio of Hsp90 bound to AMP-PNP* is shifted towards the C* state. In contrast to the findings for the dwell times, the combination of ATP and Aha1 leads to a more pronounced effect on the O*/C* ratio than each of them separately. Because the dwell time of AMP-PNP* and the conformation of Hsp90 are differently affected by Aha1 and ATP, they have to affect independent processes of Hsp90. However, these processes have to interfere with each other.

The underlying cause of these effects remains unclear at this stage as the dwell times and populations alone are not sufficient to describe the system. For example, the increase in the population of C* could be due to an increase in the rates leading to this state or due to a decrease in the rates depopulating this state.

Thus, a kinetic description of the system, that resolves all relevant states, is required to gain insights into the actual mechanism mediating the cooperativity in Hsp90. For a system with more than two states, this is currently only possible by a single-molecule approach.

Additional ATP affects the nucleotide dissociation and the conformational transitions differently (Fig. 4.16C). On the one hand, additional ATP decreases the rates for AMP-PNP* dissociation from both the open and the closed state of Hsp90 (O*→O and to a lesser extent C*→C). On the other hand, the equilibrium between the labeled nucleotide bound populations of Hsp90 is shifted by both, increasing the rate for closing (O*→C*) and decreasing the rate for opening (C*→O*). Since the bleach rates in all data sets are similar (see Fig. A.4 in the Appendix), these effects are not caused by a different temporal resolution. Thus, cooperativity is not the result of ATP affecting one single rate, but by the combined effects of the nucleotide on four rates in the studied system.

Aha1 alone accelerates the transition from open, AMP-PNP* bound Hsp90 to the closed state (O*→C*), even stronger than 250 µM ATP. In combination with ATP, the effects of both on this transition actually add up. In contrast, the transitions from closed Hsp90 with AMP-PNP* bound to the open state as well as the dissociation of labeled nucleotide from open Hsp90 are increased to values similar to the ones observed without ATP and Aha1. Therefore, Aha1 attenuates these additional effects of ATP.

4.3.4. Discussion

Several structural elements of Hsp90 are known to be involved in the nucleotide binding. At least two of these, the catalytic loop [84] and the ATP lid [125], are also related to Aha1 binding. These two elements are depicted in Figure 4.17A.

The presented data and the 3D HMM analysis allow a deeper insight into the kinetic causes for the cooperativity and to propose a kinetic model that combines the global conformation of Hsp90 and the nucleotide binding state (Fig. 4.17B). The cooperativity has been missed in Hill plots and other bulk experiments so far, because it is not very strong. The addition of ATP accelerates the closing of AMP-PNP* bound Hsp90 (O*→C*). Besides, it decelerates the opening of AMP-PNP* bound Hsp90 (C*→O*) and the dissociation of AMP-PNP* from open Hsp90 (O*→O). The structural origins of these effects could either be a communication between the two nucleotide binding sites through the whole dimer [93, 88] or a direct interaction between the domains of the two subunits. Direct steric contacts of the two NTDs in the open state are possible because the open conformation of Hsp90 represents a flexible and highly dynamic ensemble [43].

Furthermore, the data reflects the role of Aha1 as an accelerator of Hsp90's conformational rearrangements and ATPase activity [95, 104]. Aha1 accelerates the transition from the open nucleotide bound to the closed nucleotide bound state (O*→C*) in absence of additional nucleotide. The co-chaperone has been reported to modulate the catalytic loop of Hsp90 in a way that facilitates the conformational transition from open to closed Hsp90 [84, 112]. This effect is suggested to be present even in the absence of nucleotide [45]. It can be speculated that this is the structural cause for the observed kinetic effect.

The addition of both, ATP and Aha1 to the assay allows further and novel insights into

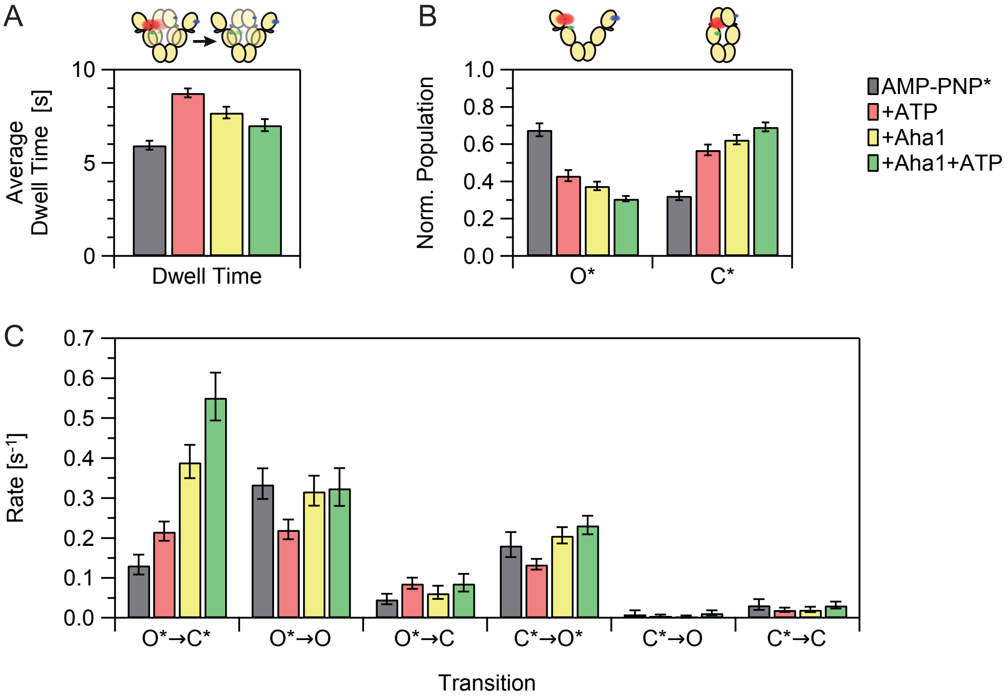

Figure 4.16: Effect of ATP (250 µM, red), Aha1 (10 µM, yellow) and Aha1 in combination with ATP (green) on Hsp90 and AMP-PNP*. (A) The mean dwell time of AMP-PNP* bound to Hsp90 is increased by Aha1. The effect observed for Aha1+ATP is smaller than for ATP or Aha1 alone. (B) Population of open (O*) and closed (C*) conformation of Hsp90 bound to AMP-PNP* (normalized to unity). The addition of nucleotide or co-chaperone or a combination of both results in a population shift to the closed conformation. (C) The transition rates and the effects of nucleotide, co-chaperone and their combination. Error bars in (A) and (B) represent the standard deviation calculated from ten 75% subsets and the 99% confidence interval in (C). Figure adapted from Ref. [144].

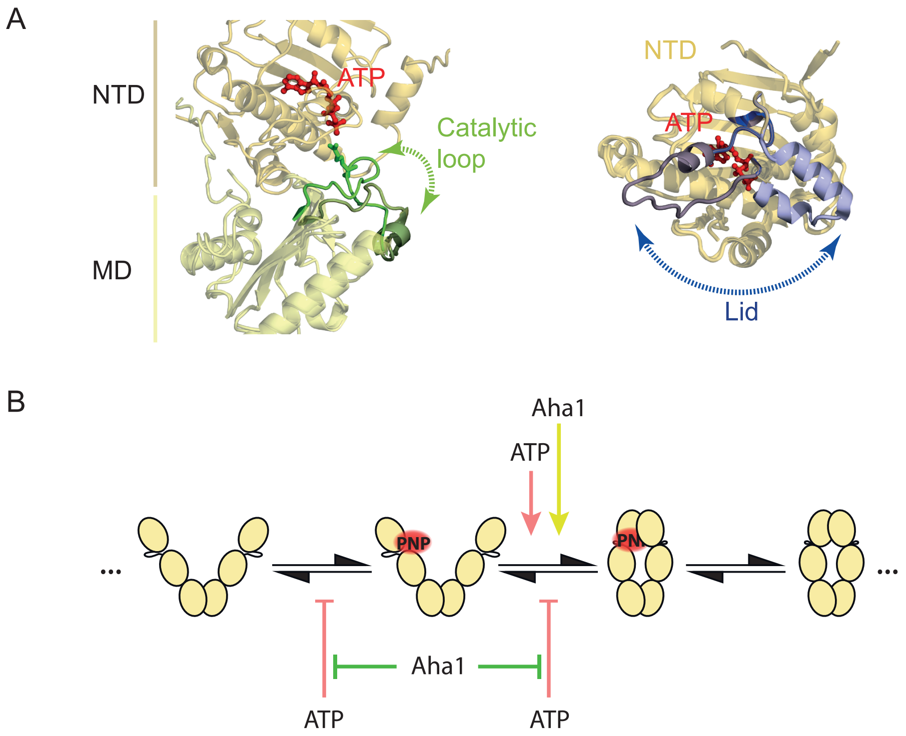

Figure 4.17: The effects of ATP and Aha1 on the state transitions of Hsp90 and their possible structural origins. (A) Local rearrangements that are linked to Aha1 and nucleotide binding. Reported rearrangement of the catalytic loop upon binding of Aha1 (left; green and dark green, superposition of the crystal structures PDB 2CG9 [5] and 1USV [84]). Reported conformation of the nucleotide lid in the AMP-PNP or the ADP bound crystal structures (right; dark and light blue, superposition of the crystal structures PDB 2CG9 and 2WEP [103]). (B) A minimal model for the state transitions of Hsp90 in presence of AMP-PNP* and the effects of ATP and Aha1 on these transitions. Only the most frequent transitions are shown. ATP increases the closing rate of Hsp90 with AMP-PNP* bound, and decelerates the reverse reaction, as well as the dissociation of AMP-PNP*. Aha1 also accelerates the closing of AMP-PNP* bound Hsp90. In a combination of Aha1 and ATP, their effects on the closing of AMP-PNP* bound Hsp90 add up, while Aha1 prevents the decelerating effects of ATP. Figure adapted from Ref. [144].

the distinct effects of nucleotide and co-chaperone on Hsp90's conformational dynamics. Their common and strongest effects, accelerating the closing of open, AMP-PNP* bound Hsp90 (O*→C*), add up. Because the concentration of Aha1 in the experiment is close to saturation [95, 125, 112], the co-chaperone is most likely already exerting its full activation potential. Nevertheless, the transition can be further accelerated by the addition of ATP. Therefore, it can be inferred that ATP and Aha1 affect different structural rearrangements independently, both resulting in an accelerated closing of Hsp90. The decelerating effect of ATP on the opening of AMP-PNP* bound Hsp90 and dissociation of AMP-PNP* from open Hsp90 is abolished by Aha1. Thus, a structural arrangement leading to a tighter binding of nucleotide is impeded by the co-chaperone when both binding pockets are occupied. This means that, on the one hand, ATP and Aha1 work to the same aim (namely the closure of the dimer). On the other hand, they act antagonistic on two different state transitions (i.e. the opening of dimer and the dissociation of nucleotide). These effects are summarized in Figure 4.17B.

Aha1 may have a more active part in the closure of the ATP lid and the N-terminal dimerization then has been suggested previously [125]. The ATP data shows, that addition of ATP accelerates the closure of AMP-PNP* bound Hsp90 (O*→C*), indicating that lid closure is rate limiting for this transition. Then, Aha1 also has to accelerate reaching the closed-lid conformation in order to speed up the N-terminal dimerization.

The observed cooperativity between the nucleotide binding sites explains several previously observed effects of point mutations in one of the nucleotide binding pockets of functional Hsp90 heterodimers. For example the effects of point mutants which impair nucleotide binding (D79N) or hydrolysis (E33A) on the ATPase activity of the dimer. On the one hand, an Hsp90 heterodimer (D79N/wt) able to bind ATP in only one subunit exhibits an increased Michaelis-Menten constant K_M [113, 86]. This decreased apparent nucleotide affinity is readily explainable by the proposed kinetic model, because no cooperativity can occur in this situation. On the other hand, an Hsp90 heterodimer (E33A/wt) able to bind two ATPs, but with the ability to hydrolyze only one, displays a decreased K_M [86]. Thus, the presence of a non-hydrolyzable nucleotide increases the apparent nucleotide affinity. The presence of a second binding site, but absence of the potential for hydrolysis in one subunit mirrors the experiment with AMP-PMP* and ATP. According to the proposed model in Figure 4.17B, this results in an increase in closed nucleotide-bound Hsp90. That is in turn the conformational prerequisite for hydrolysis, since a correlation between the population of the closed conformation of Hsp90 and the ATPase rate has been reported [41, 147]. The cooperativity between the two pockets is an additional aspect of Hsp90's cross-monomer coordination, which happens before the actual hydrolysis reaction [18].

One observation worth mentioning is the fact that the presence of ATP in one binding pocket and AMP-PNP* in the other results in a larger population of the closed state, an effect that could be observed previously only in excess of AMP-PNP (i.e. both binding pockets are occupied by AMP-PNP), but not in excess of ATP [5, 85, 115, 43]. Thus, binding of one AMP-PNP* (and most likely AMP-PNP) results in a conformational change that is the prerequisite for a more stable N-terminal dimerization. Nucleotide has been proposed to affect the lid dynamics of Hsp90 [102], which can then facilitate the N-M arrangement necessary for the transition into the closed Hsp90 conformation. This molecular arrangement would explain the decreased opening rate (C*→O*) as well.

5. Conclusion

In the first part of this work, a novel three-color smFRET approach is developed and validated. Switching from two-color to three-color smFRET experiments adds another dimension to the analysis of biomolecular machines. Thereby, it becomes possible to directly access the correlation between molecular interactions and conformational changes on the single-molecule level and in real time. This is essential to fully understand biological multi-state and multi-component systems. The approach is robust enough to also meet the special needs of single-molecule measurements on a dynamic chaperone system, namely Hsp90. This large, multi-domain protein switches between at least two distinct global conformations and has a plethora of interaction partners.

The three-dimensional signal (i.e. the distances between the three dyes) and the broad distribution of the different states in the PF space necessitate a two-step approach. In the first step, the position and width of each states is extracted from the 3D PF histogram of the complete data set. In the second step, an ensemble HMM optimizes a kinetic state model for the complete data set. This method proves to work robust and reproducible with the inherently noisy three-color smFRET data.

The second part of the work comprises different approaches to elucidate critical steps in Hsp90's functional cycle. Eukaryotic Hsp90 acts in combination with a number of co-chaperones. Two prominent representatives – Aha1 and p23 – are tested and found to induce subtle changes in Hsp90. However, they are not able to fundamentally change the characteristic N-terminal dynamics of the chaperone.

A similar result was obtained for the model-substrate $\Delta 131\Delta$ that is found to specifically bind to Hsp90 and preferentially affect the open conformation of Hsp90. Still, changes in the conformational equilibrium of Hsp90 are modest.

This leaves room for two interesting conclusions: Possibly, only a more sophisticated combination of co-chaperones, potentially also with components from the Hsp70 chaperone cycle and substrates, is able to transform eukaryotic Hsp90 in a "processive" molecular machine and to add the regulatory mechanism that seems to be absent in Hsp90 alone. In contrast, the bacterial homologue (HtpG) can be strongly influenced by nucleotide binding all by itself [108]. Interestingly, this evolution from an independently working complex to a multi-component machinery is also true for other large, multi-protein complexes (e.g. RNA polymerases). An alternative explanation is that Hsp90 evolved from a rigid system to a more flexible one, not being the active component of the complex anymore but rather the scaffold for other proteins to assemble. In this scenario, Hsp90's flexibility would be beneficial to allow for a dynamic formation of different complexes. The actual "work", i.e. the chaperoning and maturation of the clients, is then performed by co-chaperones.

Another project focused on the nucleotide binding of Hsp90. A previously overlooked weak cooperativity between the two nucleotide binding pockets of the Hsp90 dimer is found and the kinetic causes of this cooperativity are identified. The direct observation of the influence of one Hsp90 subunit on the other abolishes the need for an indirect inference by titration experiments and Hill-like plots to detect cooperativity. The cooperativity is not caused by an effect of ATP on a single rate, but by the combined effects of the nucleotide on four rates in the studied system. The results also demonstrate that cross-effects of different interaction partners (nucleotide binding and Aha1 in this case) have to be taken into account in order to understand the Hsp90 chaperone machinery to its full extent. Besides, co-chaperones most likely affect more than one single step in the functional cycle of Hsp90 in general. Both ideas might also apply to many other catalytic systems with more than one interaction partner.

Appendices

A. Supplementary Information

A.1. Supplementary Figures

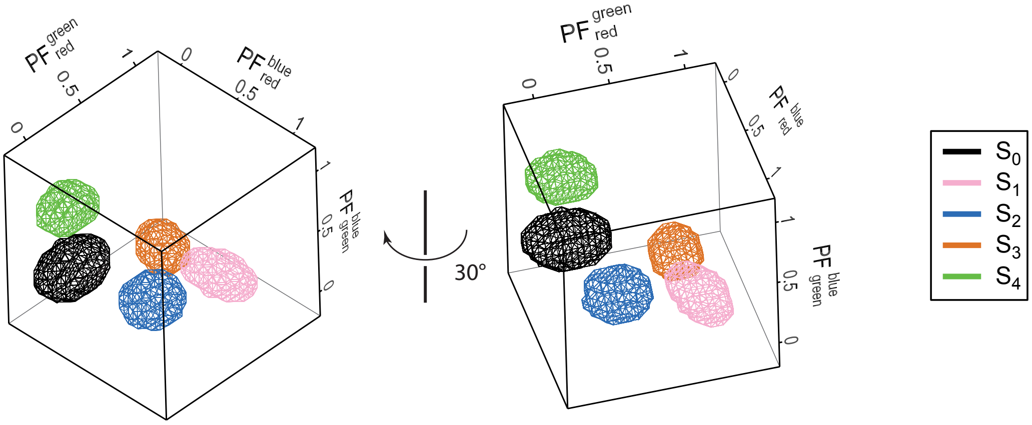

Figure A.1: 3D representation of the five emission PDFs in the PF space. Isosurfaces indicate the full width at half maximum of the probability- density functions.

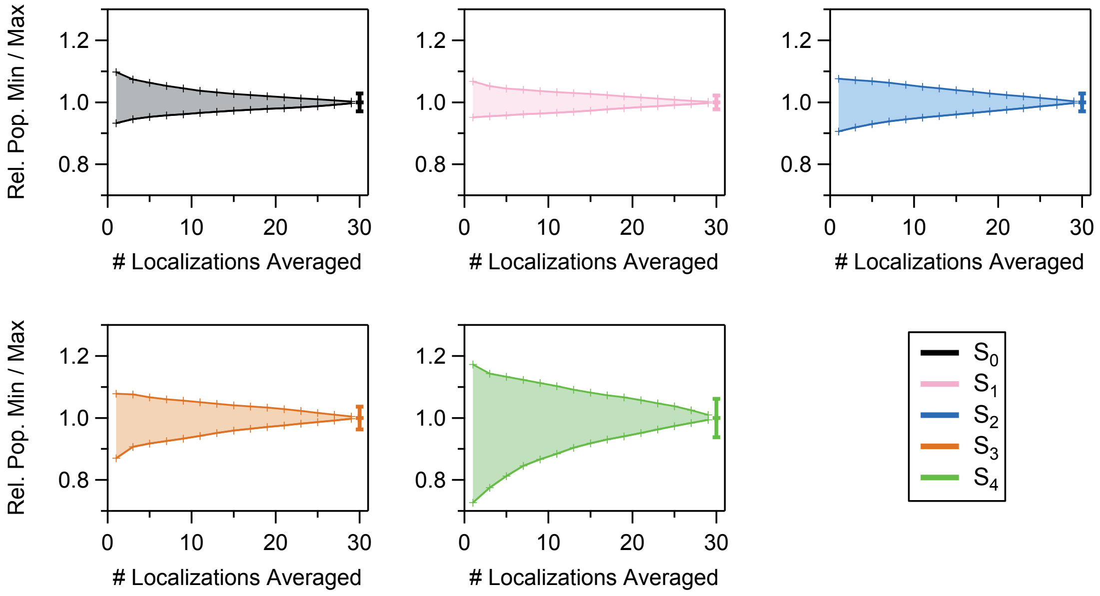

Figure A.2: Convergence of minimal and maximal population with increasing number of localizations. Shown in bold is the average and standard deviation from all 30 localizations.

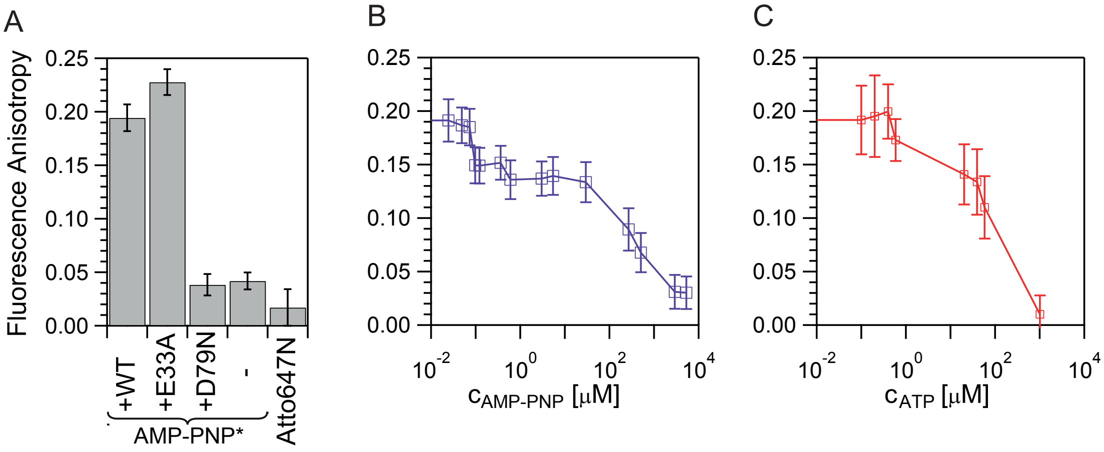

Figure A.3: Control experiments to confirm that AMP-PNP* binds to the nucleotide binding pocket of Hsp90 similar to the unlabeled nucleotide. (A) AMP-PNP* binds to Hsp90 wt and E33A but not to D79N. (B) and (C) AMP-PNP* can be displaced by a micromolar concentration of AMP-PNP or ATP. Measurements performed by Philipp Wortmann. Figure adapted from Ref. [144].

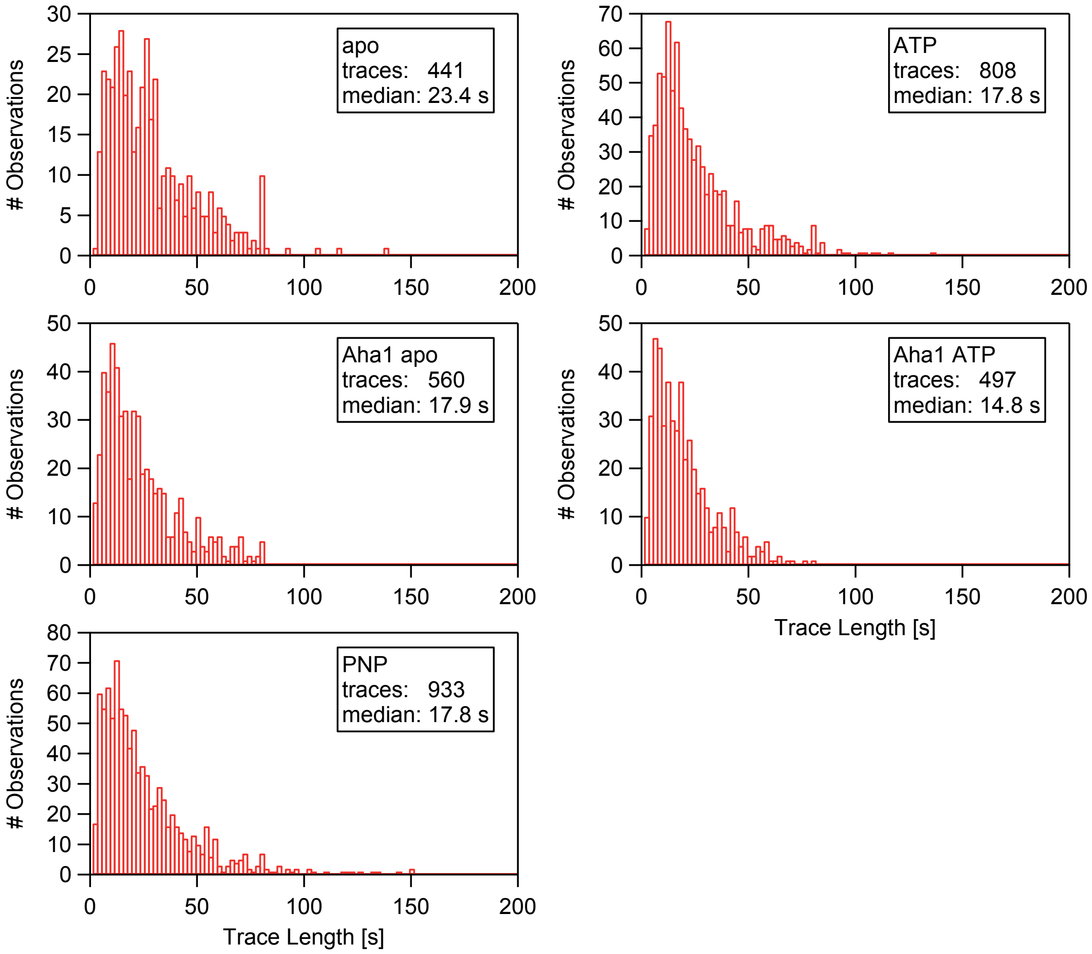

Figure A.4: Histograms of the trace lengths for the different experimental conditions. Temporal resolution: 200 ms per excitation cycle. Figure adapted from Ref. [144].

A.2. Calculation of the Time to Absorption

In the following, the calculation of the time to absorption is given for the merged "apo" data set. Transition probabilities are given in 1/frame, where one frame corresponds to 200 ms. For a more detailed description see the main text, Section 3.6, page 37.

transition matrix

$$\boldsymbol{A} = \begin{array}{c} \\ \mathrm{S}_0 \\ \mathrm{S}_1 \\ \mathrm{S}_2 \\ \mathrm{S}_3 \\ \mathrm{S}_4 \end{array} \begin{array}{c} \begin{array}{ccccc} \mathrm{S}_0 & \mathrm{S}_1 & \mathrm{S}_2 & \mathrm{S}_3 & \mathrm{S}_4 \end{array} \\ \begin{pmatrix} 0.976 & 0.000573 & 0.0111 & 0.00676 & 0.00523 \\ 0.00182 & 0.955 & 0.0269 & 0.00941 & 0.00639 \\ 0.0317 & 0.0147 & 0.944 & 0.000424 & 0.00931 \\ 0.035 & 0.0116 & 0.00222 & 0.951 & 5.23 \cdot 10^{-63} \\ 0.063 & 0.019 & 0.035 & 7.35 \cdot 10^{-44} & 0.883 \end{pmatrix} \end{array} \tag{A.1}$$

transition matrix of the absorbing Markov chain

$$\boldsymbol{A'} = \begin{array}{c} \\ \mathrm{S}_1 \\ \mathrm{S}_2 \\ \mathrm{S}_3 \\ \mathrm{S}_0 \\ \mathrm{S}_4 \end{array} \begin{array}{c} \begin{array}{ccccc} \mathrm{S}_1 & \mathrm{S}_2 & \mathrm{S}_3 & \mathrm{S}_0 & \mathrm{S}_4 \end{array} \\ \begin{pmatrix} 0.955 & 0.0269 & 0.00941 & 0.00182 & 0.00639 \\ 0.0147 & 0.944 & 0.000424 & 0.0317 & 0.00931 \\ 0.0116 & 0.00222 & 0.951 & 0.035 & 5.23 \cdot 10^{-63} \\ 0 & 0 & 0 & 1 & 0 \\ 0 & 0 & 0 & 0 & 1 \end{pmatrix} \end{array} \tag{A.2}$$

transition matrix between the non-absorbing states

$$\boldsymbol{Q} = \begin{array}{c} \\ \mathrm{S}_1 \\ \mathrm{S}_2 \\ \mathrm{S}_3 \end{array} \begin{array}{c} \begin{array}{ccc} \mathrm{S}_1 & \mathrm{S}_2 & \mathrm{S}_3 \end{array} \\ \begin{pmatrix} 0.955 & 0.0269 & 0.00941 \\ 0.0147 & 0.944 & 0.000424 \\ 0.0116 & 0.00222 & 0.951 \end{pmatrix} \end{array} \tag{A.3}$$

expected time in state i when starting in state j, with $N = \{n_{ij}\}$

$$\begin{aligned} \boldsymbol{N} = (\boldsymbol{I}_3 - \boldsymbol{Q})^{-1} &= \left(\begin{pmatrix} 1 & 0 & 0 \\ 0 & 1 & 0 \\ 0 & 0 & 1 \end{pmatrix} - \begin{pmatrix} 0.955 & 0.0269 & 0.00941 \\ 0.0147 & 0.944 & 0.000424 \\ 0.0116 & 0.00222 & 0.951 \end{pmatrix} \right)^{-1} \\ &= \begin{pmatrix} 28.5 & 13.9 & 5.61 \\ 7.50 & 21.5 & 1.63 \\ 7.12 & 4.28 & 21.9 \end{pmatrix} \end{aligned} \tag{A.4}$$

expected time in state i

$$\boldsymbol{t} = \boldsymbol{N}\,\boldsymbol{1} = \begin{pmatrix} 28.5 & 13.9 & 5.61 \\ 7.50 & 21.5 & 1.63 \\ 7.12 & 4.28 & 21.9 \end{pmatrix} \cdot \begin{pmatrix} 1 \\ 1 \\ 1 \end{pmatrix} = \begin{pmatrix} 48.0 \\ 30.6 \\ 33.3 \end{pmatrix} \tag{A.5}$$

$$\tau_{TTA} = \frac{1}{\|\boldsymbol{\pi'}\|}\, \boldsymbol{\pi'} \cdot \boldsymbol{t}\ , \text{ with} \quad \boldsymbol{\pi'} = \begin{array}{c} \pi_1 \\ \pi_2 \\ \pi_3 \end{array} \begin{pmatrix} 0.133 \\ 0.173 \\ 0.106 \end{pmatrix} \tag{A.6}$$

$$\tau_{TTA} = 37 \text{ (frames)} = 7.4\,\text{s} \tag{A.7}$$

B. Supplementary Material and Methods

All chemicals were purchased from Sigma-Aldrich (St. Louis, USA) in the highest available grade, if not stated otherwise.
The standard measurement buffer (termed “H buffer”) is 40 mM HEPES, 150 mM KCl, 10 mM $MgCl_2$, pH 7.5. A 10× stock of the H buffer can be prepared with a pH 7.8 to yield the correct pH after dilution. If Atto488 is present in any step, additional 0.5 mg/mL BSA are added to the buffer.

B.1. Concentration Determination

If not stated otherwise, concentrations of proteins or nucleotides were determined photometrically with a NanoDrop 1000 (Thermo Scientific) and refer to the monomer in the case of Hsp90.

Sample	ϵ_{280} or ϵ_{259} $[\mathrm{M}^{-1}\mathrm{cm}^{-1}]$
Hsp90 Czip	75’290
Aha1	50’545
p23	29’900
Δ131Δ	15’930
SENP	35’660
nucleotide	15’400

Dye	ϵ_{max} $[\mathrm{M}^{-1}\mathrm{cm}^{-1}]$	cf_{280}
Atto488	90’000	9%
Atto550	120’000	12%
Atto647N	150’000	5%

Table B.1: Molar extinction coefficients for the used proteins and fluorophores. The correction factor cf_{280} is used to correct the protein absorption at 280 nm according to $A_{280}^{\mathrm{corr}} = A_{280} - cf_{280} \cdot A_{\mathrm{max}}$. Values for the proteins are determined with the ExPASy ProtParam tool [28]. Values for the dyes are taken from the manufacturer.

B.2. Protein Expression and Purification

If not stated otherwise, the *Saccharomyces cerevisiae* homologues were used for all proteins.

B.2.1. Hsp90

Hsp90 (Hsp82 in yeast, UniProtKB ID P02829) is used either as wt protein or with a C-terminal coiled-coil motif (denoted “Czip”) from the kinesin neck region of *Drosophila* *melanogaster* (DmKHC) that prevents dimer dissociation at picomolar concentrations in single molecule experiments [85]. smFRET experiments are done with “Czip” single cysteine variants, some of which additionally carry a biotinylated tag (AviTag) at the far C-terminus (indicated by the identifier “biotin” in the main text). The His-SUMO tag is cleaved during purification. The AviTag (Avidity LLC) is a unique 15 amino acid peptide sequence for specific *in vivo* biotinylation. As wild-type yeast Hsp90 contains no native cysteines, single cysteine mutants allow one to specifically attach one fluorescent dye per subunit. The mutants are created by site-directed mutagenesis (QuikChange Lightning, Agilent).

The Hsp90 constructs are contained in pET28 vectors and expressed from *Escherichia coli* BL21 (DE3) or BL21 Star (DE3) cells in the case of AviTag constructs (Thermo Fisher Scientific).

Standard expression is done in LB medium supplemented with 50 µg/mL kanamycin at 37°C and inoculation from an over-night culture (1:100). Cells are induced at an OD_{600} of 0.6 by addition of 1 mM IPTG. After 3 h cells are harvested by centrifugation (20 min, 4°C, 3’000 rpm, JLA 8.1, Avanti JXN-26, Beckman Coulter), resuspended in phosphate buffered saline (PBS) and pelleted again (10 min, 4°C, 4’600 rpm, Rotanta 460R, Hettich). Cell pellets are frozen in liquid nitrogen and stored at -20°C until purification.

For *in vivo* biotinylation, the biotin ligase (BirA) is co-expressed from pBirAcm (Avidity LLC) following the manufacturer’s instructions. In short, TB medium is supplemented with 0.5% glucose and 30 µg/mL kanamycin (note that no chloramphenicol is added during expression while it has to be present at 10 µg/mL for any other step to sustain pBirAcm). Expression is induced at an OD_{600} of 0.7 by adding 1 mM IPTG and 50 µM D-biotin (from a 5 mM stock, in warm 10 mM bicine buffer pH 8.3, filter-sterilized). After induction for 3 h at 37°C, cells are harvested by centrifugation, washed with PBS and pelleted again.

For purification, the cells are re-suspended in approx. 30 mL 50 mM sodium phosphate pH 8.0, 300 mM NaCl and lysed with a Cell Disruptor (Constant Systems) at 1.6 kbar. Cell debris is pelleted by centrifugation at $30'000 \times g$ at 4°C for 45 min (JA-25.50, Avanti JXN-26, Beckman Coulter). If necessary, 2 mM $MgCl_2$ and 3 µL benzonase can be added and incubated 15 min at room temperature (RT). After filtration (Filtropur S 0.45, Sarstedt) 20 mM imidazole is added from a 1 M stock, the solution is applied to a 5 mL HisTrap HP (GE Healthcare) and eluted by a linear gradient from 20 to 500 mM imidazole in 50 mM sodium phosphate pH 8.0, 300 mM NaCl at 8°C. Protein-containing fractions are pooled and dialyzed against the imidazole-free buffer overnight in the presence of 1/100 equivalent SENP protease. This protease cuts off the N-terminal His-SUMO sequence, leaving the native, tag-free protein [96]. The solution is again applied to the HisTrap column and the flow-through is collected and diluted 1:3 with ddH_2O to decrease the ionic strength. After applying to a HiTrap Q HP 5 mL (GE Healthcare), the protein is eluted with a linear gradient from 50 mM to 1 M NaCl in 40 mM HEPES pH 7.5. Hsp90 fractions are pooled and concentrated using centrifugal filters with a

50 kDa molecular weight cut-off (Amicon Ultra, Merck Millipore). Finally, the protein is applied to a HiLoad 16/600 Superdex200 (GE Healthcare) and eluted with 40 mM HEPES, 200 mM KCl pH 7.5. Peak fractions are again pooled and concentrated to 50–100 µM. Aliquots are snap-frozen in liquid nitrogen and stored at -80°C until further usage. Expression and purification is monitored by SDS-PAGE and final sample purity typically exceeds 95%.

B.2.2. Ah1

Aha1 (UniProtKB ID Q12449) is either used as wild-type protein or with an unnatural amino acid incorporated at position S85 for copper-free click chemistry.

The wt construct is contained in pET28a and expressed with a cleavable N-terminal His-SUMO tag. *E. coli* BL21 Star (DE3) (Thermo Fisher Scientific) are grown at 37°C in TB medium with 50 µg/mL kanamycin to an OD_{600} of 0.6 and induced with 1 mM IPTG for 4 h. Cells are harvested by centrifugation, washed with PBS, pelleted again and stored at -20°C. Cell pellets are re-suspended in PBS and lysed in a Cell Disruptor (Constant Systems) at 1.6 kbar. Cell debris is pelleted by centrifugation at $25'000 \times g$ at 4°C for 30 min (JA-25.50, Avanti JXN-26, Beckman Coulter). After filtration (Filtropur S 0.45, Sarstedt), the cell lysate is applied to a 5 mL HisTrap HP (GE Healthcare) and eluted by a linear gradient from 0 to 500 mM imidazole in 100 mM sodium phosphate, 300 mM NaCl pH 8.0 at 8°C. Protein-containing fractions are pooled and dialyzed against the imidazole-free buffer overnight at 8°C in the presence of 1/100 equivalent SENP protease to cleave the His-tag. The solution is again applied to the HisTrap column and the flow-through is collected and diluted 1:3 in 40 mM MES, 40 mM NaCl pH 6 and subsequently applied to a HiTrap SP HP 5 mL (GE Healthcare). The protein is eluted with a linear gradient to 40 mM MES, 1 M NaCl pH 6. Protein is reduced with 1 mM DTT and concentrated. Finally, it is applied to a HiLoad 16/600 Superdex200 (GE Healthcare) and eluted with 40 mM HEPES, 200 mM KCl pH 7.5. Sample purity is checked by SDS-PAGE.

The Aha1 S85SCO variant (with an amber stop codon at position S85) is expressed in BL21 (DE3) cells also harboring pEvol-MmPylRS AF [101]. The over-night culture is grown in LB with 30 µg/mL kanamycin and 30 µg/mL chloramphenicol. TB medium with 30 µg/mL kanamycin and 10 µg/mL chloramphenicol is inoculated to an OD_{600} of 0.05. Cells are grown at 37°C until an OD_{600} of 0.8 is reached. The temperature is shifted to 30°C and 0.1% L-arabinose and 1 mM SCO-L-lysine (SC-8001, Sirius Fine Chemicals SiChem) are added. The UAA is prepared freshly as a 100 mM stock solution in 0.2 M NaOH, 15% DMSO and diluted 1:4 in 1 M HEPES pH 7.0 prior to addition. After 30 min induction is started by addition of 1 mM IPTG and allowed to proceed for 3 h at 30°C.

B.2.3. p23

p23 (Sba1 in yeast, UniProtKB ID P28707) is used as wild-type protein.

The wt construct is contained in a pET28 vector and expressed from BL21 RIPL cells with a cleavable N-terminal His-SUMO tag. LB medium with 50 µg/mL kanamycin is inoculated 1:100 with an over-night culture and induced at an OD_{600} of 0.4 with 1 mM IPTG for 3.5 h. Cells are harvested by centrifugation, washed with PBS and pelleted again. The cell pellet is frozen in liquid nitrogen and stored at -20°C until purification.

After re-suspending in 50 mM sodium phosphate pH 8.0, 300 mM NaCl, 20 mM imidazole, cells are lysed in a Cell Disruptor (Constant Systems) at 1.6 kbar. Cell debris is pelleted by centrifugation at $17'000 \times g$ at 4°C for 30 min. After filtration (Filtropur S 0.45, Sarstedt), the cell lysate is applied to a 5 mL HisTrap HP (GE Healthcare) and eluted by a linear gradient from 20 to 500 mM imidazole in 50 mM sodium phosphate, 300 mM NaCl pH 8.0 at 8°C. Protein-containing fractions are pooled and dialyzed against 600 mL of the 20 mM imidazole buffer overnight at 8°C in the presence of 1/100 equivalent SENP protease to cleave the His-tag. The solution is again applied to the HisTrap column and the flow-through is collected and diluted 6× with ddH_2O to decrease the ionic strength. Subsequently, the solution is applied to a HiTrap Q HP 5 mL (GE Healthcare) and the protein is eluted with a linear gradient from 50 mM to 1 M NaCl in 40 mM HEPES pH 7.5. p23 containing fractions are pooled, concentrated with a centrifugal filter, snap-frozen in liquid nitrogen and stored at -80°C. Sample purity is checked by SDS-PAGE.

B.2.4. Δ131Δ

Δ131Δ is a 131 amino acid long fragment of the Staphylococcal nuclease (UniProtKB ID P00644) that comprises residues 1–3 and 13–140 of the full-length nuclease (149 residue). Wild-type Δ131Δ and cysteine mutants at positions K16 or K16/L137 (termed "C_2") are used.

Δ131Δ is contained in a pET28 vector and expressed from BL21 Codon plus RIL cells. Purification is done from inclusion bodies, following a protocol from the Agard lab. LB medium with 50 µg/mL kanamycin is inoculated 1:100 with an over-night culture and induced at an OD_{600} of 0.6 with 1 mM IPTG for 3 h. Cells are pelleted (15 min, 4°C, 4'600 rpm) washed with PBS pH 6.7, pelleted again and stored at -20°C.

In the following, volumes are given for a pellet from 200 mL expression. The pellet is re-suspend in 20 mL extraction buffer 1 (EB1; 25 mM TRIS, 2.5 mM EDTA, 6 M urea, pH 8.0) and rocked 10 min in the cold room. Inclusion bodies are pelleted by centrifugation (8'000 rpm, 15 min, 4°C). The inclusion bodies are dissolved in 10 mL EB2 (EB1 + 400 mM NaCl). The solution is centrifuged at 12'000 rpm, 20 min, 4°C and the supernatant is kept. 10 mL ice-cold EtOH absolute is added and incubated 1 h at -20°C to precipitate nucleic acids. The solution is centrifuged at 17'000 rpm, 20 min, 4°C, and the supernatant is added to 20 mL ice-cold EtOH absolute to precipitate Δ131Δ. Incubate 2 h (or over night) at -20°C. The solution is centrifuged at 17'000 rpm, 20 min, 4°C and the pellet is dried and re-suspended in 10 mL EB1 (+ 5 mM DTT when a cysteine mutant is purified). The protein is applied on a HiTrap SP HP 5 mL (GE Healthcare) and washed with EB1.

In the case of the wt Δ131Δ, the column is washed with refolding buffer 1 (RB1; 25 mM TRIS, 25 mM KCl, 5 mM $MgCl_2$, pH 7.5) and protein is eluted with a gradient from 0–100% RB2 (25 mM TRIS, 500 mM KCl, 5 mM $MgCl_2$, pH 7.5). Finally, wt Δ131Δ is dialyzed against H buffer at 8°C.

In the case of cysteine mutants, the protein unfortunately binds strongly to the ion exchange column. Therefore, the column is washed with ddH_2O and protein is eluted with a gradient from 0–100% 1 M NaOH. The pH has to be quickly adjust by addition of 50 mM TRIS pH 8 from a 10× stock. 5 mM DTT are added and Δ131Δ is dialyzed against H buffer at 8°C.

B.2.5. SENP

SENP is a protease which specifically cuts after a SUMO tag. The used construct is the protease domain of human Senp2 (UniProtKB ID Q9HC62; aa 396–560) fused to a His-Tag.

The protease was expressed in LB (without further antibiotics added) for 3 h at 37°C after induction with 1 mM IPTG. Cell disruption and purification with a HisTrap HP column is done as described for Hsp90. The protein solution is then applied immediately to a HiLoad 16/600 Superdex200 and eluted with 40 mM HEPES, 200 mM KCl pH 7.5, as the protein tends to precipitate at high concentrations of imidazole.

B.3. Biotin Labeling of Hsp90

The Δ131Δ smFRET data was recorded with Hsp90 that was *in vitro* biotinylated (indicated by “NHS-biotin”). Therefore, Hsp90 Q385C labeled with Atto647N (approx. 20 µM) is incubated with 2.5 mM AMP-PNP for 30 min at RT in H buffer. Then, NHS-PEG-biotin from a 3 mM stock in DMSO is added in 2× excess for 1 h at RT. Free NHS-PEG-biotin is removed by buffer exchange to H buffer with an Amicon Ultra 0.5 mL centrifugal filter (50 kDa MWCO, Merck Millipore).

B.4. Fluorescence Labeling

Fluorescence labels are attached to engineered cysteine residues via maleimide or copper-free click chemistry. The dyes (Atto488, Atto550 or Atto647N) are from ATTO-TEC.

B.4.1. Labeling of Hsp90

Typically, approx. 50 µL of a 50 µM Hsp90 solution are reduced for 30 min at RT with 5–10 mM TCEP, added from a pH-adjusted stock solution. Buffer is exchanged to 1× PBS, pH 6.7 using an Amicon Ultra 0.5 mL centrifugal filter (50 kDa MWCO) and an appropriate dilution factor. The sample should be in a concentration range of 30–70 µM after the last centrifugation step. Maleimide derivatives of the dyes are added from a millimolar stock solution in DMSO in 1.2–1.5× excess and allowed to react for 60 min at RT in the dark. Free dye is removed using PD MiniTrap G-25 columns (GE Healthcare) with the spin protocol. In short, prepare the column by removing the caps, pouring off the storage buffer and removing the top filter, washing with a total of 8 mL H buffer in gravity flow, adding 2 mL of H buffer and centrifuging 2 min at 1000 × g and 4°C. Apply the labeling reaction, diluted to 200 µL with H buffer, and centrifuge for 2 min at 1000 × g and 4°C. Remove potential aggregates by centrifugation (4°C, 14'000 rpm, >30 min). Aliquots are snap-frozen in liquid nitrogen and stored at -80°C.

B.4.2. Labeling of Aha1 S85SCO

Buffer is exchanged to PBS pH 6.7 with an Amicon Ultra 0.5 mL centrifugal filter (10 kDa MWCO). Atto647N-azide from a millimolar stock solution in DMSO is added in 5× excess and allowed to react over night in a cold room.

Free label is removed by extensive dialysis against 20 mM HEPES, 75 mM KCl, pH 7.5 with ready-to-use dialysis units (12–14 kDa MWCO, ZelluTrans/Roth Mini Dialyzer).

B.4.3. Labeling of Δ131Δ

500 µL of an approx. 25 µM solution of Δ131Δ K16C is incubated with 5 mM TCEP and 3 M urea (added from solid) for 1 h at RT. Then, the buffer is exchanged to 10 mM potassium phosphate (~3:2 mix of KH_2PO_4/K_2HPO_4), 5 mM $MgCl_2$, 3 M urea, pH 6.7 with an Amicon Ultra 0.5 mL centrifugal filter (3 kDa MWCO). 1.2× excess of maleimide dye is added and incubated for 2 h at RT. Free dye is removed by dialysis against at least 0.5 L H buffer using dialysis units (3.5 kDa MWCO, ZelluTrans/Roth Mini Dialyzer) in a cold room for two days.

For the stochastic labeling of the Δ131Δ K16C/L137C variant (data in Fig. 4.10), the protein was incubated with 5 mM TCEP and 3 M urea (added from solid) for 30 min at RT. Subsequently, the buffer is exchanged to 10 mM potassium phosphate, 5 mM $MgCl_2$, 3 M urea, pH 6.7 ("Δ131Δ label buffer") with an Amicon Ultra 0.5 mL centrifugal filter (3 kDa MWCO). Maleimide derivatives of Atto550 and Atto647N are added simultaneously at 1.5× excess over the Δ131Δ concentration and allowed to react for 2 h at RT in the dark. Free label is removed by buffer exchange to Δ131Δ label buffer with the same Amicon Ultra centrifugal filter and five buffer exchange steps. Then, buffer is changed to H buffer in three steps.

B.5. Fluorescence Anisotropy

For all measurements, the G-factor (the correction for different detection efficiencies for vertically and horizontally polarized light) is determined prior to the actual experiment. For this, the labeled species is used in approx. the same concentration as for the measurement.

Steady-state fluorescence anisotropy data was recorded with a Jasco FP-8500 fluorescence spectrometer (Munich) and the polarization filters were mounted manually. 500 nM Δ131Δ-Atto647N were used. Excitation bandwidth was set to either 2.5 nm in combination with a response of 4 s (for data in Fig. 4.7) or 5 nm in combination with a response of 0.5 s (for data in Fig. 4.8). Emission bandwidth was set to 5 nm and sensitivity to "high". Excitation and emission wavelength were set to 630 and 660 nm, respectively. Temperature is indicated in the Figure caption and was either RT or 25°C with a Peltier cuvette holder.

Steady-state fluorescence anisotropy data was also recorded with a Horiba Fluoro-Max 4 fluorescence spectrometer (Freiburg). The G-factor for this device is approx. 0.63 for Atto550 and 0.49 for Atto647N.
Aha1 85SCO-Atto550 (500 nM; data in Fig. 4.3) was measured with excitation at 550 nm (3 nm bandwidth), emission 575 nm (5 nm bandwidth), 1 s integration time and a time increment of 6 s at 30°C in a Peltier 4× cuvette holder.
Aha1 85SCO-Atto647N (200 nM; data in Fig. 4.5) was measured with excitation at 648 nm (3 nm bandwidth), emission 660 nm (3 nm bandwidth), 2 s integration time and a time increment of 10 s at 25°C in a Peltier 4× cuvette holder.
Atto647N-labeled AMP-PNP (500 nM; data in Fig. 4.14) was measured with excitation at 648 nm (1 nm bandwidth), emission 660 nm (3 nm bandwidth), 0.5 s integration time and a time increment of 5 s at 25°C in a Peltier 4× cuvette holder.

B.6. Fluorescence Spectra

Fluorescence spectra (of samples labeled with Atto550 and Atto647N) were recorded with a Jasco FP-8500 fluorescence spectrometer (Munich). The excitation wavelength was set to 510 nm, excitation and emission bandwidth were set to 2.5 nm and the scan speed was 200 nm/min. The response is set to 1 s and sensitivity to "high". Spectra were recorded in the range from 550–750 nm with a data interval of 1 nm.

The spectra is corrected for the wavelength dependent detection efficiency, by multiplication with a correction file (obtained by measurement of a calibrated light source). If applicable, the direct excitation of the acceptor dye of the FRET pair is subtracted (by measurement of an acceptor-only sample). The spectra are then normalized to an area of unity and scaled by a factor of 1000 to give a convenient axis range.

B.7. ATPase Assay

ATPase activity was determined with a regenerating ATPase assay [135, 45]. ATP hydrolysis is coupled to oxidation of nicotinamide adenine dinucleotide (NADH) by pyruvate kinase (PK) and lactate dehydrogenase (LDH) – via the transfer of a phosphate group from phosphoenolpyruvate (PEP) to ADP. The consumption of NADH can be measured by the change in absorbance at 340 nm. The final concentrations in the assay are: 0.2 mM NADH, 2 mM PEP, 2 U/mL PK, 10 U/mL LDH, 2 mM ATP and 2 µM Hsp90 in H buffer.

A premix of all components except ATP and Hsp90 is prepared and stored at -80°C. ATP is added and the absorbance is followed until a stable baseline is reached (indicating that residual ADP is regenerated). Then Hsp90 is added. After approx. 5–10 min, 1 µL of 2 mg/mL radicicol is added in order to specifically inhibit the ATPase of Hsp90. This allows to measure the ATPase background.

Absorbance time traces were recorded on a PerkinElmer Lambda25 spectrophotometer (wavelength 340 nm, slits 1 nm, UV lamp only, interval 1 sec, response 0.5 sec, water bath set to 37°C) or on a TIDAS S 500-1910 UV/NIR (scan range 251.2–380 nm, interpolate on, step 0.8 nm, integration time 10.6 ms, 10 accumulations, water bath set to

30.7°C).

B.8. Measurements on a Four-Color smFRET Setup

Main parts of the methods described in this section are published in Götz, Wortmann, Schmid & Hugel (2016) [35].

B.8.1. Construction of the Measurement Chamber

The sample is studied in a custom-built flow-chamber, which is a sandwich of:

- a thick (3 mm) quartz slide (Finkenbeiner) with drilled holes to attach flexible tubes,
- a thin (40 µm) sealing film (Tegaderm 1626W, 3M) sprayed with Photomount (3M) on the non-adhesive side,
- a high precision cover slip (LH26.1, Carl Roth).

A laser cutter (Speedy 100, Trotec) is used to cut the outline of the flow-chamber from Tegaderm film (settings: power 30, speed 3, frequency Auto Hz, passes 1, blow off, correction 20, offset 0).

The Tegaderm film is placed on the quartz slide with the spray adhesive facing down and covered with a normal microscopy slide to protect the quartz slide, heated to approx. 80°C and tightly pressed together with two cap screws for 1 min. The quartz slide is allowed to cool down a bit, the paper support of the Tegaderm film is removed and the cover slip is placed on top, followed by another microscopy slide. The sandwich is again heated to approx. 80°C, pressed together for 1 min and allowed to cool down.

The flow-chamber is mounted in an aluminum prism-holder with glycerol (Immersol G, Carl Zeiss) between prism and quartz slide. Flexible PTFE tubing (Bola S1810-08, Bohlender) is fit to the flow chamber with hollow setscrews and a thicker, more flexible tubing (Tygon S3 E-3603, neoLab).

A syringe pump (PHD22/2000, Harvard Apparatus) allows exchanging of buffer and immersion oil with low auto-fluorescence is used between flow-chamber and objective (Immoil-F30CC, Olympus).

Specific immobilization of the protein of interest on the quartz slide is achieved by biotin-Neutravidin linkage. Both, the slide surface and the protein are biotinylated and cross-linked by Neutravidin (250 µg/mL in H buffer; 31000, Thermo Fisher Scientific).

B.8.2. Surface Passivation and Functionalization

The quartz slide is passivated with a layer of methoxy-/biotin-PEG (5 kDa methoxy-PEG-NHS, 12 5000-35; 3 kDa biotin-PEG-NHS, 13 3000-25-35; Rapp Biopolymere).

Cleaning

1. Sonicate quartz slides 3× in 2% Hellmanex (Hellma Analytics) solution for 10 min and wash 5× with ultra-pure water in between and afterwards.
2. Incubate slides for 2 h in Piranha solution (3:1 vol/vol H_2SO_4:H_2O_2) at 60°C.
3. Rinse slides with ultra-pure water.
4. Repeat step 1.
5. Incubate slides for 2 h in RCA (5:1:1 vol/vol/vol H_2O:H_2O_2:NH_4OH) at 60°C.
6. Rinse slides 5× with ultra-pure water.

Functionalization

1. Incubate the slides 15 min in acetone.
2. Incubate slides with a 1:200 dilution of Vectabond (Vector Laboratories) in acetone for 5–10 min.
3. Wash slides with ultra-pure water in a large beaker.
4. Dissolve 3 mg biotin-PEG and 80 mg methoxy-PEG in 600 µL 100 mM $NaHCO_3$ (pH does not have not be adjusted).
5. Add a droplet of 60 µL of the PEG solution on each slide, place a clean cover slip on top, and incubate overnight at 8°C in humid atmosphere.
6. Wash slides with ultra-pure water in a large beaker, dry them with a stream of nitrogen and store them in a dry and light-protected place.

B.8.3. Measurement

Pre-bleaching of the measurement chamber, camera and other acquisition settings are detailed in the main text in Section 3.2.2 on page 24.

B.8.4. Post-Measurement Procedures

Intensity Map

In the case of two-color measurements, an intensity map is used to correct for non-uniform illumination. On a prism-type TIRF microscope, flush a sample with approx. 1 nM into the flow-chamber at the end of the measurement. Record a movie with the same settings as used for single-molecule recording while driving through the chamber. Slight defocusing helps to reduce the influence of single bright spots on the final result. A second movie is recorded with the lasers turned off to record the dark current of the chip and residual stray light that strikes the camera.

All frames in the corresponding channels of the movies are summed, an average filter of 5 × 5 is applied and the dark current is subtracted. Finally, the intensity map is normalized to the maximal intensity.

Channel Registration

A precise mapping of the coordinates of one channel to all other channels is necessary to get the fluorescence intensities of all dyes attached to one protein in a multi-color FRET experiment. This is achieved by a calibration with fluorescent beads (FluoSpheres amine-modified, 0.2 µm, yellow-green, F8764, Thermo Fisher Scientific) that show fluorescence emission in the spectral range of all four detection channels of the setup upon excitation with the blue laser. At the end of each day of measurement, a 1:1000 dilution of the beads in ddH_2O is flushed into the chamber and a movie is recorded while driving stepwise through the chamber. Neutral density filters are placed in the blue (OD 1) and orange (OD 0.8) detection to match the recorded intensity between the different channels. The EM gain of the camera for blue/green is lowered to 5 and the one of the camera for orange/red is lowered to 50. Acquisition mode is set to Frame Transfer.

Bead positions are detected in the calibration movie by searching for the brightest spots and the central position is determined from a Gaussian fit to the intensity profile. The bead positions in the different channels are linked by image registration of the recorded calibration movies (kudos to Markus Jahn for writing the initial code). A distance cut-off is applied to exclude incorrectly assigned beads. The coordinates of beads that are found in all four channels are saved and the mapping offset in x- and y-direction is each fitted with a 2D polynomial of degree three.

B.8.5. Extraction of Fluorescence Intensity Time Traces

All data analysis is done with in-house written scripts in Igor Pro 6 (WaveMetrics).

The raw data from the EMCCD cameras (i.e. frames of 512 × 512 pixels of the fluorescence intensities in 16-bit gray scale) are stored as TIFF stacks. The movies are automatically split into the respective detection channels when loaded according to predefined settings.

Individual molecules are identified in each movie by searching for the brightest spots in the sum of 5 consecutive frames of a certain channel. The central position of the spot is calculated for all channels using the channel mapping. For each channel the intensity traces are typically obtained by a 5 × 5 binning of the pixels around the central coordinates in each frame. The binning corresponds to an area of approximately 800 × 800 nm for the given magnification of the setup.

Intensity traces are automatically corrected for an offset originating from the dark current of the EMCCD and background fluorescence. This is done by automatically subtracting a background time trace that is the mean of the 200 darkest pixels in each channel.

Two-Color Measurements

The trace selection criteria for a two-color experiment are the presence of both dyes and no photo-physical artifacts such as blinking. This means flat plateaus in all three detection channels (donor and acceptor fluorescence after donor excitation and acceptor fluorescence after acceptor excitation), as well as single bleaching steps.

A local background is subtracted for each trace by selecting a region where both dyes are already bleached. Then the region where both dyes are present ("FRET range") and where only one of the dyes is still present (donor only/acceptor only) are selected separately.

A stoichiometry (S) versus FRET efficiency (E) histogram is compiled from the complete data set and the intensity map is applied to correct the non-uniform illumination. First, the donor only/acceptor only data is used to determine the correction factors for leakage of donor fluorescence into the acceptor channel (α) and direct acceptor excitation by the donor excitation laser (δ). Then, α and δ are used to correct the "FRET range" data and the correction factors to normalize the excitation intensities and absorption cross-sections of acceptor and donor (β) and to normalize fluorescence quantum yields and detection efficiencies of acceptor and donor (γ) are determined. This procedure can be iterated, if β and γ are far from 1.

The correction factors tend to get over-estimated if the data set is small. In this case it is better to use a default set of these values. For the Atto550/Atto647N dye pair and the described four-color setup (see Section 3.1) one finds typically: $\alpha = 0.05$–0.08, $\delta = 0.04$–0.07, $\gamma = 1.0$–1.3 and the excitation intensities should be adjusted to yield $\beta \approx 1$.

Three-Color Measurements

The selection criteria for a three-color experiment and the correction for local background are given in Section 3.2.3 on page 25.

The calculation of the partial fluorescence trace from the "FRET" region of the intensity traces is detailed in Section 3.2.4. The predetermined correction factors for apparent leakage lk and apparent gamma ag for the four detection channels of Atto488, Atto550, Atto594 and Atto647N ("blue", "green", "orange" and "red") are $lk^{blue}_{green} = 0.12$, $lk^{blue}_{orange} = 0.03$, $lk^{blue}_{red} = 0.01$, $lk^{green}_{orange} = 0.26$, $lk^{green}_{red} = 0.08$, $lk^{orange}_{red} = 0.46$, $ag_{blue} = 0.68$, $ag_{green} = 1.16$, $ag_{orange} = 2.18$ and $ag_{red} := 1$.

The calibration samples are high-FRET dsDNA samples for each dye in combination with the acceptor having the longest excitation wavelength (Atto488-Atto647N, Atto550- Atto647N, Atto594-Atto647N). The Atto647N strand additionally carries a biotin. The sequence of the DNA is:

```
5'-GAG CTG AAA GTG TCG AGT TTG TTT GAG TGT TTG TCT GG-3'
3'-CTC GAC TTT CAC AGC TCA AAC AAA CTC ACA AAC AGA CC-5'-biotin
```

with the thymidine highlighted in red carrying the acceptor dye (Atto647N) and the thymidine with the gray background the donor dye (Atto488, Atto550 or Atto594). Each calibration sample is attached to the surface via biotin-Neutravidin coupling in a separate experiment. Measurements are done in TNM buffer (5 mM Tris pH 7.5, 5 mM NaCl, 20 mM $MgCl_2$) and 2 mM Trolox. ALEX is used to exclude photo-physical artifacts such as acceptor blinking and the obtained intensity traces are corrected automatically and manually for background.

Determination of the correction factors for apparent leakage (lk) and apparent gamma (ag) is given in Section 3.2.4 on page 25.

List of Figures

Acronyms

ALEX alternating laser excitation

AMP-PNP* Atto647N-labeled AMP-PNP

AV accessible volume

BIC Bayesian information criterion

CI confidence interval

CL charged linker

CTD C-terminal domain

EM electron microscopy

FCS fluorescence correlation spectroscopy

FRET Förster resonance energy transfer

GR-LBD ligand binding domain of the glucocorticoid receptor

HMM hidden Markov model

HtpG high-temperature protein G

Hsp90 heat shock protein 90

LR likelihood ratio

MD middle domain

MLE maximum likelihood estimator

NTD N-terminal domain

PDF probability density function

PEG polyethylene glycol

SAXS small-angle X-ray scattering

SMACKS single-molecule analysis of complex kinetic sequences

smFRET single-molecule Förster resonance energy transfer

SN Staphylococcal nuclease

SNR signal-to-noise ratio

TIR total internal reflection

TIRF total internal reflection fluorescence

TPR tetratricopeptide repeat

Bibliography

[1] Aitken, C. E., Marshall, R. A., and Puglisi, J. D. “An oxygen scavenging system for improvement of dye stability in single-molecule fluorescence experiments”. *Biophysical Journal* 94 (2008), pp. 1826–1835. DOI: `10.1529/biophysj.107.117689`.

[2] Alberts, B. “The Cell as a Collection of Protein Machines. Preparing the Next Generation of Molecular Biologists”. *Cell* 92 (1998), pp. 291–294. DOI: `10.1016/S0092-8674(00)80922-8`.

[3] Alexandrescu, A. T. and Shortle, D. “Backbone Dynamics of a Highly Disordered 131 Residue Fragment of Staphylococcal Nuclease”. *Journal of Molecular Biology* 242 (1994), pp. 527–546. DOI: `10.1006/jmbi.1994.1598`.

[4] Alexandrescu, A. T., Abeygunawardana, C., and Shortle, D. “Structure and Dynamics of a Denatured 131-Residue Fragment of Staphylococcal Nuclease. A Heteronuclear NMR Study”. *Biochemistry* 33 (1994), pp. 1063–1072. DOI: `10.1021/bi00171a004`.

[5] Ali, M. M. U., Roe, S. M., Vaughan, C. K., Meyer, P., Panaretou, B., Piper, P. W., Prodromou, C., and Pearl, L. H. “Crystal structure of an Hsp90-nucleotide-p23/Sba1 closed chaperone complex”. *Nature* 440 (2006), pp. 1013–1017. DOI: `10.1038/nature04716`.

[6] Andrec, M., Levy, R. M., and Talaga, D. S. “Direct Determination of Kinetic Rates from Single-Molecule Photon Arrival Trajectories Using Hidden Markov Models”. *The Journal of Physical Chemistry A* 107 (2003), pp. 7454–7464. DOI: `10.1021/jp035514`.

[7] Anyika, M., McMullen, M., Forsberg, L. K., Dobrowsky, R. T., and Blagg, B. S. J. “Development of Noviomimetics as C-Terminal Hsp90 Inhibitors”. *ACS Medicinal Chemistry Letters* 7 (2016), pp. 67–71. DOI: `10.1021/acsmedchemlett.5b00331`.

[8] Bagshaw, C. R. “Kinetics. Single-Molecule Techniques”. *Encyclopedia of Biophysics*. Ed. by Roberts, G. C. K. Berlin, Heidelberg: Springer Berlin Heidelberg, 2013, pp. 1217–1223. DOI: `10.1007/978-3-642-16712-6_57`.

[9] Bauer, R. J., Bowman, B. F., and Kenyon, J. L. “Theory of the kinetic analysis of patch-clamp data”. *Biophysical Journal* 52 (1987), pp. 961–978. DOI: `10.1016/S0006-3495(87)83289-7`.

[10] Benke, S., Nettels, D., Hofmann, H., and Schuler, B. “Quantifying Kinetics from Time Series of Single-Molecule FRET Efficiency Histograms”. *Nanotechnology* (2017). DOI: `10.1088/1361-6528/aa5abd`.

[11] Blanchard, S. C., Kim, H. D., Gonzalez, R. L., Puglisi, J. D., and Chu, S. “tRNA dynamics on the ribosome during translation”. *Proceedings of the National Academy of Sciences of the United States of America* 101 (2004), pp. 12893–12898. DOI: `10.1073/pnas.0403884101`.

[12] Borkovich, K. A., Farrelly, F. W., Finkelstein, D. B., Taulien, J., and Lindquist, S. L. “hsp82 is an essential protein that is required in higher concentrations for growth of cells at higher temperatures”. *Molecular and Cellular Biology* 9 (1989), pp. 3919–3930. URL: `https://www.ncbi.nlm.nih.gov/pmc/articles/PMC362454/`.

[13] Bron, P., Giudice, E., Rolland, J.-P., Buey, R. M., Barbier, P., Díaz, J. F., Peyrot, V., Thomas, D., and Garnier, C. “Apo-Hsp90 coexists in two open conformational states in solution”. *Biology of the Cell* 100 (2008), pp. 413–425. DOI: `10.1042/BC20070149`.

[14] Bronson, J. E., Fei, J., Hofman, J. M., Gonzalez, R. L., and Wiggins, C. H. “Learning rates and states from biophysical time series: a Bayesian approach to model selection and single-molecule FRET data”. *Biophysical Journal* 97 (2009), pp. 3196–3205. DOI: `10.1016/j.bpj.2009.09.031`.

[15] Brunger, A. T., Strop, P., Vrljic, M., Chu, S., and Weninger, K. R. “Three-dimensional molecular modeling with single molecule FRET”. *Journal of Structural Biology* 173 (2011), pp. 497–505. DOI: `10.1016/j.jsb.2010.09.004`.

[16] Chen, B., Doucleff, M., Wemmer, D. E., Carlo, S. de, Huang, H. H., Nogales, E., Hoover, T. R., Kondrashkina, E., Guo, L., and Nixon, B. T. “ATP ground- and transition states of bacterial enhancer binding AAA+ ATPases support complex formation with their target protein, sigma54”. *Structure* 15 (2007), pp. 429–440. DOI: `10.1016/j.str.2007.02.007`.

[17] Chen, B., Zhong, D., and Monteiro, A. “Comparative genomics and evolution of the HSP90 family of genes across all kingdoms of organisms”. *BMC Genomics* 7 (2006), p. 156. DOI: `10.1186/1471-2164-7-156`.

[18] Cunningham, C. N., Krukenberg, K. A., and Agard, D. A. “Intra- and intermonomer interactions are required to synergistically facilitate ATP hydrolysis in Hsp90”. *Journal of Biological Chemistry* 283 (2008), pp. 21170–21178. DOI: `10.1074/jbc.M800046200`.

[19] Cunningham, C. N., Southworth, D. R., Krukenberg, K. A., and Agard, D. A. “The conserved arginine 380 of Hsp90 is not a catalytic residue, but stabilizes the closed conformation required for ATP hydrolysis”. *Protein Science* 21 (2012), pp. 1162–1171. DOI: `10.1002/pro.2103`.

[20] DeBoer, C., Meulman, P. A., Wnuk, R. J., and Peterson, D. H. “Geldanamycin, a new antibiotic”. *The Journal of Antibiotics* 23 (1970), pp. 442–447. DOI: `10.7164/antibiotics.23.442`.

[21] Delmotte, P. and Delmotte-Plaquee, J. “A New Antifungal Substance of Fungal Origin”. *Nature* 171 (1953), p. 344. DOI: `10.1038/171344a0`.

[22] Dezwaan, D. C. and Freeman, B. C. “HSP90: the Rosetta stone for cellular protein dynamics?” *Cell Cycle* 7 (2008), pp. 1006–1012. DOI: `10.4161/cc.7.8.5723`.

[23] Donnelly, A. and Blagg, B. S. J. “Novobiocin and Additional Inhibitors of the Hsp90 C-Terminal Nucleotide-binding Pocket”. *Current Medicinal Chemistry* 15 (2008), pp. 2702–2717.

[24] Falsone, S. F., Kungl, A. J., Rek, A., Cappai, R., and Zangger, K. “The Molecular Chaperone Hsp90 Modulates Intermediate Steps of Amyloid Assembly of the Parkinson-related Protein α-Synuclein”. *Journal of Biological Chemistry* 284 (2009), pp. 31190–31199. DOI: `10.1074/jbc.M109.057240`.

[25] Fink, G. A. *Markov Models for Pattern Recognition.* London: Springer London, 2014. DOI: `10.1007/978-1-4471-6308-4`.

[26] Förster, T. “Zwischenmolekulare Energiewanderung und Fluoreszenz”. *Annalen der Physik* 437 (1948), pp. 55–75. DOI: `10.1002/andp.19484370105`.

[27] Frauenfelder, H., Sligar, S. G., and Wolynes, P. G. “The energy landscapes and motions of proteins”. *Science* 254 (1991), pp. 1598–1603. DOI: `10.1126/science.1749933`.

[28] Gasteiger, E., Hoogland, C., Gattiker, A., Duvaud, S., Wilkins, M. R., Appel, R. D., and Bairoch, A. “Protein Identification and Analysis Tools on the ExPASy Server”. *The Proteomics Protocols Handbook.* Ed. by Walker, J. M. Methods in Molecular Biology. Totowa, NJ: Humana Press Inc, 2005, pp. 571–607. DOI: `10.1385/1-59259-890-0:571`.

[29] Gavin, A.-C., Bösche, M., Krause, R., Grandi, P., Marzioch, M., Bauer, A., Schultz, J., Rick, J. M., Michon, A.-M., Cruciat, C.-M., Remor, M., Höfert, C., Schelder, M., et al. “Functional organization of the yeast proteome by systematic analysis of protein complexes”. *Nature* 415 (2002), pp. 141–147. DOI: `10.1038/415141a`.

[30] Genest, O., Reidy, M., Street, T. O., Hoskins, J. R., Camberg, J. L., Agard, D. A., Masison, D. C., and Wickner, S. “Uncovering a region of heat shock protein 90 important for client binding in E. coli and chaperone function in yeast”. *Molecular Cell* 49 (2013), pp. 464–473. DOI: `10.1016/j.molcel.2012.11.017`.

[31] Giudici, P., Ryden, T., and Vandekerkhove, P. “Likelihood-Ratio Tests for Hidden Markov Models”. *Biometrics* 56 (2000), pp. 742–747. DOI: `10.1111/j.0006-341X.2000.00742.x`.

[32] Gopich, I. and Szabo, A. “Theory of photon statistics in single-molecule Förster resonance energy transfer”. *The Journal of Chemical Physics* 122 (2005), p. 14707. DOI: `10.1063/1.1812746`.

[33] Gopich, I. V. and Szabo, A. “Single-molecule FRET with diffusion and conformational dynamics”. *The Journal of Physical Chemistry B* 111 (2007), pp. 12925–12932. DOI: `10.1021/jp075255e`.

[34] Gopich, I. V. and Szabo, A. "Decoding the pattern of photon colors in single-molecule FRET". *The Journal of Physical Chemistry B* 113 (2009), pp. 10965–10973. DOI: `10.1021/jp903671p`.

[35] Götz, M., Wortmann, P., Schmid, S., and Hugel, T. "A Multicolor Single-Molecule FRET Approach to Study Protein Dynamics and Interactions Simultaneously". *Methods in Enzymology* 581 (2016), pp. 487–516. DOI: `10.1016/bs.mie.2016.08.024`.

[36] Graf, C., Lee, C.-T., Meier-Andrejszki, L. E., Nguyen, M. T. N., and Mayer, M. P. "Differences in conformational dynamics within the Hsp90 chaperone family reveal mechanistic insights". *Frontiers in Molecular Biosciences* 1 (2014), p. 4. DOI: `10.3389/fmolb.2014.00004`.

[37] Greenfeld, M., Pavlichin, D. S., Mabuchi, H., and Herschlag, D. "Single Molecule Analysis Research Tool (SMART): an integrated approach for analyzing single molecule data". *PloS ONE* 7 (2012), e30024. DOI: `10.1371/journal.pone.0030024`.

[38] Grinstead, C. M. and Snell, J. L. *Introduction to Probability.* Providence, Rhode Island, USA: American Mathematical Society, 1998. URL: `http://www.dartmouth.edu/~chance/teaching_aids/books_articles/probability_book/pdf.html`.

[39] Ha, T., Enderle, T., Ogletree, D. F., Chemla, D. S., Selvin, P. R., and Weiss, S. "Probing the interaction between two single molecules: fluorescence resonance energy transfer between a single donor and a single acceptor". *Proceedings of the National Academy of Sciences of the United States of America* 93 (1996), pp. 6264–6268. URL: `http://www.pnas.org/content/93/13/6264`.

[40] Ha, T. "Single-molecule methods leap ahead". *Nature Methods* 11 (2014), pp. 1015–1018. DOI: `10.1038/nmeth.3107`.

[41] Halpin, J. C., Huang, B., Sun, M., and Street, T. O. "Crowding Activates Heat Shock Protein 90". *Journal of Biological Chemistry* 291 (2016), pp. 6447–6455. DOI: `10.1074/jbc.M115.702928`.

[42] Hellenkamp, B. "Dynamic structure of a multi-domain protein. uncovered using self-consistent FRET networks and time-correlated distance distributions". Fakultät für Physik. Dissertation. München: Technische Universität München, 2016. URL: `https://mediatum.ub.tum.de/doc/1289875/1289875.pdf`.

[43] Hellenkamp, B., Wortmann, P., Kandzia, F., Zacharias, M., and Hugel, T. "Multidomain structure and correlated dynamics determined by self-consistent FRET networks". *Nature Methods* 14 (2017), pp. 174–180. DOI: `10.1038/nmeth.4081`.

[44] Henzler-Wildman, K. and Kern, D. "Dynamic personalities of proteins". *Nature* 450 (2007), pp. 964–972. DOI: `10.1038/nature06522`.

[45] Hessling, M., Richter, K., and Buchner, J. "Dissection of the ATP-induced conformational cycle of the molecular chaperone Hsp90". *Nature Structural & Molecular Biology* 16 (2009), pp. 287–293. DOI: `10.1038/nsmb.1565`.

[46] Hill, T. L. *Free Energy Transduction and Biochemical Cycle Kinetics*. Courier Corporation, 2004.

[47] Hohng, S., Joo, C., and Ha, T. “Single-molecule three-color FRET”. *Biophysical Journal* 87 (2004), pp. 1328–1337. DOI: `10.1529/biophysj.104.043935`.

[48] Horn, R. and Lange, K. “Estimating kinetic constants from single channel data”. *Biophysical Journal* 43 (1983), pp. 207–223. DOI: `10.1016/S0006-3495(83)84341-0`.

[49] Horvat, N. K., Armstrong, H., Lee, B. L., Mercier, R., Wolmarans, A., Knowles, J., Spyracopoulos, L., and LaPointe, P. “A mutation in the catalytic loop of Hsp90 specifically impairs ATPase stimulation by Aha1p, but not Hch1p”. *Journal of Molecular Biology* 426 (2014), pp. 2379–2392. DOI: `10.1016/j.jmb.2014.04.002`.

[50] Howard, J. *Mechanics of Motor Proteins and the Cytoskeleton*. Sunderland, Massachusetts: Sinauer Associates, 2001. XVI, 367 S.

[51] Immormino, R. M., Kang, Y., Chiosis, G., and Gewirth, D. T. “Structural and quantum chemical studies of 8-aryl-sulfanyl adenine class Hsp90 inhibitors”. *Journal of Medicinal Chemistry* 49 (2006), pp. 4953–4960. DOI: `10.1021/jm060297x`.

[52] Jabłoński, A. “Über den Mechanismus der Photolumineszenz von Farbstoffphosphoren”. *Zeitschrift für Physik* 94 (1935), pp. 38–46. DOI: `10.1007/BF01330795`.

[53] Jaffe, H. H. and Miller, A. L. “The fates of electronic excitation energy”. *Journal of Chemical Education* 43 (1966), p. 469. DOI: `10.1021/ed043p469`.

[54] Jahn, M., Rehn, A., Pelz, B., Hellenkamp, B., Richter, K., Rief, M., Buchner, J., and Hugel, T. “The charged linker of the molecular chaperone Hsp90 modulates domain contacts and biological function”. *Proceedings of the National Academy of Sciences of the United States of America* 111 (2014), pp. 17881–17886. DOI: `10.1073/pnas.1414073111`.

[55] Jakob, U., Lilie, H., Meyer, I., and Buchner, J. “Transient Interaction of Hsp90 with Early Unfolding Intermediates of Citrate Synthase. Implications for Heat Shock in vivo”. *Journal of Biological Chemistry* 270 (1995), pp. 7288–7294. DOI: `10.1074/jbc.270.13.7288`.

[56] Jakob, U. “HSP90 – news from the front”. *Frontiers in Bioscience* 1 (1996), pp. d309–17.

[57] Johnson, J. L., Beito, T. G., Krco, C. J., and Toft, D. O. “Characterization of a novel 23-kilodalton protein of unactive progesterone receptor complexes”. *Molecular and Cellular Biology* 14 (1994), pp. 1956–1963. DOI: `10.1128/MCB.14.3.1956`.

[58] Kalinin, S., Peulen, T., Sindbert, S., Rothwell, P. J., Berger, S., Restle, T., Goody, R. S., Gohlke, H., and Seidel, C. A. M. “A toolkit and benchmark study for FRET-restrained high-precision structural modeling”. *Nature Methods* 9 (2012), pp. 1218–1225. DOI: `10.1038/nmeth.2222`.

[59] Kapanidis, A. N., Lee, N. K., Laurence, T. A., Doose, S., Margeat, E., and Weiss, S. “Fluorescence-aided molecule sorting: analysis of structure and interactions by alternating-laser excitation of single molecules”. *Proceedings of the National Academy of Sciences of the United States of America* 101 (2004), pp. 8936–8941. DOI: `10.1073/pnas.0401690101`.

[60] Kapanidis, A. N., Laurence, T. A., Lee, N. K., Margeat, E., Kong, X., and Weiss, S. “Alternating-laser excitation of single molecules”. *Accounts of Chemical Research* 38 (2005), pp. 523–533. DOI: `10.1021/ar0401348`.

[61] Karagöz, G. E., Duarte, A. M. S., Ippel, H., Uetrecht, C., Sinnige, T., van Rosmalen, M., Hausmann, J., Heck, A. J. R., Boelens, R., and Rüdiger, S. G. D. “N-terminal domain of human Hsp90 triggers binding to the cochaperone p23”. *Proceedings of the National Academy of Sciences of the United States of America* 108 (2011), pp. 580–585. DOI: `10.1073/pnas.1011867108`.

[62] Karagöz, G. E. and Rüdiger, S. G. D. “Hsp90 interaction with clients”. *Trends in Biochemical Sciences* 40 (2015), pp. 117–125. DOI: `10.1016/j.tibs.2014.12.002`.

[63] Kasha, M. “Characterization of electronic transitions in complex molecules”. *Discussions of the Faraday society* 9 (1950), pp. 14–19.

[64] Kelly, D., Dillingham, M., Hudson, A., and Wiesner, K. “A new method for inferring hidden markov models from noisy time sequences”. *PloS ONE* 7 (2012), e29703. DOI: `10.1371/journal.pone.0029703`.

[65] Khandelwal, A., Crowley, V. M., and Blagg, B. S. J. “Natural Product Inspired N-Terminal Hsp90 Inhibitors: From Bench to Bedside?” *Medicinal Research Reviews* 36 (2016), pp. 92–118. DOI: `10.1002/med.21351`.

[66] Kleckner, I. R. and Foster, M. P. “An introduction to NMR-based approaches for measuring protein dynamics”. *Biochimica et Biophysica Acta* 1814 (2011), pp. 942–968. DOI: `10.1016/j.bbapap.2010.10.012`.

[67] Knox, R. S. and van Amerongen, H. “Refractive Index Dependence of the Förster Resonance Excitation Transfer Rate”. *The Journal of Physical Chemistry B* 106 (2002), pp. 5289–5293. DOI: `10.1021/jp013927`.

[68] Koulov, A. V., LaPointe, P., Lu, B., Razvi, A., Coppinger, J., Dong, M.-Q., Matteson, J., Laister, R., Arrowsmith, C., Yates, J. R., and Balch, W. E. “Biological and structural basis for Aha1 regulation of Hsp90 ATPase activity in maintaining proteostasis in the human disease cystic fibrosis”. *Molecular Biology of the Cell* 21 (2010), pp. 871–884. DOI: `10.1091/mbc.E09-12-1017`.

[69] Lai, B.-T., Chin, N. W., Stanek, A. E., Keh, W., and Lanks, K. W. “Quantitation and intracellular localization of the 85K heat shock protein by using monoclonal and polyclonal antibodies”. *Molecular and Cellular Biology* 4 (1984), pp. 2802–2810. DOI: `10.1128/MCB.4.12.2802`.

[70] Lakowicz, J. R. *Principles of fluorescence spectroscopy.* 3. ed., corr. 4. print. New York NY: Springer, 2010. XXVI, 954 S.

[71] Lee, J., Lee, S., Ragunathan, K., Joo, C., Ha, T., and Hohng, S. "Single-molecule four-color FRET". *Angewandte Chemie (International ed. in English)* 49 (2010), pp. 9922–9925. DOI: `10.1002/anie.201005402`.

[72] Lee, N. K., Kapanidis, A. N., Wang, Y., Michalet, X., Mukhopadhyay, J., Ebright, R. H., and Weiss, S. "Accurate FRET measurements within single diffusing biomolecules using alternating-laser excitation". *Biophysical Journal* 88 (2005), pp. 2939–2953. DOI: `10.1529/biophysj.104.054114`.

[73] Li, J., Richter, K., Reinstein, J., and Buchner, J. "Integration of the accelerator Aha1 in the Hsp90 co-chaperone cycle". *Nature Structural & Molecular Biology* 20 (2013), pp. 326–331. DOI: `10.1038/nsmb.2502`.

[74] Liu, Y., Park, J., Dahmen, K. A., Chemla, Y. R., and Ha, T. "A comparative study of multivariate and univariate hidden Markov modelings in time-binned single-molecule FRET data analysis". *The Journal of Physical Chemistry B* 114 (2010), pp. 5386–5403. DOI: `10.1021/jp9057669`.

[75] Loll, P. J. and Lattman, E. E. "The crystal structure of the ternary complex of staphylococcal nuclease, Ca2+, and the inhibitor pdTp, refined at 1.65 A". *Proteins* 5 (1989), pp. 183–201. DOI: `10.1002/prot.340050302`.

[76] Lorenz, O. R., Freiburger, L., Rutz, D. A., Krause, M., Zierer, B. K., Alvira, S., Cuellar, J., Valpuesta, J. M., Madl, T., Sattler, M., and Buchner, J. "Modulation of the Hsp90 chaperone cycle by a stringent client protein". *Molecular Cell* 53 (2014), pp. 941–953. DOI: `10.1016/j.molcel.2014.02.003`.

[77] Louvion, J.-F., Warth, R., and Picard, D. "Two eukaryote-specific regions of Hsp82 are dispensable for its viability and signal transduction functions in yeast". *Proceedings of the National Academy of Sciences of the United States of America* 93 (1996), pp. 13937–13942. URL: `http://www.pnas.org/content/93/24/13937`.

[78] Martinez-Yamout, M. A., Venkitakrishnan, R. P., Preece, N. E., Kroon, G., Wright, P. E., and Dyson, H. J. "Localization of sites of interaction between p23 and Hsp90 in solution". *Journal of Biological Chemistry* 281 (2006), pp. 14457–14464. DOI: `10.1074/jbc.M601759200`.

[79] Mayer, M. P., Prodromou, C., and Frydman, J. "The Hsp90 mosaic: a picture emerges". *Nature Structural & Molecular Biology* 16 (2009), pp. 2–6. DOI: `10.1038/nsmb0109-2`.

[80] McKinney, S. A., Joo, C., and Ha, T. "Analysis of single-molecule FRET trajectories using hidden Markov modeling". *Biophysical Journal* 91 (2006), pp. 1941–1951. DOI: `10.1529/biophysj.106.082487`.

[81] McLaughlin, S. H., Smith, H. W., and Jackson, S. E. "Stimulation of the weak ATPase activity of human Hsp90 by a client protein". *Journal of Molecular Biology* 315 (2002), pp. 787–798. DOI: `10.1006/jmbi.2001.5245`.

[82] McLaughlin, S. H., Ventouras, L.-A., Lobbezoo, B., and Jackson, S. E. "Independent ATPase activity of Hsp90 subunits creates a flexible assembly platform". *Journal of Molecular Biology* 344 (2004), pp. 813–826. DOI: `10.1016/j.jmb.2004.09.055`.

[83] Meeker, W. Q. and Escobar, L. A. "Teaching about Approximate Confidence Regions Based on Maximum Likelihood Estimation". *The American Statistician* 49 (1995), p. 48. DOI: `10.2307/2684811`.

[84] Meyer, P., Prodromou, C., Liao, C., Hu, B., Roe, S. M., Vaughan, C. K., Vlasic, I., Panaretou, B., Piper, P. W., and Pearl, L. H. "Structural basis for recruitment of the ATPase activator Aha1 to the Hsp90 chaperone machinery". *The EMBO Journal* 23 (2004), pp. 1402–1410. DOI: `10.1038/sj.emboj.7600141`.

[85] Mickler, M., Hessling, M., Ratzke, C., Buchner, J., and Hugel, T. "The large conformational changes of Hsp90 are only weakly coupled to ATP hydrolysis". *Nature Structural & Molecular Biology* 16 (2009), pp. 281–286. DOI: `10.1038/nsmb.1557`.

[86] Mishra, P. and Bolon, D. N. A. "Designed Hsp90 heterodimers reveal an asymmetric ATPase-driven mechanism in vivo". *Molecular Cell* 53 (2014), pp. 344–350. DOI: `10.1016/j.molcel.2013.12.024`.

[87] Mittag, T., Kay, L. E., and Forman-Kay, J. D. "Protein dynamics and conformational disorder in molecular recognition". *Journal of Molecular Recognition* 23 (2010), pp. 105–116. DOI: `10.1002/jmr.961`.

[88] Morra, G., Verkhivker, G., Colombo, G., and Jacobson, M. P. "Modeling Signal Propagation Mechanisms and Ligand-Based Conformational Dynamics of the Hsp90 Molecular Chaperone Full-Length Dimer". *PLoS Computational Biology* 5 (2009), e1000323. DOI: `10.1371/journal.pcbi.1000323`.

[89] Motojima-Miyazaki, Y., Yoshida, M., and Motojima, F. "Ribosomal protein L2 associates with E. coli HtpG and activates its ATPase activity". *Biochemical and Biophysical Research Communications* 400 (2010), pp. 241–245. DOI: `10.1016/j.bbrc.2010.08.047`.

[90] Muschielok, A., Andrecka, J., Jawhari, A., Brückner, F., Cramer, P., and Michaelis, J. "A nano-positioning system for macromolecular structural analysis". *Nature Methods* 5 (2008), pp. 965–971. DOI: `10.1038/nmeth.1259`.

[91] Myung, I. J. "Tutorial on maximum likelihood estimation". *Journal of Mathematical Psychology* 47 (2003), pp. 90–100. DOI: `10.1016/S0022-2496(02)00028-7`.

[92] Nathan, D. F., Vos, M. H., and Lindquist, S. L. "In vivo functions of the saccharomyces cerevisiae hsp90 chaperone". *Proceedings of the National Academy of Sciences of the United States of America* 94 (1997), pp. 12949–12956. URL: `http://www.pnas.org/content/94/24/12949`.

[93] Obermann, W. M., Sondermann, H., Russo, A. A., Pavletich, N. P., and Hartl, F. U. "In Vivo Function of Hsp90 Is Dependent on ATP Binding and ATP Hydrolysis". *The Journal of Cell Biology* 143 (1998), pp. 901–910. DOI: `10.1083/jcb.143.4.901`.

[94] Owicki, J. C. “Fluorescence polarization and anisotropy in high throughput screening: perspectives and primer”. *Journal of Biomolecular Screening* 5 (2000), pp. 297–306. DOI: `10.1177/108705710000500501`.

[95] Panaretou, B., Siligardi, G., Meyer, P., Maloney, A., Sullivan, J. K., Singh, S., Millson, S. H., Clarke, P. A., Naaby-Hansen, S., Stein, R., Cramer, R., Mollapour, M., Workman, P., et al. “Activation of the ATPase Activity of Hsp90 by the Stress-Regulated Cochaperone Aha1”. *Molecular Cell* 10 (2002), pp. 1307–1318. DOI: `10.1016/S1097-2765(02)00785-2`.

[96] Panavas, T., Sanders, C., and Butt, T. R. “SUMO Fusion Technology for Enhanced Protein Production in Prokaryotic and Eukaryotic Expression Systems”. *SUMO Protocols*. Ed. by Ulrich, H. D. Totowa, NJ: Humana Press, 2009, pp. 303–317. DOI: `10.1007/978-1-59745-566-4_20`.

[97] Pearl, L. H. and Prodromou, C. “Structure and mechanism of the Hsp90 molecular chaperone machinery”. *Annual Review of Biochemistry* 75 (2006), pp. 271–294. DOI: `10.1146/annurev.biochem.75.103004.142738`.

[98] Pearl, L. H. “Review. The HSP90 molecular chaperone—an enigmatic ATPase”. *Biopolymers* 105 (2016), pp. 594–607. DOI: `10.1002/bip.22835`.

[99] Perrin, F. “Polarisation de la lumière de fluorescence. Vie moyenne des molécules dans l’etat excité”. *Journal de Physique et le Radium* 7 (1926), pp. 390–401. DOI: `10.1051/jphysrad:01926007012039000`.

[100] Picard, D. “Heat-shock protein 90, a chaperone for folding and regulation”. *Cellular and Molecular Life Sciences* 59 (2002), pp. 1640–1648. DOI: `10.1007/PL00012491`.

[101] Plass, T., Milles, S., Koehler, C., Schultz, C., and Lemke, E. A. “Genetically encoded copper-free click chemistry”. *Angewandte Chemie (International ed. in English)* 50 (2011), pp. 3878–3881. DOI: `10.1002/anie.201008178`.

[102] Prodromou, C., Panaretou, B., Chohan, S., Siligardi, G., O’Brien, R., Ladbury, J. E., Roe, S. M., Piper, P. W., and Pearl, L. H. “The ATPase cycle of Hsp90 drives a molecular ’clamp’ via transient dimerization of the N-terminal domains”. *The EMBO Journal* 19 (2000), pp. 4383–4392. DOI: `10.1093/emboj/19.16.4383`.

[103] Prodromou, C., Nuttall, J. M., Millson, S. H., Roe, S. M., Sim, T.-S., Tan, D., Workman, P., Pearl, L. H., and Piper, P. W. “Structural basis of the radicicol resistance displayed by a fungal hsp90”. *ACS Chemical Biology* 4 (2009), pp. 289–297. DOI: `10.1021/cb9000316`.

[104] Prodromou, C. “Mechanisms of Hsp90 regulation”. *The Biochemical Journal* 473 (2016), pp. 2439–2452. DOI: `10.1042/BCJ20160005`.

[105] Qin, F., Auerbach, A., and Sachs, F. “Estimating single-channel kinetic parameters from idealized patch-clamp data containing missed events”. *Biophysical Journal* 70 (1996), pp. 264–280. DOI: `10.1016/S0006-3495(96)79568-1`.

[106] Qin, F. and Li, L. "Model-based fitting of single-channel dwell-time distributions". *Biophysical Journal* 87 (2004), pp. 1657–1671. DOI: `10.1529/biophysj.103.037531`.

[107] Rabiner, L. R. "A tutorial on hidden Markov models and selected applications in speech recognition". *Proceedings of the IEEE* 77 (1989), pp. 257–286. DOI: `10.1109/5.18626`.

[108] Ratzke, C., Nguyen, M. T. N., Mayer, M. P., and Hugel, T. "From a ratchet mechanism to random fluctuations evolution of Hsp90's mechanochemical cycle". *Journal of Molecular Biology* 423 (2012), pp. 462–471. DOI: `10.1016/j.jmb.2012.07.026`.

[109] Ratzke, C., Berkemeier, F., and Hugel, T. "Heat shock protein 90's mechanochemical cycle is dominated by thermal fluctuations". *Proceedings of the National Academy of Sciences of the United States of America* 109 (2012), pp. 161–166. DOI: `10.1073/pnas.1107930108`.

[110] Ratzke, C., Hellenkamp, B., and Hugel, T. "Four-colour FRET reveals directionality in the Hsp90 multicomponent machinery". *Nature Communications* 5 (2014), p. 4192. DOI: `10.1038/ncomms5192`.

[111] Rehn, A. B. and Buchner, J. "p23 and Aha1". *Sub-Cellular Biochemistry* 78 (2015), pp. 113–131. DOI: `10.1007/978-3-319-11731-7_6`.

[112] Retzlaff, M., Hagn, F., Mitschke, L., Hessling, M., Gugel, F., Kessler, H., Richter, K., and Buchner, J. "Asymmetric activation of the hsp90 dimer by its cochaperone aha1". *Molecular Cell* 37 (2010), pp. 344–354. DOI: `10.1016/j.molcel.2010.01.006`.

[113] Richter, K., Muschler, P., Hainzl, O., and Buchner, J. "Coordinated ATP hydrolysis by the Hsp90 dimer". *Journal of Biological Chemistry* 276 (2001), pp. 33689–33696. DOI: `10.1074/jbc.M103832200`.

[114] Richter, K., Walter, S., and Buchner, J. "The Co-chaperone Sba1 Connects the ATPase Reaction of Hsp90 to the Progression of the Chaperone Cycle". *Journal of Molecular Biology* 342 (2004), pp. 1403–1413. DOI: `10.1016/j.jmb.2004.07.064`.

[115] Schmid, S., Götz, M., and Hugel, T. "Single-Molecule Analysis beyond Dwell Times: Demonstration and Assessment in and out of Equilibrium". *Biophysical Journal* 111 (2016), pp. 1375–1384. DOI: `10.1016/j.bpj.2016.08.023`.

[116] Schmid, S. "Single Protein Dynamics at Steady State Quantified from FRET Time Traces. Biochemical & Physical Manipulation of Hsp90". Fakultät für Physik. Dissertation. München: Technische Universität München, 2017.

[117] Schopf, F. H., Biebl, M. M., and Buchner, J. "The HSP90 chaperone machinery". *Nature Reviews. Molecular Cell Biology* (2017). DOI: `10.1038/nrm.2017.20`.

[118] Schuler, B. and Hofmann, H. “Single-molecule spectroscopy of protein folding dynamics—expanding scope and timescales. Folding and binding / Protein-nucleic acid interactions”. *Current Opinion in Structural Biology* 23 (2013), pp. 36–47. DOI: `10.1016/j.sbi.2012.10.008`.

[119] Schulte, T. W., Akinaga, S., Soga, S., Sullivan, W. P., Stensgard, B., Toft, D. O., and Neckers, L. M. “Antibiotic radicicol binds to the N-terminal domain of Hsp90 and shares important biologic activities with geldanamycin”. *Cell Stress & Chaperones* 3 (1998), pp. 100–108. URL: `https://www.ncbi.nlm.nih.gov/pmc/articles/PMC312953`.

[120] Schulze, A., Beliu, G., Helmerich, D. A., Schubert, J., Pearl, L. H., Prodromou, C., and Neuweiler, H. “Cooperation of local motions in the Hsp90 molecular chaperone ATPase mechanism”. *Nature Chemical Biology* 12 (2016), pp. 628–635. DOI: `10.1038/nchembio.2111`.

[121] Schütz, G. J., Trabesinger, W., and Schmidt, T. “Direct Observation of Ligand Colocalization on Individual Receptor Molecules”. *Biophysical Journal* 74 (1998), pp. 2223–2226. DOI: `10.1016/S0006-3495(98)77931-7`.

[122] Schwarz, G. “Estimating the Dimension of a Model”. *The Annals of Statistics* 6 (1978), pp. 461–464. URL: `http://www.jstor.org/stable/2958889`.

[123] Sharma, S. V., Agatsuma, T., and Nakano, H. “Targeting of the protein chaperone, HSP90, by the transformation suppressing agent, radicicol”. *Oncogene* 16 (1998), pp. 2639–2645. DOI: `10.1038/sj.onc.1201790`.

[124] Shortle, D. and Abeygunawardana, C. “NMR analysis of the residual structure in the denatured state of an unusual mutant of staphylococcal nuclease”. *Structure* 1 (1993), pp. 121–134. DOI: `10.1016/0969-2126(93)90027-E`.

[125] Siligardi, G., Hu, B., Panaretou, B., Piper, P. W., Pearl, L. H., and Prodromou, C. “Co-chaperone regulation of conformational switching in the Hsp90 ATPase cycle”. *Journal of Biological Chemistry* 279 (2004), pp. 51989–51998. DOI: `10.1074/jbc.M410562200`.

[126] Southworth, D. R. and Agard, D. A. “Species-dependent ensembles of conserved conformational states define the Hsp90 chaperone ATPase cycle”. *Molecular Cell* 32 (2008), pp. 631–640. DOI: `10.1016/j.molcel.2008.10.024`.

[127] Stefan, M. I. and Le Novère, N. “Cooperative binding”. *PLoS Computational Biology* 9 (2013), e1003106. DOI: `10.1371/journal.pcbi.1003106`.

[128] Street, T. O., Lavery, L. A., and Agard, D. A. “Substrate binding drives large-scale conformational changes in the Hsp90 molecular chaperone”. *Molecular Cell* 42 (2011), pp. 96–105. DOI: `10.1016/j.molcel.2011.01.029`.

[129] Street, T. O., Zeng, X., Pellarin, R., Bonomi, M., Sali, A., Kelly, M. J. S., Chu, F., and Agard, D. A. “Elucidating the mechanism of substrate recognition by the bacterial Hsp90 molecular chaperone”. *Journal of Molecular Biology* 426 (2014), pp. 2393–2404. DOI: `10.1016/j.jmb.2014.04.001`.

[130] Stryer, L. and Haugland, R. P. "Energy transfer: a spectroscopic ruler". *Proceedings of the National Academy of Sciences of the United States of America* 58 (1967), pp. 719–726. URL: `http://www.pnas.org/content/58/2/719.citation`.

[131] Sullivan, W. P., Owen, B. A. L., and Toft, D. O. "The influence of ATP and p23 on the conformation of hsp90". *Journal of Biological Chemistry* 277 (2002), pp. 45942–45948. DOI: `10.1074/jbc.M207754200`.

[132] Sunney Xie, X. "Single-molecule approach to dispersed kinetics and dynamic disorder. Probing conformational fluctuation and enzymatic dynamics". *The Journal of Chemical Physics* 117 (2002), pp. 11024–11032. DOI: `10.1063/1.1521159`.

[133] Swoboda, M., Henig, J., Cheng, H.-M., Brugger, D., Haltrich, D., Plumeré, N., and Schlierf, M. "Enzymatic oxygen scavenging for photostability without pH drop in single-molecule experiments". *ACS Nano* 6 (2012), pp. 6364–6369. DOI: `10.1021/nn301895c`.

[134] Taipale, M., Jarosz, D. F., and Lindquist, S. L. "HSP90 at the hub of protein homeostasis: emerging mechanistic insights". *Nature Reviews. Molecular Cell Biology* 11 (2010), pp. 515–528. DOI: `10.1038/nrm2918`.

[135] Tamura, J. K. and Gellert, M. "Characterization of the ATP binding site on Escherichia coli DNA gyrase. Affinity labeling of Lys-103 and Lys-110 of the B subunit by pyridoxal 5'-diphospho-5'-adenosine". *Journal of Biological Chemistry* 265 (1990), pp. 21342–21349. URL: `http://www.jbc.org/content/265/34/21342.full.pdf`.

[136] Verba, K. A., Wang, R. Y.-R., Arakawa, A., Liu, Y., Shirouzu, M., Yokoyama, S., and Agard, D. A. "Atomic structure of Hsp90-Cdc37-Cdk4 reveals that Hsp90 traps and stabilizes an unfolded kinase". *Science* 352 (2016), pp. 1542–1547. DOI: `10.1126/science.aaf5023`.

[137] Visser, I., Raijmakers, M. E. J., and Molenaar, P. C. M. "Confidence intervals for hidden Markov model parameters". *British Journal of Mathematical and Statistical Psychology* 53 (2000), pp. 317–327. DOI: `10.1348/000711000159240`.

[138] Wang, Y., Alexandrescu, A. T., and Shortle, D. "Initial studies of the equilibrium folding pathway of staphylococcal nuclease". *Philosophical Transactions of the Royal Society of London. Series B, Biological Sciences* 348 (1995), pp. 27–34. DOI: `10.1098/rstb.1995.0042`.

[139] Wayne, N. and Bolon, D. N. "Dimerization of Hsp90 is required for in vivo function. Design and analysis of monomers and dimers". *Journal of Biological Chemistry* 282 (2007), pp. 35386–35395. DOI: `10.1074/jbc.M703844200`.

[140] Weaver, A. J., Sullivan, W. P., Felts, S. J., Owen, B. A. L., and Toft, D. O. "Crystal structure and activity of human p23, a heat shock protein 90 co-chaperone". *Journal of Biological Chemistry* 275 (2000), pp. 23045–23052. DOI: `10.1074/jbc.M003410200`.

[141] Weikl, T., Abelmann, K., and Buchner, J. “An unstructured C-terminal region of the Hsp90 co-chaperone p23 is important for its chaperone function”. *Journal of Molecular Biology* 293 (1999), pp. 685–691. DOI: `10.1006/jmbi.1999.3172`.

[142] Whitesell, L., Mimnaugh, E. G., Costa, B. de, Myers, C. E., and Neckers, L. M. “Inhibition of heat shock protein HSP90-pp60v-src heteroprotein complex formation by benzoquinone ansamycins. Essential role for stress proteins in oncogenic transformation”. *Proceedings of the National Academy of Sciences of the United States of America* 91 (1994), pp. 8324–8328. URL: `http://www.pnas.org/content/91/18/8324`.

[143] Whitesell, L. and Lindquist, S. L. “HSP90 and the chaperoning of cancer”. *Nature Reviews. Cancer* 5 (2005), pp. 761–772. DOI: `10.1038/nrc1716`.

[144] Wortmann, P., Götz, M., and Hugel, T. “Cooperative Nucleotide Binding in Hsp90 and Its Regulation by Aha1”. *Biophysical Journal* 113 (2017), pp. 1711–1718. DOI: `10.1016/j.bpj.2017.08.032`.

[145] Ye, K. and Wang, J. “Self-association reaction of denatured staphylococcal nuclease fragments characterized by heteronuclear NMR”. *Journal of Molecular Biology* 307 (2001), pp. 309–322. DOI: `10.1006/jmbi.2000.4449`.

[146] Young, J. C., Moarefi, I., and Hartl, F. U. “Hsp90. a specialized but essential protein-folding tool”. *The Journal of Cell Biology* 154 (2001), pp. 267–274. DOI: `10.1083/jcb.200104079`.

[147] Zierer, B. K., Rübbelke, M., Tippel, F., Madl, T., Schopf, F. H., Rutz, D. A., Richter, K., Sattler, M., and Buchner, J. “Importance of cycle timing for the function of the molecular chaperone Hsp90”. *Nature Structural & Molecular Biology* 23 (2016), pp. 1020–1028. DOI: `10.1038/nsmb.3305`.